論文 / 著書情報
Article / Book Information

題目(和文)	
Title(English)	Materials Design and Fabrication of Metal-Embedded Core-Shell and Yolk-Shell Nanocrystals and Characterization of the Charge Transfer Mechanism and Photocatalytic Activity
著者(和文)	呉振揚
Author(English)	Jhen-Yang Wu
出典(和文)	学位:博士(工学), 学位授与機関:東京工業大学, 報告番号:甲第12725号, 授与年月日:2024年3月26日, 学位の種別:課程博士, 審査員:CHANG TSO-FU,曽根 正人,細田 秀樹,小林 郁夫,林 智広,HSU YUNG JUNG
Citation(English)	Degree:Doctor (Engineering), Conferring organization: Tokyo Institute of Technology, Report number:甲第12725号, Conferred date:2024/3/26, Degree Type:Course doctor, Examiner:,,,,,
学位種別(和文)	博士論文
Type(English)	Doctoral Thesis

Materials Design and Fabrication of Metal-Embedded Core-Shell and Yolk-Shell Nanocrystals and Characterization of the Charge Transfer Mechanism and Photocatalytic Activity

Department of Materials Science and Engineering

Tokyo Institute of Technology

Jhen–Yang Wu

March, 2024

Table of content

CHAPTER 1

General Introduction

1.1 Background

1.1.1 Core-shell and yolk-shell nanocrystals as photocatalysts

In the preceding decade, there has been a pressing call for alternative energy solutions, steering both academic and industrial sectors to channel their efforts towards green energy technologies. The sun, integral to human existence, serves as a nearly endless source of clean, renewable energy. The challenge lies in harnessing this natural bounty efficiently. Photocatalysts act as conduits, transforming solar energy into chemical energy, positioning photocatalysis as a competitive contender among varied energy conversion methodologies. Through photocatalytic water splitting[1] and CO_2 reduction,[2] substances like H_2, O_2, and hydrocarbons can be generated, presenting viable alternative fuels to supplant fossil fuels. Regardless of how these fuels are used, they leave behind clean, eco-friendly by-products, aligning with the key idea of sustainable development. Besides fuel production, photocatalysis also plays a role in treating wastewater and remediating environmental issues, offering a practical solution to the growing global environmental changes by breaking down harmful organic (e.g., antibiotics,[3] dyes,[4] bacteria[5]) and inorganic substances (e.g., heavy metal ions[6]). Photocatalysis can also

reduce the high costs and complex procedures involved in producing value-added chemicals, with ongoing efforts directed towards creating high value-added organic compounds through photocatalytic reactions. Furthermore, photocatalysis can alleviate the high expenses and complex procedures involved in the production of value-added chemicals.[7] Continual endeavors have been channeled towards generating high value-added organic compounds through photocatalytic reactions.

The mechanism of photocatalysis can be delineated into three cardinal steps. Initially, semiconductor photocatalysts are subjected to light irradiation of sufficient energy; this constitutes the first step. Subsequently, the second step unfolds with the generation of electron-hole pairs, followed by the ensuing transfer of charge carriers. The third and final step encompasses the mediation of surface redox reactions by photoexcited electrons and holes, culminating the photocatalytic process. From a thermodynamic standpoint, the photoexcited electrons must possess adequate reducing ability to facilitate the desired reduction reactions. In essence, the conduction band (CB) level of the chosen photocatalyst should be situated at a potential that is more cathodic compared to the potential necessary for the reduction reactions. Similarly, the valence band (VB) level of the semiconductor should be positioned at a sufficiently anodic potential to provide photoexcited holes with the necessary oxidizing capacity to carry out oxidation reactions. During the photocatalytic process, several challenges arise that can dampen photocatalytic activity. These hurdles encompass inadequate light absorption, brisk electron-hole recombination, and lethargic charge transfer kinetics. Due to these limitations, only a restricted number of charge carriers can engage in surface redox reactions. The situation could be improved by engineering composite photocatalysts characterized by well-defined structural and compositional heterogeneity, wherein the

features of individual components are synergistically harnessed. Notably, the integration of multiple components to form a heterojunction can alter the electronic band structure, amending charge transfer behavior to enhance carrier utilization efficiency. To date, a range of composite nanocrystals have been suggested as the paradigm for developing superior photocatalytic systems. Representative examples include doped/alloyed nanocrystals, particle-decorated nanocrystals, heterodimers, core-shell nanocrystals, and yolk-shell nanocrystals. Among these, core-shell and yolk-shell nanocrystals represent a burgeoning platform in photocatalyst technology. In core-shell nanocrystals, a core is encapsulated by an outer shell. These structures, with their unique morphologies and physicochemical properties, present enticing advantages such as notable chemical and thermal stability, enhanced permeability and solubility, and augmented functionality and activity.[8] Among the various attributes of core-shell nanocrystals, the heightened stability and ease of charge transfer between the two phases are paramount. The superior stability is achieved by enveloping one material with another, while the facile charge transfer is facilitated through their intimate contact. This latter aspect can be pivotal in engineering the band gap and harnessing visible light, paving the way for utilizing cost-effective and abundant solar light to initiate photoactivity. On the other hand, yolk-shell nanocrystals stand for a newly emerging photocatalyst platform, which are composed of a movable core surrounded by a permeable shell with void space. Theoretically speaking, yolk-shell structures can also be considered a type of core-shell nanocrystals. Such a peculiar architecture possesses several noteworthy advantages, including confined space which can facilitate the diffusion of reacting species, and large surface area which can provide abundant active sites. Besides, the incident light may undergo multiple reflections inside the void space and thus conduce to photon harvesting.[9]

In recent years, substantial efforts have been channeled towards devising viable synthetic pathways for core-shell and yolk-shell nanostructures and demonstrating their potency in photocatalytic applications. Through innovative approaches, researchers have not only expanded the synthesis toolkit for these nanostructures but also explored their potential in harnessing solar energy, thereby contributing to the advancement of green technology solutions. As depicted in Figure 1 and 2, this thesis renders a thorough retrospection on the formulation and photocatalytic utilities of core-shell and yolk-shell nanocrystals. A heightened emphasis is cast upon understanding the interfacial charge dynamics and the potential for achieving spatial segregation of charge carriers within this singular nanoarchitecture, given that charge transfer is the linchpin determining the overarching photocatalytic efficiency. The discourse culminates with a summarization and an outlook towards the future, aiming to foster the progression of employing core-shell and yolk-shell nanocrystals in intricate photocatalytic systems.

1.1.2 Synthesis approach for core-shell

In the realm of synthesis, methodologies employed for fabricating nanomaterials are generally adaptable for preparing the core and/or shell components of core-shell nanocrystals. While top-down strategies, where external controls like microfabrication techniques and mechanical stress are leveraged to deconstruct bulk materials into desired nanomaterials of varying shapes and sizes, are feasible, bottom-up techniques are predominantly favored. In this latter approach, nanomaterials are synthesized from molecular or atomic building blocks, capitalizing on the intrinsic chemical properties of the individual constituents and their collective interactions to govern the shape and size of the resultant nanomaterials. Utilizing bottom-up synthetic methods, the core and shell

can be crafted either in a stepwise manner or via a one-pot approach. Both strategies have found application in the synthesis of core-shell nanocrystals. Nonetheless, the evolution of new and modified procedures continues, with advancements being regularly documented in scholarly literature.

Drawing inspiration from the categorization framework conceived by Paria, this section delves into the synthesis of varied core-shell nanocrystals pivoting on the material types rather than the procedural techniques employed for their creation. Herein, core-shell nanocrystals are bifurcated into two principal classes: organics and inorganics. The organic domain encompasses carbon-centric materials, predominantly polymers, while the inorganic realm encapsulates metal, metalloid, and metal salt nanoparticles. The synthesis methodologies deployed for each of these categories are explored in this review, enriched with contemporary exemplars. As a segue to the conclusion, a modernized classification schema predicated on the shell properties of the core-shell nanomaterials is integrated, reflecting the escalating significance of nano catalysis in this field.

Organics: Despite being relatively nascent compared to traditional core-shell nanocrystals, the allure of utilizing carbon-based compounds, especially in terms of material stability and biocompatibility, has garnered considerable attention. The synthesis of such materials predominantly hinges on polymerization techniques to fashion the organic core, shell, or both. At the heart of polymerization lies the creation of 3D network-like structures through the amalgamation of numerous units of suitable monomeric substrates possessing pivotal functionalities. While the norm is often the initial synthesis of organic cores, organic shells too can be fabricated in situ. Furthermore, the employment of surface modifiers like surfactants and polyelectrolytes can be leveraged to bolster coating efficiency and stability, thus enhancing the versatility and applicability of these

organic core-shell nanocrystals.

Inorganics: The umbrella of "inorganic" materials unfolds into two prominent sub-categories: (a) silica-based core-shell nanocrystals, and (b) metal-based core-shell nanocrystals.

(a) **Silica-based core-shell nanocrystals**: Predominantly fabricated through sol-gel chemistry, historically known as the Stöber method, these core-shell nanocrystals see the light of day via the hydrolysis and subsequent condensation of silicon alkoxides or silicon halides in a milieu of alcohol, water, or a blend of both, under the catalytic eye of a base like ammonia. This method, hailed for its simplicity, reproducibility, and versatility, has been an architect of varied silica-based core-shell nanocrystals. Though initially tethered to solid, non-porous SiO_2, the trajectory has veered towards porous materials, courtesy of template-based techniques or post-synthetic modifications. This shift not only amplifies the surface area but also elevates core and shell accessibility. The pore narrative further evolves with functional group modifications, paving the way for multi-functional materials apt for diverse catalytic rendezvous.

(b) **Metal-based core-shell nanocrystals**: This expansive class necessitates further dissection into: (i) metallic nanoparticles, (ii) metal oxides, and (iii) metal salts. The narrative of metallic nano particles is often penned through the reduction of metal salts, with characters like $NaBH_4$ and hydrazine playing the reducing agent role, or transmetalation exploiting the intrinsic redox traits of metal precursors. The plot, influenced by reaction medium, temperature, and reducing agent type, shapes the particle growth, size, and thus the spectrum of chemical, physical, optical, and biological properties. The metal oxide subplot, with titania-based materials as protagonists, often shares the sol-gel method stage with silica. These materials, showcasing a spectrum of

properties, find roles in photo-, bio-, and energy- realms. Thermal treatment acts as a subplot twist, tuning structures, physical robustness, or porosity. The faster kinetics of titania-based material formation, owing to the relatively higher reactivity of its precursors compared to silica, adds a layer of complexity. The availability of a myriad of structurally and electronically different precursors, coupled with intriguing phase-behavior, permits modulation of the final structure and reactivity of the precursors, crafting a variety of nanostructures, each with its own tale of potential and application. Within the context of core-shell nanocrystals, recent literature showcases instances where TiO_2, in varied forms, has been employed as a component, predominantly as the shell. Besides the celebrated sol-gel method, co-precipitation and thermal decomposition methods have also been championed to synthesize other metal oxides, contingent on the chemical temperament of the metal precursors. The co-precipitation technique primarily finds favor with metal oxides/hydroxides amenable to precipitation under basic conditions, while thermal decomposition navigates the high-temperature corridor, orchestrating the thermolysis of organometallic precursors in the oxygen or air theatre to yield the final product. Noteworthy instances include magnetic core-shell nanocatalysts birthed from a blend of hydrolysis and thermal treatment of Fe-precursors.

Moreover, Chemical Vapor Deposition (CVD) and Pulsed Layer Deposition (PLD) have also been enlisted for crafting metal oxides from gaseous precursors, often engaging in the in-situ synthesis of metal oxides. The narrative of metal-salt based core-shell nanocrystals unfolds with metal chalcogenides/halides playing pivotal roles in semiconductor-based devices and bioimaging arenas. Commonly, these are synthesized by precipitating metal salts from a choreography of metal precursors and chosen counter ions in the presence of stabilizer/capping agents, with the reactivity of metal salts towards

external parameters like oxygen and temperature steering further modifications.

A relatively new actor on the stage, the Successive Ionic Layer Adsorption and Reaction (SILAR) method, has emerged to synthesize metal-salt based core-shell nanocrystals, primarily eyeing their semiconductor and photovoltaic properties. SILAR orchestrates uniform and isotropic growth of shell materials over core particles, minimizing the emergence of unwanted nanocrystals of just the shell material. The annealing act between successive depositions, pivotal for crafting multi-shell nanoparticles, aids in eradicating any bias emanating from either the core or shell materials. Veering beyond such classifications and methods, alternate energy inputs like ultrasound-, and microwave-irradiation, and electrodeposition have also been explored for core-shell nanocrystals synthesis. In sonochemical synthesis, sound frequency modulation spawns local microreactors/cavities, promoting better mixing and generating short-lived shock waves that induce localized heating for smaller particle production. Electrodeposition, on the other hand, follows a narrative of substrate/core material deposition on an electrode or supported matrix from a bulk electrolyte solution, courtesy of an electric field, with the shell decoration unfolding through different electrolytes or synthetic strategies. Recent strides in microwave technology have also ushered in expedited synthesis of core-shell nanocrystals components with a decent reign over structural properties.

1.1.3 Synthesis approach for yolk-shell

Based on the mechanism of void space formation, the synthetic approach to yolk-shell nanocrystals can be classified into five distinct categories. These include the (a) Kirkendall effect, (b) Galvanic replacement, (c) Ostwald ripening, (d) chemical etching,

and (d) physical volatilization or oxidative decomposition through thermal treatment. Both the Kirkendall effect and galvanic replacement are intertwined with ion exchange; however, they diverge at their roots where the former originates from different solubility products and the latter from distinct redox potentials. These methods employ the inherent chemical properties of materials to engineer the hollow or void spaces within the nanocrystals. On the other hand, Ostwald ripening, a crystal growth narrative, orchestrates the dissolution of smaller particles, bequeathing their mass onto larger counterparts. This process can be harnessed to spawn void spaces as the dissolved particles contract. Transitioning to chemical etching, this method unfolds a drama of void space creation at the altar of sacrificial templates through the act of selective etching, akin to carving out spaces by selectively removing material using chemical agents. Lastly, the tale of hollow structure genesis via physical volatilization or oxidative decomposition navigates the thermal treatment pathway. Herein, thermal energy acts as a catalyst to either volatilize or oxidatively decompose material, thus scripting the emergence of hollow or void structures. The subsequent section endeavors to delve deeper into the intricacies of these synthetic systems, shedding light on the underlying mechanisms and the plethora of possibilities they unfurl in the realm of yolk-shell nanocrystal synthesis. Through a closer examination of these methods, a more profound understanding of the diverse pathways to achieving the desired yolk-shell nanocrystals is attained, each with its own set of advantages, challenges, and potential applications.

(a) **Kirkendall effect:** The Kirkendall effect, anchored in diffusion dynamics, has been extensively harnessed to craft hollow structures, serving as a bedrock for the synthesis of yolk-shell nanocrystals. This phenomenon unfolds when a diffusion couple encounters different diffusion rates, subsequently birthing voids as two ions engage. As

the narrative of this principle unfolds in contemporary research, a plethora of works have emerged, employing the Kirkendall effect to fabricate yolk-shell nanocrystals of diverse compositions. This effect, therefore, stands as a potentially universal strategy in the yolk-shell nanocrystal synthesis arena. By meticulously accounting for the difference in solubility products, one can navigate towards obtaining yolk-shell nanocrystals with the desired compositions. This method not only unveils a pathway for creating such intricate structures but also opens a vista of possibilities in tailoring the material properties, thereby extending the potential applications of yolk-shell nanocrystals in various fields.

(b) **Galvanic replacement:** By judicious selection of two elements with appropriate oxidation and reduction potentials, a spontaneous replacement reaction can be triggered. This principle has been commonly employed to fabricate yolk-shell nanocrystals encompassing a broad spectrum of compositions. Mirroring the Kirkendall effect, galvanic replacement emerges as a universal approach towards the synthesis of yolk-shell nanocrystals. By orchestrating a pair of suitable redox potentials, one can readily craft yolk-shell nanocrystals with a diverse array of material combinations. This method not only showcases the versatility in the composition of the resultant yolk-shell nanocrystals but also underscores the feasibility of tailoring these nanocrystals to suit specific application needs, thereby broadening the horizon of their potential utilization in various technological domains.

(c) **Ostwald ripening:** Ostwald ripening, a process underlined by the principle of energy minimization, orchestrates the growth of yolk-shell nanocrystals, whether of singular composition (homogeneous) or multiple compositions (heterogeneous). In the saga of homogeneous yolk-shell structure formation, a core particle undergoes dissolution, with a subsequent re-deposition of a shell layer embracing the gradually dissolving core.

Contrarily, the narrative of heterogeneous yolk-shell structures unfolds as either the core particle or the shell layer itself dissolves and re-crystalizes, heralding the growth of these structures. The realm of heterogeneous yolk-shell nanocrystals has garnered heightened attention owing to the enchanting synergistic properties they exhibit, holding a promise of broad-spectrum applications. The driving force behind Ostwald ripening is widely recognized as the quest for surface energy minimization. However, the precise systematic factors propelling the ripening process still elude control, presenting a domain ripe for further exploration and understanding. This lack of control over inducing factors continues to pose a challenge, yet also an opportunity for delving deeper into the mechanistic intricacies of Ostwald ripening, thus paving the way for more controlled synthesis of yolk-shell nanocrystals with tailored properties.

(d) **Chemical etching:** Among the diverse pathways for crafting yolk-shell nanocrystals, the template-assisted method emerges as a notably straightforward approach. This method hinges on the deposition of an additional layer of etchable materials, predominantly SiO_2, nestled between the core and shell components. Following this deposition, selective etching is employed to eliminate this intermediary layer, thus giving birth to an empty space between the core and shell. This principle of chemical etching extends a versatile scaffold for the synthesis of a myriad of yolk-shell nanocrystals, embodying the essence of the template-assisted approach. The versatility of this method lies in its adaptability to various material systems, paving the way for a plethora of yolk-shell nanocrystal compositions. However, a lingering concern gravitates around the durability of the components during the template removal phase, as this process often calls for the employment of strong acids or bases. The corrosive nature of these chemicals poses a challenge to the integrity and stability of the core-shell structure

amidst the template removal endeavor. This scenario underscores a crucial area for further exploration and innovation to ensure the robustness of the yolk-shell nanocrystals, while preserving the simplicity and adaptability that the template-assisted chemical etching method promises.

(e) **Thermal treatment:** An alternative versatile strategy to fabricate yolk-shell nanocrystals hinges on the thermal treatment method, where volatile components are decomposed and expelled under high temperatures. This method unfurls a spectrum of possibilities for creating yolk-shell nanocrystals with a diverse range of compositions. It finds a particular resonance in the synthesis of metal oxides-based yolk-shell nanocrystals, where high-temperature operations are requisite. However, akin to the concerns associated with the chemical etching approach, the thermal treatment method beckons a cautious scrutiny of the potential deterioration of materials properties under the austere high-temperature conditions. The rigors of high temperatures could potentially induce alterations in the structural integrity or other inherent properties of the materials, thus demanding a meticulous consideration of the thermal regimen employed. Hence, while the thermal treatment method extends a promising avenue for the synthesis of yolk-shell nanocrystals, particularly those based on metal oxides, a balanced and cautious approach is imperative to ensure the preservation of the desired materials properties amidst the high-temperature synthesis landscape.

1.1.4 Photocatalytic activity

1.1.4.1 Dye degradation

Photocatalysis has ascended to prominence over the past two decades as a formidable contender in ameliorating environmental quandaries, notably in the realm of dyeing wastewater treatment. This pollution mitigation technique flourishes owing to the

robust oxidizing prowess of charge carriers spawned by photocatalysts, which possess the capability to wholly oxidize and dismantle dye molecules, rendering them harmless. The encapsulating architecture of core-shell and yolk-shell nanocrystals has been brought to the fore in numerous studies, underscoring their efficacy in dye degradation aimed at purifying dyeing wastewater. The distinct configuration of core-shell and yolk-shell nanocrystals amplifies the contact between the photocatalysts and dye molecules, thereby augmenting the oxidation and decomposition processes. This burgeoning body of work heralds a promising trajectory for core-shell and yolk-shell nanocrystals in championing the cause of environmental remediation, especially in the battle against the perils posed by dyeing wastewater.

1.1.4.2 H_2 production

The quest for green, alternative energy solutions has propelled the exploration of H_2 production from water splitting using semiconductor photocatalysts, heralding a sustainable path to energy creation. This initiative gained momentum with the seminal demonstration by Fujishima and Honda of water photolysis on TiO_2 photoelectrodes, establishing photocatalytic H_2 production as a crucial goal in the journey of solar energy conversion towards clean energy avenues. Numerous strategies have been devised to augment the efficiency of solar H_2 production. Utilizing unique nanostructures to optimize solar energy harvesting is particularly pivotal as light absorption is the primary process governing the production of charge carriers. In this context, core-shell and yolk-shell nanostructures present an optimal structural platform. The design of yolk-shell facilitates enhanced light harvesting efficiency due to the multi-reflection of incident light within the void space, thus amplifying the generation of charge carriers pivotal for the photocatalytic process. On the other hand, the design of core-shell nanocrystals provides

a robust framework wherein the core acts as a solid support for the shell material, offering enhanced stability and facilitating controlled interactions between the materials. This structure not only allows for effective light absorption but also ensures a conducive environment for charge transfer, which is crucial for the photocatalytic process. The protective shell in core-shell nanostructures serves to shield the core material from potential corrosion, thereby enhancing the durability and effectiveness of the photocatalyst in long-term applications.

Both core-shell and yolk-shell nanostructures open avenues for engineering advanced photocatalysts with superior light harvesting capabilities, efficient charge transfer dynamics, and reduced recombination rates. The strategic employment of these nanostructures could significantly enhance the efficiency of solar H_2 production, bringing us a step closer to realizing the full potential of solar energy conversion in addressing the pressing demand for clean, renewable energy solutions. Through continuous research and development in synthesizing and optimizing these nanostructures, it is envisaged that significant strides will be made towards achieving higher photocatalytic efficiency and advancing the global quest for sustainable energy alternatives.

1.1.4.3 CO_2 reduction

The concentration of CO_2 in atmosphere has been increasing year by year due to the prosperous development of human society. This would cause greenhouse effect and global warming, which arouses general agreement for reducing CO2 emission as well as consuming CO_2 on demand. Photocatalysis on semiconductor nanostructures is a potential manner of converting CO_2 into other high value-added hydrocarbon fuels, such as CH_4, C_2H_6 and CH_3OH. The goal of CO_2 reduction is imitating natural photosynthesis in order to balance the global CO_2 footprint. Many core-shell and yolk-shell nanocrystals

have emerged as promising platforms for advancing CO_2 reduction via photocatalysis, owing to their unique structural attributes that can be engineered to optimize the process. These nanocrystals offer distinct advantages in enhancing the photocatalytic conversion of CO_2 into valuable fuels, harnessing solar energy to drive this environmentally crucial reaction. The core-shell nanostructure embodies a configuration where a core material is encapsulated by a shell material. This design permits a synergistic interaction between the core and shell materials, providing a scaffold for harnessing and transferring solar energy efficiently to the catalytic sites where CO_2 reduction occurs. The shell material can serve as a protective barrier, preserving the integrity of the core material, and at the same time, it can possess catalytic properties that facilitate the CO_2 reduction process. The core material, on the other hand, can be selected to enhance light absorption and charge carrier generation, which are critical for driving the photocatalytic reactions. Yolk-shell nanocrystals, with their unique hollow architecture, present a different set of advantages for photocatalytic CO_2 reduction. The void space within these structures allows for enhanced light harvesting through multiple reflections of incident light, thereby increasing the likelihood of photon absorption and charge carrier generation. Moreover, the distinct separation between the movable core and the permeable shell in yolk-shell nanostructures can provide a conducive environment for the diffusion and interaction of reactants, facilitating the CO_2 reduction process. Both core-shell and yolk-shell nanocrystals can be tailored to incorporate materials with high photocatalytic activity and selectivity towards the desired hydrocarbon products. Furthermore, the flexibility in designing these structures enables the integration of multiple catalytic sites, thereby diversifying the range of producible fuels from CO_2 reduction. The application of core-shell and yolk-shell nanostructures in photocatalytic CO_2 reduction signifies a step

forward in mimicking natural photosynthesis to address the escalating CO_2 levels in the atmosphere. By advancing the design and synthesis of these nanostructures, and exploring their integration in photocatalytic systems, a substantial contribution can be made towards combating climate change. This endeavor not only aligns with the global initiative to reduce CO_2 emissions but also presents an avenue for generating renewable fuels, which is paramount for sustaining the energy demands of our evolving society.

1.1.5 Charge Transfer Dynamics

The efficacy of semiconductor photocatalysts hinges significantly on their intrinsic attributes encompassing light absorption, carrier transfer and recombination, and the kinetics of surface redox reactions. Among these, light absorption is intrinsic to the optical properties of the selected photocatalysts, which can be enhanced through the introduction of dopants and amalgamation of different materials. The dynamics of charge at the interface governs charge transfer and carrier utilization, which are pivotal processes in photocatalytic reactions. Upon light illumination, photoexcited electrons and holes traverse from the bulk of the photocatalysts to the surface region to partake in redox reactions. However, these charge carriers are predisposed to being trapped and recombined before reaching the surface region, thus undermining carrier utilization efficiency and attenuating the photocatalytic performance. This places interfacial charge dynamics as a cardinal factor dictating the overall photocatalytic efficiency. Delving into the mechanisms of how photoexcited charge carriers are transported, trapped, and/or recombined can unveil avenues to optimize the performance of semiconductor photocatalysts. Particularly, forging correlations between interfacial charge dynamics and photocatalytic activity can yield empirical yet actionable insights, aiding in the design of

versatile nanostructures for superior photocatalytic applications. The architecture of core-shell and yolk-shell nanocrystals can be particularly instrumental in mitigating the challenges associated with charge carrier recombination. The spatial separation in yolk-shell nanostructures and the intimate contact between core and shell materials in core-shell nanostructures can promote more efficient charge transfer, thereby reducing recombination rates. Furthermore, the design flexibility of these nanostructures allows for the incorporation of materials and dopants that can modulate the band structure, facilitating enhanced charge separation and transfer. This not only augments light absorption but also ameliorates the kinetics of surface redox reactions, which is crucial for achieving high photocatalytic performance. In essence, a detailed understanding of interfacial charge dynamics coupled with the strategic design of core-shell and yolk-shell nanostructures can significantly propel the advancement of photocatalytic applications. This encompasses not only environmental remediation like dye degradation and CO_2 reduction but also renewable energy generation through solar-driven water splitting for hydrogen production.

1.2 Thesis objectives

In the rapidly evolving field of photocatalysis, core-shell and yolk-shell nanocrystals have emerged as potent agents, demonstrating promising potential in various applications. Their unique structural properties, coupled with the ability to harness light energy for chemical transformations, make them subjects of immense interest. As we strive to achieve more sustainable energy sources and environmental remediation techniques, the study of these nanocrystals becomes increasingly pertinent. The objective of this research is to:

1.2.1 Exploring the effects of different metals paired with Cu_2O on photocatalytic performance.

In materials science, the unique physicochemical properties of metal@Cu_2O core-shell nanocrystals, particularly for photocatalytic applications, have drawn significant attention. This study explores the influence of Ag, Pd, and Au core materials on the degradation of organic pollutants, exemplified by MO. The choice of the metallic core is critical due to:

(a) Localized Surface Plasmon Resonance (LSPR): Ag and Au nanoparticles exhibit strong LSPR effects that enhance the local electromagnetic field, boosting light absorption and charge separation, key for photocatalytic efficiency. Pd, with minimal LSPR, provides a contrast to underscore the impact of LSPR.

(b) Electronic Structure and Band Positioning: The electronic configuration of Ag, Au, and Pd creates varied band alignments with Cu_2O, influencing electron-hole pair dynamics and, consequently, photocatalytic activity.

Additionally, the specialized applications of these nanometals are:

(i) Nano Ag: With excellent electrical conductivity and a robust LSPR effect, nano Ag excels in degrading organic pollutants and in antimicrobial applications.

(ii) Nano Au: Valued for its stability and biocompatibility, nano Au is notable in both photocatalysis and biomedicine, leveraging its LSPR for visible light absorption and potential in biolabeling.

(iii) Nano Pd: Even without pronounced LSPR, nano palladium is renowned for its catalytic efficiency in organic reactions, especially hydrogenation.

Understanding how different metal cores affect photocatalytic properties not only enhances photocatalyst design but also enriches our understanding of core- shell

interactions during photocatalysis. This knowledge is pivotal for the development of more efficient and stable photocatalysts, facilitating the transition from laboratory research to practical application.

1.2.2 Exploring the sustainability and recyclability of nanomaterials used in wastewater treatment.

This research aims to address the challenges associated with the use of powdered nanomaterials in environmental purification by exploring the integration of Au@Cu_2O core-shell nanocrystals onto PET fibers. The objective is to enhance the practicality and efficiency of wastewater treatment processes through the development of advanced composite materials. These functionalized fabrics are expected to harness the photocatalytic properties of Au@Cu_2O nanocrystals while benefiting from the durability and reusability of PET fibers. The study will investigate the following aspects:

(a) Synthesis and Characterization: To synthesize Au@Cu_2O core-shell nanocrystals and uniformly immobilize them onto PET fibers, and to characterize the morphology, structure, and functional groups of the composite material.
(b) Photocatalytic Activity: To evaluate the photocatalytic efficiency of the functionalized PET fabrics in degrading various organic pollutants found in wastewater.
(c) Recyclability and Reusability: To examine the long-term sustainability of the nanocrystal-functionalized PET fabrics by conducting multiple cycles of use and regeneration, analyzing any loss in photocatalytic activity.

1.2.3 Exploring the extension of core-shell to yolk-shell nanocrystals.

With core-shell nanostructures being extensively investigated, this research seeks to advance the field by transitioning to the study of yolk-shell nanocrystal architectures. The objective is to unravel the intricacies of electronic interactions and charge-transfer dynamics within a series of yolk-shell nanocrystals, and to understand their implications for enhanced photocatalytic performance. This study will synthesize four distinct types of yolk-shell nanocrystals: Au@Cu_7S_4, Au@CdS, Au@ZnS, and Au@Ni_3S_4. The research will aim to achieve the following:

(a) Synthesis and Optimization: To develop a robust and reproducible synthesis method for each type of yolk-shell nanocrystal, optimizing conditions to ensure structural integrity and compositional purity.

(b) Structural and Electronic Characterization: To conduct a thorough characterization of the synthesized nanocrystals, employing techniques such as TEM, XRD, UV-Vis, and XPS to ascertain their morphology, crystal structure, and electronic properties.

(c) Charge-Transfer Dynamics: To investigate the charge-transfer mechanisms within the yolk-shell structures, using TRPL to elucidate the role of the Au core and the semiconducting shells in facilitating or impeding electron movement.

1.3 Thesis overview

In the dynamic and increasingly critical domain of photocatalysis, the emergence of core-shell and yolk-shell nanocrystals as pivotal contributors has necessitated an in-depth exploration of their properties, synthesis, and applications. This thesis delves into the multifaceted aspects of these nanocrystals, aiming to offer a comprehensive understanding that could pave the way for sustainable energy solutions and

environmentally beneficial techniques.

In Chapter 1, this chapter sets the stage by elucidating the foundational properties and significance of both core-shell and yolk-shell nanocrystals. By probing into their synthesis techniques, structural intricacies, and electronic interactions, we seek to establish a strong base that underpins their critical role in photocatalysis. The focus is not just on their inherent properties but also on the dynamics that influence their performance in light-driven chemical processes.

In Chapter 2, this chapter zones in on the specific application of Metal@Cu_2O core-shell nanocrystals, particularly in the degradation of methyl orange. Here, we assess their efficiency, scalability, and potential implications in real-world scenarios.

In Chapter 3, this chapter delves into the innovative realm of material functionalization. The spotlight is on the integration of polyethylene terephthalate fabrics with Au@Cu_2O core-shell nanocrystals, examining its potential to drive environmental purification.

In Chapter 4, this chapter embarks on a meticulous exploration of the electronic dynamics intrinsic to yolk-shell nanocrystals. By understanding the nuances of electronic interplay and charge transfer dynamics, we aim to discern strategies that can enhance the photocatalytic efficiency of these nanocrystals.

In Chapter 5, drawing all threads together, this concluding chapter synthesizes the diverse aspects explored throughout the thesis. It presents an integrated perspective on the roles and potential of core-shell and yolk-shell nanocrystals in the broader context of photocatalysis. Furthermore, based on the findings, it charts out forward-looking recommendations, setting the trajectory for future research and potential industrial applications.

1.4 Figures

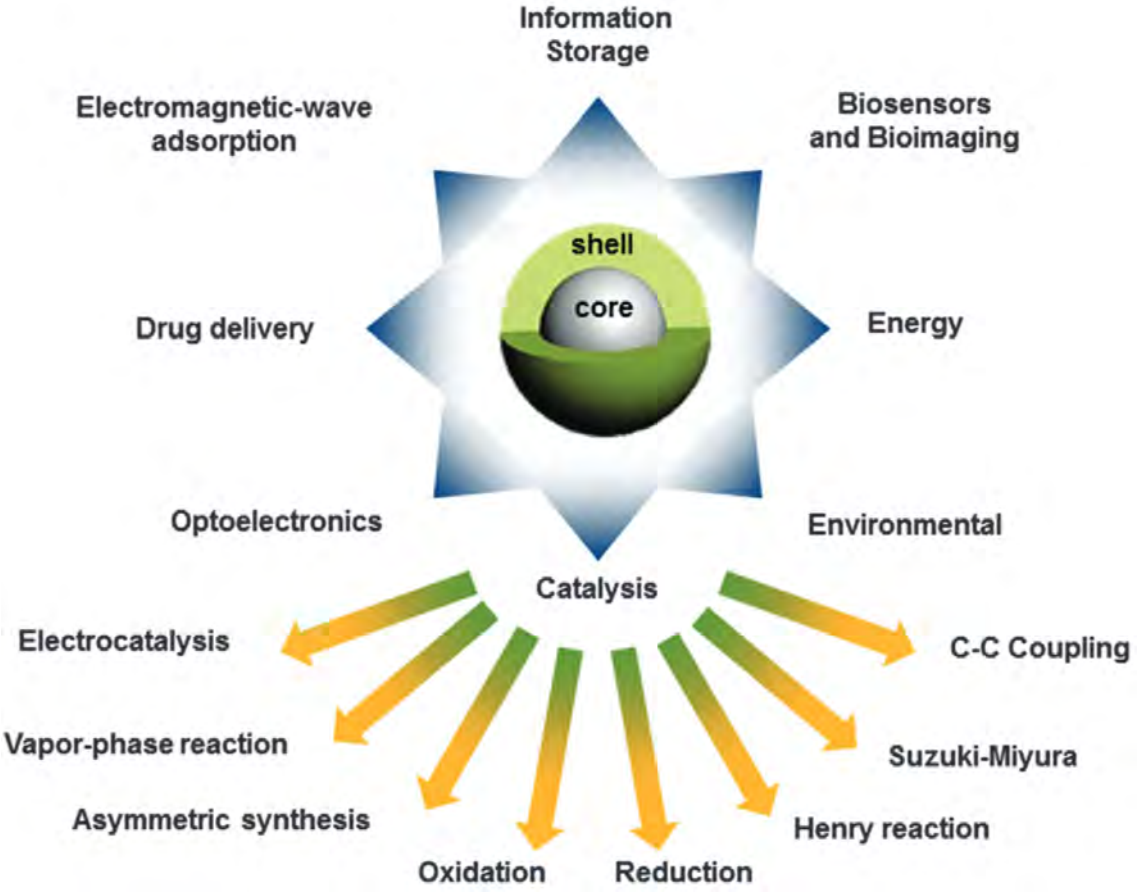

Figure 1-1. Applications of core-shell nanocrystals in various areas of modern technology especially in the field of catalysis.[10]

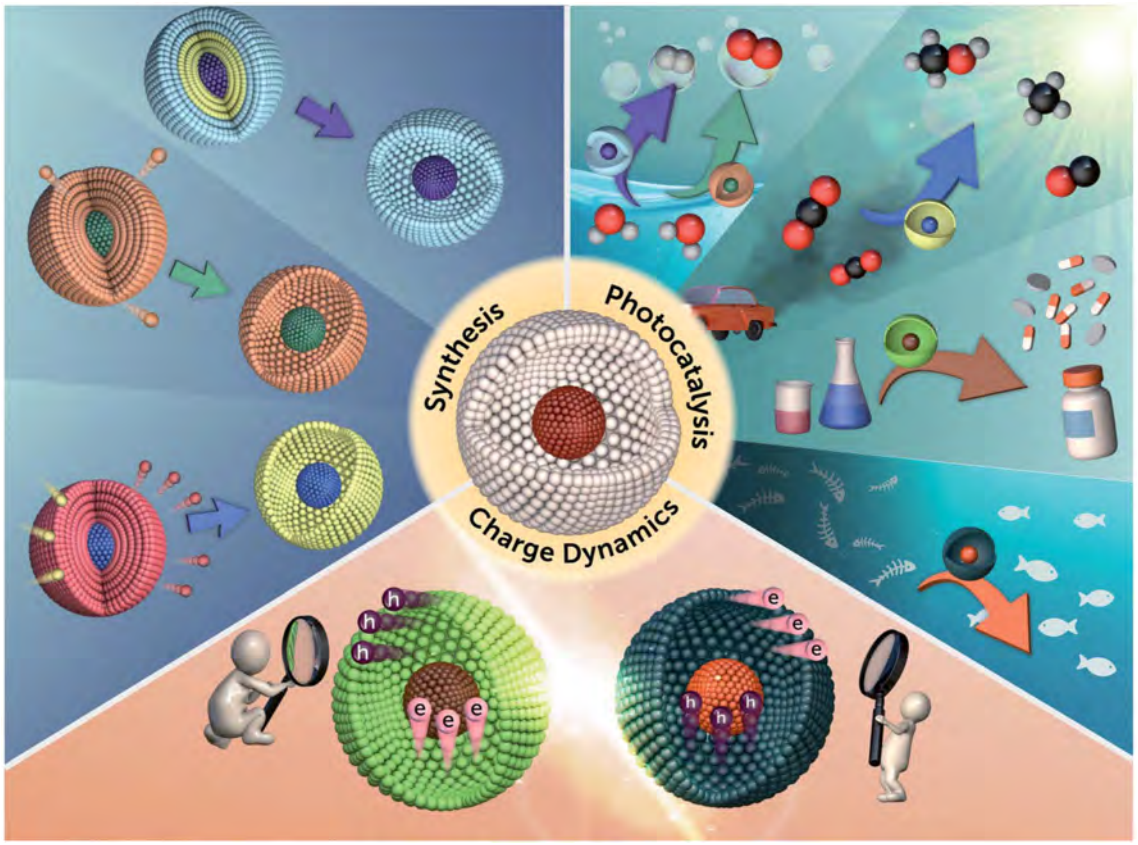

Figure 1-2. Schematic illustration for the synthesis, photocatalysis and charge dynamics of yolk–shell nanocrystals.[9]

1.5 References

[1-1] T. Jafari, E. Moharreri, A. S. Amin, R. Miao, W. Song, S. L. Suib, *Molecules* **2016**, *21*, 900.

[1-2] S. Nahar, M. F. M. Zain, A. A. H. Kadhum, H. A. Hasan, M. R. Hasan, *Materials* **2017**, *10*, 629.

[1-3] D. Li, W. Shi, *Chinese Journal of Catalysis* **2016**, *37*, 792.

[1-4] M. A. Rauf, S. S. Ashraf, *Chemical Engineering Journal* **2009**, *151*, 10.

[1-5] W. Wang, G. Huang, J. C. Yu, P. K. Wong, *Journal of Environmental Sciences* **2015**, *34*, 232.

[1-6] Z. Li, L. Wang, L. Qin, C. Lai, Z. Wang, M. Zhou, L. Xiao, S. Liu, M. Zhang, *Chemosphere* **2021**, *285*, 131432.

[1-7] S. Xu, P. Zhou, Z. Zhang, C. Yang, B. Zhang, K. Deng, S. Bottle, H. Zhu, *J. Am. Chem. Soc.* **2017**, *139*, 14775.

[1-8] A. Shafiee, N. Rabiee, S. Ahmadi, M. Baneshi, M. Khatami, S. Iravani, R. S. Varma, *ACS Appl. Nano Mater.* **2022**, *5*, 55.

[1-9] Y.-A. Chen, Y.-T. Wang, H. S. Moon, K. Yong, Y.-J. Hsu, *RSC Adv.* **2021**, *11*, 12288.

CHAPTER 2

Material Design and Fabrication of Metal@Cu_2O Core–Shell Nanostructures and the Photocatalytic Properties

2.1 Introduction

Due to its direct impact on human health and the ecological environment, water pollution by synthetic dyes has become a significant concern with the rapid development of society and the economy. Several methods for reducing organic dye, such as adsorption,[11] flocculation,[12] coagulation,[13] and sedimentation,[14] have been employed in treating dye wastewater. Nevertheless, it should be noted that the utilization of these procedures may lead to the occurrence of secondary contamination and may not be entirely effective in the full removal of dye molecules. Photocatalysis has emerged as a viable alternative technology with considerable prospects for diminishing water contamination, since it has demonstrated the ability to achieve total degradation of dyes with a high level of efficiency.[15] When photocatalysts are exposed to incoming light of adequate energy, the electrons inside the material become excited and transition to the conduction band (CB), while simultaneously generating holes in the valence band (VB). The photoexcited electrons and holes can diffuse to the surface in order to conduct redox

reactions with the adsorbed molecules. For dye degradation, superoxide ($\cdot O_2^-$) and hydroxyl radicals (·OH), which derive from photoexcited electrons and holes, respectively, are the two primary reactive species responsible for the degradation reactions.[16] These reactive species can decompose dye molecules rapidly and non-selectively. In addition, photosensitization of dye molecules can provide photocatalysts with additional photoexcited electrons and thus additional $\cdot O_2^-$ radicals, which has been demonstrated to be a viable strategy for effective dye degradation.[17]

Researchers continue to be drawn to hybrid nanocrystals due to their exhibited synergistic properties, which are challenging to achieve from their individual components. Extensive efforts have been invested in the design of diverse hybrid nanocrystals., which are motivated not only by the challenge of developing a synthetic system, but also by the fascinating material features. The metal-semiconductor hybrid nanocrystals that can achieve efficient charge separation under light irradiation, a critical component in the photocatalytic process, are of much interest.[18–28] Thus, one of the most exciting processes in materials engineering has been the combining of metal and semiconductor.

With rising worries about environmental pollution and safety, the development of highly effective photocatalysts is more important than ever. For dye degradation, oxide semiconductors such as ZnO,[29] TiO_2,[30] SnO_2[31] and Cu_2O[32] have been widely employed. Cu_2O has been recognized as an attractive photocatalyst option due to its unique features, which include cost effectiveness, versatility in targeting various dyes, and good thermal stability. Recent advancements have revealed the need for metal addition to improve the dye degradation performance of oxide semiconductors. Even though numerous studies have delved into metal@Cu_2O hybrid nanocrystals, there's a noticeable gap in thoroughly studying the dye degradation features, particularly

concerning the impact of metal composition. Therefore, a deeper mechanistic study on this aspect would significantly enrich both the fundamental understanding and practical uses of Cu_2O-based photocatalysts.

In this research, we established a quick and flexible citrate-binding method for generating metal@Cu_2O core-shell nanocrystals,[28] a common form of hybrid nanocrystal. The synthesis, which employed ascorbic acid as the reducing agent, was completed in 5 minutes at 35°C without the usage of capping reagents. To demonstrate the versatility of the synthetic strategy for the formation of metal@Cu_2O core-shell nanocrystals, three different metals (Ag, Pd and Au) were adopted. The effectiveness of the method depended on the presence of citrate ligands on the surface of the metal particle, which facilitated the approach of Cu^{2+} to the metal surface and ensuing Cu^{2+} reduction. Cu_2O deposition might occur entirely on the metal surface as a result of the Cu^{2+}-citrate interaction, leading the formation of metal@Cu_2O core-shell nanocrystals. The photodegradation performance of the materials was investigated with MO as the dye molecules. Many studies have primarily looked into the photocatalytic applications of pure Cu_2O or basic metal@Cu_2O combinations such as Au@Cu_2O. However, investigations into the outcomes of associating Cu_2O with multiple metals are scarce. This research stands out due to its investigation into different metal cores integrated with Cu_2O. The three metal@Cu_2O nanocrystals all shown improved degradation performance as compared to pure Cu_2O, with Au-Cu_2O demonstrating the best MO degradation performance. The mechanism of the charge transfer for metal@Cu_2O nanocrystals and their relationship with metal composition were identified by comparing results for samples with different metal compositions.

2.2 Experimental

2.2.1 Chamicals

Tri-sodium citrate ($C_6H_5Na_3O_7$; 99.0%) and tetrachloroauric (III) acid trihydrate ($HAuCl_4 \bullet 3H_2O$, 99.5%) were purchased from Sigma-Aldrich. Copper (II) sulfate pentahydrate ($CuSO_4 \bullet 5H_2O$; 99.0%), silver nitrate ($AgNO_3$; 99.0%), palladium(II) chloride ($PdCl_2$; 98.0%), hexadecyltrimethylammonium bromide (CTAB; 99%), sodium borohydride ($NaBH_4$; 99%), tanic acid ($C_{76}H_{52}O_{46}$; 99%) and L-ascorbic Acid (LAA; 99.0%) were provided by Kanto Chemical Co., Inc. Sodium hydroxide (NaOH; 99.0%) was purchased from Tokyo Chemical Industry Co., Ltd.

2.2.2 Preparation of Au, Ag, and Pd colloids

The Turkevich method was used to create the citrate-protected Au colloids.[33] In a typical procedure, an aqueous solution of $HAuCl_4$ (100 mL, 0.25 mM) was heated to 100 °C in a reflux system before adding the reducing agent, trisodium citrate (200 L, 0.5 M) The mixed solution was kept at 100 °C for 10 minutes until the colour changed to burgundy red. The resulting Au colloids were naturally cooled to room temperature for further usage.

Ag nanoparticles were synthesized by using a modified version of a previously reported method.[34] In a reflux system, an aqueous solution of $AgNO_3$ (100 mL, 0.25 mM) was first heated to 100 °C, followed by the quick addition of a mixed solution comprising tri-sodium citrate (0.5 mL, 0.2 M) and tannic acid (0.5 mL, 4 mM). After 10 minutes at 100 °C, the reaction solution produced a stable, light-yellow dispersion of Ag nanoparticles. After that, the citrate-protected Ag colloids were cooled to room temperature for future use.

In order to produce Pd nanoparticles,[28] a solution of H_2PdCl_4 (2.5 mL, 10 mM) was initially mixed with a solution of CTAB (94.2 mL, 6.25 mM) at a temperature of 100 °C while undergoing vigorous stirring. Subsequently, a specified volume of ascorbic acid solution (800 μL, 0.1 M) was introduced. The solution containing a mixture of substances conducted a reaction at a temperature of 100 °C for a duration of 10 minutes, resulting in the formation of a stable dispersion of dark-gray Pd nanoparticles. The CTAB-capped Pd nanoparticles were subjected to incubation in a trisodium citrate solution (400 μL, 0.5 M) in order to produce Pd colloids that are protected by citrate.

2.2.3 Preparation of metal@Cu_2O core-shell nanocrystals

Metal@Cu_2O nanocrystals were synthesised utilising a chemical reduction technique.[28] A specific amount of citrate-protected metal colloids (3 mL, 0.25 mM) was added to an aqueous solution containing 0.03 mmol $CuSO_4$. After that, 1.5 mL of 1 M NaOH solution was added, followed by 0.5 mL of 0.1 M L-ascorbic acid solution. To form metal@Cu_2O core-shell nanocrystals, the reaction solution was stirred for 5 minutes at 35 °C. After centrifugation at 7800 rpm for 5 minutes, the products were rinsed with distilled water and ethanol to remove any residual ions and contaminants. Pure Cu2O nanocrystals were also generated in the chemical reduction procedure without the addition of metal colloids for comparison.

2.2.4 Photocatalytic MO degradation

MO is representative of azo dyes, a class of pollutants found in industrial wastewater, particularly from the textile industry. Its widespread use makes it easier to compare results across different studies and materials. Furthermore, based on the band

position of Cu_2O, it is adept at generating $\cdot O_2^-$, making it suitable for MO degradation.[35] In this work, MO was used as a test pollutant in order to assess the photocatalytic efficiency of the metal@Cu_2O. In a standard experimental protocol, the metal@Cu_2O core-shell nanocrystals were placed in a solution of MO in an aqueous medium with a volume of 20 mL and a concentration of 40 μM. This process was carried out within a quartz tube. Following the achievement of adsorption-desorption equilibrium in without the presence of light for a duration of 120 minutes, the reaction solution underwent white light exposure (xenon lamp, 500 mW/cm^2) to facilitate the degradation of the MO molecule. At regular time intervals, a volume of 0.2 mL of the reaction solution was eliminated and then underwent centrifugation. The measurement of absorbance at a wavelength of 464 nm was subsequently conducted in order to determine the variations in the concentration of the residual MO.

2.2.5 Characterization

The microstructural features of the samples were analyzed by a field-emission scanning electron microscope (SEM, Hitachi, SU4300SE) and a high-resolution transmission electron microscope (HRTEM, JEOL, JEM-ARM200FTH) operated at 200 kV. The crystallographic structure and chemical compositions were studied with X-ray diffraction (XRD, Rigaku, Ultima IV) and an energy-dispersive X-ray spectrometer (EDS) installed on the SEM (SU4300SE) and TEM (JEM-ARM200FTH). The chemical states of the samples were analyzed with X-ray photoelectron spectroscopy (XPS, ULVAC-PHI, ESCA1700R) using Al Kα radiation. The recorded binding energies were calibrated to the C 1s peak at 284.8 eV. UV−visible diffuse reflectance spectra (DRS) were obtained from a spectrometer (Shimadzu, UV-2600i) equipped with an integrating sphere. Steady-state PL spectra were collected in a commercial spectroscope (Hitachi, F-7000) using 375

nm as excitation wavelength. Time-resolved PL spectra were obtained in a customized single-photon counting setup, which contains a sub-nanosecond pulsed diode laser (λ_{ex} = 375 nm, PicoQuant, PDL 800-D) and provides an instrument response function down to 25 ps FWHM. The recorded data were fitted with a biexponential kinetics equation to generate two lifetime components (τ_1, τ_2) and the corresponding amplitude contributions (A_1, A_2) along with the goodness of the fitting result (χ^2). The intensity-average lifetime ($\langle\tau\rangle$) was then computed for overall comparison.

2.3 Results and discussion

2.3.1 Morphology and Crystallographic Structure

Metal@Cu_2O was made by depositing a Cu_2O shell across citrate-protected Ag, Pd, and Au particles using the previously described synthetic techniques.[28] SEM was used to characterise the microstructures of the resulting metal@Cu_2O. Pure Cu_2O and the three metal@Cu_2O had comparable microstructural shape, as shown in Figure 1 (a-d). The surface morphology of the four samples, Ag@Cu_2O, Pd@Cu_2O, Au@Cu_2O, and pure Cu_2O, exhibited distinct, yet uniformly distributed nano-features. The morphology of Ag@Cu_2O and Au@Cu_2O is spherical in nature, while Pd@Cu_2O and pure Cu_2O exhibit a square-like structure. This distinction in morphology could potentially influence their photocatalytic performance. In terms of overall size, Ag@Cu_2O nanoparticles manifested an average diameter of 101.20 ± 11.74 nm. In contrast, Pd@Cu_2O and Au@Cu_2O recorded average dimensions of 82.96 ± 8.49 nm and 65.61 ± 9.57 nm, respectively. The pure Cu_2O nanoparticles exhibited an average size of 71.66 ± 7.41 nm. Such disparities in particle sizes could impart distinct surface-to-volume ratios, thereby modulating their reactive interfaces and resultant photocatalytic efficacies.

The carboxyl groups on the surface of citrate-protected Au may coordinate with

the Cu^{2+} ions, allowing for even more uniform Cu_2O deposition on each metal particle. The core composition of metal (Au, Ag, and Pd) and the shell composition of cubic Cu_2O were validated further by TEM-EDS mapping data. Delving deeper into the microstructural details, the Ag core exhibited a size of 24.31 ± 4.18 nm, while the Pd core measured 14.74 ± 3.40 nm, and the Au core was 16.60 ± 1.55 nm. This translated to shell thicknesses of 38.45 ± 6.23 nm for Ag@Cu_2O, 34.11 ± 4.57 nm for Pd@Cu_2O, and 24.51 ± 4.85 nm for Au@Cu_2O. Intriguingly, EDS spectra, as showcased in Fig. 2(d-f), indicated a progressive increase in the Cu/Au ratio, moving from 39.22 in Ag@Cu_2O to 48.15 in Pd@Cu_2O, and culminating at 52.64 in Au@Cu_2O. These quantitative findings are in harmony with the observed microstructural variations.

The chemical compositions of the samples were further analyzed with XRD. Figure 3 depicted the XRD analytic findings, which indicated strong crystallinity for three metal@Cu_2O with core compositions of fcc Pd (JCPDS 46-1043), fcc Au (JCPDS 04-0784), and Ag (JCPDS 04-0783) and shell composition of cubic Cu2O (JCPDS 78-2076). The pattern of pure Cu_2O was also collected, showing the constituent component of cubic Cu_2O. With similar microstructural feature and identical crystallographic structure to metal@Cu2O, pure Cu2O can serve as a righteous control sample for performance comparison in order to reveal the influence of metal core. The average crystallite size of pure Cu_2O sample was determined using XRD data. By focusing on the (111) reflection and employing the Scherrer equation, an estimated grain size of approximately 5.07 nm.

$$D = \frac{K\,\lambda}{\beta\,cos\theta}$$

Where:

- K is the Scherrer constant (0.9 in this study).
- λ is the X-ray wavelength for Cu Kα radiation (1.5418 Å).

- β is the FWHM in radians.
- θ is the Bragg angle in radians.

It's important to highlight that high crystallinity is beneficial for photocatalytic applications. This is because it enhances charge carrier transport, which is crucial for efficient photocatalysis.[36] In Figure 4a, the Ag 3d, Cu 2p, and O 1s spectra analysis revealed the chemical states consistent with metallic Ag and Cu_2O for Ag@Cu_2O. Significantly, compared to pure Ag and pure Cu_2O, Ag@Cu_2O demonstrated marked binding energy shifts in Ag 3d (~0.4 eV), Cu 2p (~0.1 eV), and O 1s (~0.4 eV). This finding underscores the pronounced electronic interactions between Ag and Cu_2O within Ag@Cu_2O.[37] The Ag 3d spectra of Ag@Cu_2O and pure Ag displayed doublet feature characteristic of metallic Ag. The recorded double peaks were located at 374.3 and 368.2 eV for Ag@Cu_2O and 373.9 and 367.8 eV for pure Ag.[37] Particular attention should be paid to the notable overlapping peaks in the Cu 2p and O 1s spectra. Deconvolution of the Cu 2p peaks identified three distinct doublet sets, corresponding to the chemical states of Cu^+ in Cu_2O (952.2 eV for Cu $2p_{1/2}$ and 932.2 eV for Cu $2p_{3/2}$), Cu^{2+} in $Cu(OH)_2$ (955.4 eV for Cu $2p_{1/2}$ and 934.7 eV for Cu $2p_{3/2}$), and the Cu^{2+} satellite (963.5 and 945.3 eV).[38] It is commonly observed that $Cu(OH)_2$ is present on the surface of Cu_2O, potentially resulting from incomplete dehydration during the crystallization process of Cu_2O. In the O 1s spectra of Ag@Cu_2O, doublets were observed for both the lattice oxygen in Cu_2O (532.9 eV) and the surface oxygen of hydroxides (530.7 eV), aligning with the spectral characteristics of Cu_2O crystals.[39] By contrast, pure Cu_2O displayed three sets of Cu 2p doublet peaks, attributable to the Cu^+ state in Cu_2O (952.1 eV for Cu 2p 1/2 and 932.1 eV for Cu 2p 3/2), Cu^{2+} in $Cu(OH)_2$ (954.8 eV for Cu 2p 1/2 and 934.5

eV for Cu 2p 3/2), and the Cu^{2+} satellite (962.7 and 943.4 eV). The O 1s spectra for pure Cu2O also featured doublets representing the lattice oxygen in Cu_2O (532.2 eV) and the surface oxygen in hydroxides (530.3 eV), in line with the crystal spectral nuances of Cu_2O.

In Figure 4b, the Pd 3d, Cu 2p, and O 1s spectra analysis revealed the chemical states consistent with metallic Pd and Cu_2O for Pd@Cu_2O. Significantly, compared to pure Pd and pure Cu_2O, Pd@Cu_2O demonstrated marked binding energy shifts in Pd 3d (~0.6 eV), Cu 2p (~0.3 eV), and O 1s (~0.8 eV). This finding underscores the pronounced electronic interactions between Pd and Cu_2O within Pd@Cu_2O.[40] The Pd 3d spectra of Pd@Cu_2O and pure Pd displayed doublet feature characteristic of metallic Pd. The recorded double peaks were located at 341.9 and 336.8 eV for Pd@Cu_2O and 342.5 and 337.2 eV for pure Pd.[41] Special consideration should be given to the overlapping peaks observed in the Cu 2p and O 1s spectra. Deconvolution of the Cu 2p peaks identified three distinct doublet sets, corresponding to the chemical states of Cu^+ in Cu_2O (952.4 eV for Cu $2p_{1/2}$ and 932.7 eV for Cu $2p_{3/2}$), Cu^{2+} in $Cu(OH)_2$ (954.9 eV for Cu $2p_{1/2}$ and 934.9 eV for Cu $2p_{3/2}$), and the Cu^{2+} satellite (963.5 and 945.3 eV).[38] In the O 1s spectra of Pd@Cu_2O, doublets were observed for both the lattice oxygen in Cu_2O (531.1 eV) and the surface oxygen of hydroxides (534.1 eV), aligning with the spectral characteristics of Cu_2O crystals.[39] In Figure 4c, the Au 4f, Cu 2p, and O 1s spectra analysis revealed the chemical states consistent with metallic Au and Cu_2O for Au@Cu_2O. Significantly, compared to pure Au and pure Cu_2O, Au@Cu_2O demonstrated marked binding energy shifts in Au 4f (~1.8 eV), Cu 2p (~0.1 eV), and O 1s (~0.7 eV). This finding underscores the pronounced electronic interactions between Au and Cu_2O within Au@Cu_2O.[20,42] The Au 4f spectra of Au@Cu_2O and pure Au displayed doublet feature characteristic of metallic Au. The recorded double peaks were located at 86.2 and 82.6 eV for Au@Cu_2O and 88.1 and 84.4

eV for pure Au.[20] The overlapping peaks in the Cu 2p and O 1s spectra warrant special attention. Deconvolution of the Cu 2p peaks identified three distinct doublet sets, corresponding to the chemical states of Cu^{+} in Cu_2O (952.4 eV for Cu $2p_{1/2}$ and 932.7 eV for Cu $2p_{3/2}$), Cu^{2+} in $Cu(OH)_2$ (954.9 eV for Cu $2p_{1/2}$ and 934.9 eV for Cu $2p_{3/2}$), and the Cu^{2+} satellite (963.5 and 945.3 eV).[38] In the O 1s spectra of Au@Cu_2O, doublets were observed for both the lattice oxygen in Cu_2O (532.9 eV) and the surface oxygen of hydroxides (530.7 eV), aligning with the spectral characteristics of Cu_2O crystals.[39] Based on the measured XPS shifts of 0.4 eV for Ag, 0.6 eV for Pd, and 1.8 eV for Au indicate that the electron-trapping capacities of the metal cores differ while interacting with Cu_2O. This suggests that Au exhibits the highest efficacy, followed by Pd, and then Ag.

2.3.2 Chemical States and Electronic Interactions

It should be noted that the investigated core-shell nanocrystals were made up of metal cores (Ag, Pd, and Au) and semiconductor shells (Cu_2O), reflecting a conventional metal semiconductor heterostructure system.[43] Under light irradiation, the electrical interactions between the metal core and semiconductor shell may produce charge-carrier separation, which may then be used for photocatalysis. The samples were further characterized with XPS spectroscopy to explore electronic interactions between the core and shell components. When a metal is introduced, its electrical interaction with Cu_2O influences the transfer of photoexcited electrons, leading to modifications in the photocatalytic activity. Because the work function of the metal core (5.10 eV for Au, 5.30 eV for Pd)[44] is greater than that of the Cu_2O shell (4.8 eV)[45], the metal core can act as an effective electron acceptor for the Cu_2O shell in the current metal@Cu_2O nanocrystals.

As a result, the electrons in conduction band of Cu_2O would preferentially move to metal, leaving numerous holes in Cu_2O to increase hole mobility. The lower work function of Ag (4.3 eV)[44] in Ag@Cu_2O nanocrystals could promote electron transport from Ag to Cu_2O, forming a Schottky barrier at the interface once thermodynamic equilibrium was attained. However, electron transfer from Cu_2O to Ag is possible under irradiation because the Cu_2O conduction band potential was higher than the Fermi level at equilibrium.

2.3.3 Light Absorption and Charge-Transfer Dynamics

In pursuit of elucidating the underlying mechanisms of photocatalysis and optimizing its efficacy, we undertook an in-depth study on the light absorption and charge-transfer dynamics inherent to the samples. Figure 5a presents a comparison of the UV-visible absorption spectra of three metal@Cu_2O composites with those of the respective pure metal and pure Cu_2O samples. The pure Au and pure Ag samples demonstrated a characteristic absorption peak at 525 and 410 nm, respectively, which is consistent with the surface plasmon resonance (SPR) for colloidal Au and Ag. The SPR peak of pure Pd nanoparticles is observed in the UV region, smaller than 300nm, resulting in their visually unremarkable black coloration.[46] When comparing the properties of Au and Ag to those of Au@Cu_2O and Ag@Cu_2O, it was observed that the latter two exhibited a SPR peak at a longer wavelength, namely beyond 650 nm for Au@Cu_2O and beyond 575 nm for Ag@Cu_2O. The observed shift in SPR may be attributed to the higher refractive index of the surrounding Cu_2O (with a refractive index range of 2.8-3.4) compared to the solvent (with a refractive index of 1.33 for H_2O).[23,47] A supplementary absorption peak at around 580 nm can be observed for the metal@Cu_2O.

The excitonic bandgap absorption was also found in pure Cu_2O, leading to a similar absorption characteristic.

In our continued exploration of the charge-transfer kinetics of samples, we delved into their band structures, utilizing both steady-state and time-resolved PL spectroscopy. Figure 6a-c delineates the band structures of the metal@Cu_2O composites. Upon the excitation of electrons from the VB of Cu_2O (-5.37 eV vs. vacuum) to CB (-3.2 eV vs. vacuum), there is a discernible electron migration to Ag, Pd, and Au, attributed to the CB of Cu_2O is positioned higher than these metals. The electron transfer capability can be discussed based on two scenarios. Using Au@Cu_2O as an example, it can be observed that the Fermi level of Au (-5.1 eV vs. vacuum)[44] is situated below the conduction band edge of Cu_2O (-3.2 eV vs. vacuum).[45] Consequently, this configuration induces a downward band bending effect at the interface, leading to a charge-transfer direction that is opposite for photogenerated electrons compared to photoexcited holes. As a result, electron and hole segregation occurs at the interface. The separation of electrons from holes allows for the further suppression of their recombination, resulting in a decrease in the intensity of PL as can been seen in Figure 6d. A comparable charge-transfer scenario was examined for Pd@Cu_2O, since the Fermi levels of Pd (-5.3 eV vs. vacuum)[44] was also more positively positioned than the conduction band of Cu_2O. It is important to acknowledge that the Fermi levels of Au (-5.1 eV vs. vacuum)[44] and Pd (-5.3 eV vs. vacuum)[44] are lower than that of Cu_2O (-4.8 eV vs. vacuum).[45] Consequently, there is a tendency for electrons to undergo transfer from Cu_2O to Au and Pd. In contrast, the element Ag, possessing a comparatively elevated Fermi level of (-4.3 eV vs. vacuum),[44] has an initial propensity to draw electrons from Cu_2O. Nevertheless, when exposed to light, the electrons in Cu_2O are elevated to the conduction band (-3.2 eV vs vacuum).[45]

Consequently, this prompts an electron transfer to Ag.[48]

Upon a thorough discussion of the band structure, we further scrutinized the charge transfer mechanism employing PL measurements. In Figure 6c, the steady-state PL reveals that, compared to pure Cu_2O, the luminescence intensity of Au@Cu_2O exhibited the most significant reduction, followed by Pd@Cu2O and Ag@Cu2O. This distinctly attests to the proficiency of Au in optimizing carrier separation and electron trapping ability. Delving deeper into the interfacial charge transfer kinetics, we studied the time-resolved PL data, as presented in Figure 6e. Notably, against pristine pure Cu_2O, all three core-shell nanocrystals demonstrated hastened PL decay kinetics. This observation provides confirmation that efficient charge separation occurred at the interface between the core and shell. The data were subjected to analysis using a biexponential equation to get more quantitative information.

As summarized in Table 1, two lifetime components (τ_1 and τ_2) along with the corresponding amplitude contributions (A_1 and A_2) were computed. The long (τ_1) and short (τ_2) lifetime components can be respectively assigned to the charge-carrier relaxation via radiative and nonradiative pathways.[20,49] Several significant points may be stated here. First, as compared to pure samples, the three core-shell samples all had a shorter long lifetime component (τ_1) and a lower amplitude contribution (A_1). This result demonstrated that the presence of a metal core can prevent charge carrier radiative recombination. Second, for core-shell samples, the amplitude contribution of the short lifetime component (A_2) was found to be higher. This discovery indicated that additional nonradiative charge transfer occurred within the core-shell nanocrystals, probably due to interfacial charge transfer between the semiconductor shell and metal core. Third, the three core-shell samples had a shorter average carrier lifetime than their pure counterparts

($\langle\tau\rangle$ = 5.88, 5.22, and 5.13 ns for Ag@Cu_2O, Au@Cu_2O, and Pd@Cu_2O vs $\langle\tau\rangle$ = 6.04 ns for pure Cu_2O). By assuming that charge transfer between the semiconductor shell and metal core accounted for the observed rapid PL decays of core-shell nanocrystals, the interfacial charge-transfer rate constant (k_{ct}) can be computed by the following equation:[20]

$$k_{et} = \frac{1}{<\tau>}(metal@Cu_2O) - \frac{1}{<\tau>}(pure\ Cu_2O)$$

For Ag@Cu_2O, Pd@Cu_2O, and Au@Cu_2O, the calculated k_{ct} values were 0.45×10^7, 2.60×10^7, and 2.94×10^7 s^{-1}, respectively. The findings from time resolved PL spectroscopy, together with the analytical results of XPS spectra, revealed significant electronic interactions and effective charge-carrier separation between the core and shell components for the three core-shell nanocrystal samples. The obtained highest k_{ct} value for Au@Cu_2O signified that charge carrier separation was much effective, giving rise to the promising potential use of Au@Cu_2O as a highly efficient photocatalyst.

2.3.4 Photocatalytic properties

By virtue of the photocatalytic potential of metal@Cu_2O, the sample could conduct a variety of photocatalytic reactions. The photocatalytic degradation of MO was used as the model reaction to show the application scenario in environmental purifications. Figure 7 compares the photocatalytic MO degradation results over all samples. The rate constant of MO degradation could be calculated using pseudo first-order kinetics, providing 7.43, 9.40, 18.55, and 0.82×10^{-3} min^{-1} for Ag@Cu_2O, Pd@Cu_2O, Au@Cu_2O, and pure Cu_2O, respectively. Notably, pure Cu_2O had relatively poor photocatalytic activity. Pure Cu_2O is photocatalytically active, however its photocatalytic performance was typical due to the low carrier utilization efficiency caused by electron-hole recombination. Metal@Cu_2O shown significantly improved photocatalytic activity towards MO

decomposition as compared to pure Cu_2O. The significant charge separation produced by the band alignment between Au and Cu_2O was attributed to this improvement. The photocatalytic performance of Au@Cu_2O was the best of the three metal@Cu_2O. The Au core can attract more electrons in Au@Cu_2O, increasing the overall amount of photoexcited charge carriers.

2.4 Chapter summary

In this work, we investigated the synthesis, characterisation, and photocatalytic application of metal@Cu_2O core-shell nanocrystals, with the goal of addressing the ongoing problem of synthetic dye pollution in wastewater. We intended to study the effect of core composition on photocatalytic effectiveness by cleverly utilising three unique metal cores (Pd, Au, and Ag). Our extensive characterization approaches, which included SEM, TEM-EDS, XRD, and XPS, revealed the distinctive morphological and electrical features of nanocrystals, providing fundamental insights into their behaviour under photocatalytic circumstances. Notably, the Au@Cu_2O nanocrystal emerged as a contender, demonstrating unrivalled degradability of MO. The increased charge separation enabled by the strategic interplay between the Au core and the Cu_2O shell is responsible for the higher performance. Furthermore, our detailed investigation of charge-transfer kinetics, supported by steady-state and time-resolved PL spectroscopy, confirmed our findings and gave a clear picture of the underlying processes. In summary, this study not only provides a possible answer to a pressing environmental issue, but it also sets the framework for future efforts aimed at optimising and expanding the uses of hybrid nanocrystal-based photocatalysts.

2.5 References

[2-1] M. B. Wazir, M. Daud, F. Ali, M. A. Al-Harthi, *J. Mol. Liq.* **2020**, *315*, 113775.

[2-2] A. K. Verma, R. R. Dash, P. Bhunia, *J. Environ. Manage.* **2012**, *93*, 154.

[2-3] A. Y. Zahrim, C. Tizaoui, N. Hilal, *Desalination* **2011**, *266*, 1.

[2-4] E. J. Weber, R. L. Adams, *Environ. Sci. Technol.* **1995**, *29*, 1163.

[2-5] Y. Zhao, Y. Li, L. Sun, *Chemosphere* **2021**, *276*, 130201.

[2-6] Y.-H. Chiu, Tso-Fu Chang, C.-Y. Chen, M. Sone, Y.-J. Hsu, *Catalysts* **2019**, *9*, 430.

[2-7] H. Zhao, Y. Zhang, G. Li, F. Tian, H. Tang, R. Chen, *RSC Adv.* **2016**, *6*, 7772.

[2-8] M.-J. Fang, Y.-C. Lin, J.-Y. Jan, T.-H. Lai, P.-Y. Hsieh, M.-Y. Kuo, Y.-H. Chiu, C.-W. Tsao, Y.-A. Chen, Y.-T. Wang, Y.-J. Hong, J.-Y. Wu, Y. C. S. Wu, Y.-G. Lin, T.-F. M. Chang, C.-Y. Chen, M. Sone, S.-M. Chang, C.-L. Chang, Y.-J. Hsu, *Appl. Catal. B Environ.* **2023**, *324*, 122198.

[2-9] T.-G. Vo, G.-S. Tran, C.-L. Chiang, Y.-G. Lin, H.-E. Chang, H.-H. Kuo, C.-Y. Chiang, Y.-J. Hsu, *Adv. Funct. Mater.* **2023**, *33*, 2209386.

[2-10] T.-H. Lai, C.-W. Tsao, M.-J. Fang, J.-Y. Wu, Y.-P. Chang, Y.-H. Chiu, P.-Y. Hsieh, M.-Y. Kuo, K.-D. Chang, Y.-J. Hsu, *ACS Appl. Mater. Interfaces* **2022**, *14*, 40771.

[2-11] J.-Y. Wu, T.-H. Lai, M.-J. Fang, J.-Y. Chen, M.-Y. Kuo, Y.-H. Chiu, P.-Y. Hsieh, C.-W. Tsao, H.-E. Chang, Y.-P. Chang, C.-Y. Wang, C.-Y. Chen, M. Sone, W.-W. Wu, T.-F. M. Chang, Y.-J. Hsu, *ACS Appl. Nano Mater.* **2022**, *5*, 8404.

[2-12] Y.-H. Chiu, S. B. Naghadeh, S. A. Lindley, T.-H. Lai, M.-Y. Kuo, K.-D. Chang, J. Z. Zhang, Y.-J. Hsu, *Nano Energy* **2019**, *62*, 289.

[2-13] M.-Y. Kuo, C.-F. Hsiao, Y.-H. Chiu, T.-H. Lai, M.-J. Fang, J.-Y. Wu, J.-W. Chen, C.-L. Wu, K.-H. Wei, H.-C. Lin, Y.-J. Hsu, *Appl. Catal. B Environ.* **2019**, *242*, 499.

[2-14] Y.-C. Pu, W.-T. Chen, M.-J. Fang, Y.-L. Chen, K.-A. Tsai, W.-H. Lin, Y.-J. Hsu, *J. Mater. Chem. A* **2018**, *6*, 17503.

[2-15] Y.-H. Chiu, K.-D. Chang, Y.-J. Hsu, *J. Mater. Chem. A* **2018**, *6*, 4286.

[2-16] Y.-H. Chiu, Y.-J. Hsu, *Nano Energy* **2017**, *31*, 286.

[2-17] W.-H. Lin, Y.-H. Chiu, P.-W. Shao, Y.-J. Hsu, *ACS Appl. Mater. Interfaces* **2016**, *8*, 32754.

[2-18] Y.-K. Lin, Y.-J. Chiang, Y.-J. Hsu, *Sens. Actuators B Chem.* **2014**, *204*, 190.

[2-19] V. Batra, I. Kaur, D. Pathania, Sonu, V. Chaudhary, *Appl. Surf. Sci. Adv.* **2022**, *11*, 100314.

[2-20] U. G. Akpan, B. H. Hameed, *J. Hazard. Mater.* **2009**, *170*, 520.

[2-21] G. Elango, S. M. Roopan, *J. Photochem. Photobiol. B* **2016**, *155*, 34.

[2-22] Q. Su, C. Zuo, M. Liu, X. Tai, *Molecules* **2023**, *28*, 5576.

[2-23] J. Polte, T. T. Ahner, F. Delissen, S. Sokolov, F. Emmerling, A. F. Thünemann, R. Kraehnert, *J. Am. Chem. Soc.* **2010**, *132*, 1296.

[2-24] Y. Cheng, F. Wang, C. Fang, J. Su, L. Yang, *J. Alloys Compd.* **2016**, *658*, 684.

[2-25] C.-Y. Chu, M. H. Huang, *J. Mater. Chem. A* **2017**, *5*, 15116.

[2-26] R. Marschall, *Adv. Funct. Mater.* **2014**, *24*, 2421.

[2-27] L. Yuan, Z. Geng, J. Xu, F. Guo, C. Han, *Adv. Funct. Mater.* **2021**, *31*, 2101103.

[2-28] H.-L. Yip, A. K.-Y. Jen, *Energy Environ. Sci.* **2012**, *5*, 5994.

[2-29] C.-S. Tan, S.-C. Hsu, W.-H. Ke, L.-J. Chen, M. H. Huang, *Nano Lett.* **2015**, *15*, 2155.

[2-30] S. Sheng, Y. Ren, S. Yang, Q. Wang, P. Sheng, X. Zhang, Y. Liu, *ACS Omega* **2020**, *5*, 17703.

[2-31] I. Platzman, R. Brener, H. Haick, R. Tannenbaum, *J. Phys. Chem. C* **2008**, *112*,

1101.

[2-32] W. Zhang, X. Yang, Q. Zhu, K. Wang, J. Lu, M. Chen, Z. Yang, *Ind. Eng. Chem. Res.* **2014**, *53*, 16316.

[2-33] L. Li, X. Chen, Y. Wu, D. Wang, Q. Peng, G. Zhou, Y. Li, *Angew. Chem. Int. Ed.* **2013**, *52*, 11049.

[2-34] F. Guo, C. Xie, H. Zhao, Y. Gao, H. Teng, E. Han, *Catal. Lett.* **2023**.

[2-35] X. Huang, H. Li, Y. Zhang, R. Wu, L. Ban, L. Xi, Z. Yin, J. Peng, Y. Zhao, L. Fang, *Nanoscale* **2022**, *14*, 13248.

[2-36] W. Niu, Z.-Y. Li, L. Shi, X. Liu, H. Li, S. Han, J. Chen, G. Xu, *Cryst. Growth Des.* **2008**, *8*, 4440.

[2-37] K.-H. Yang, S.-C. Hsu, M. H. Huang, *Chem. Mater.* **2016**, *28*, 5140.

[2-38] S. Ghose, S. Singh, T. S. Bhattacharya, *ACS Appl. Mater. Interfaces* **2020**, *12*, 7727.

[2-39] H. Wu, Z. Zheng, C. Ying Toe, X. Wen, J. N. Hart, R. Amal, Y. Hau Ng, *J. Mater. Chem. A* **2020**, *8*, 5638.

2.6 Figures

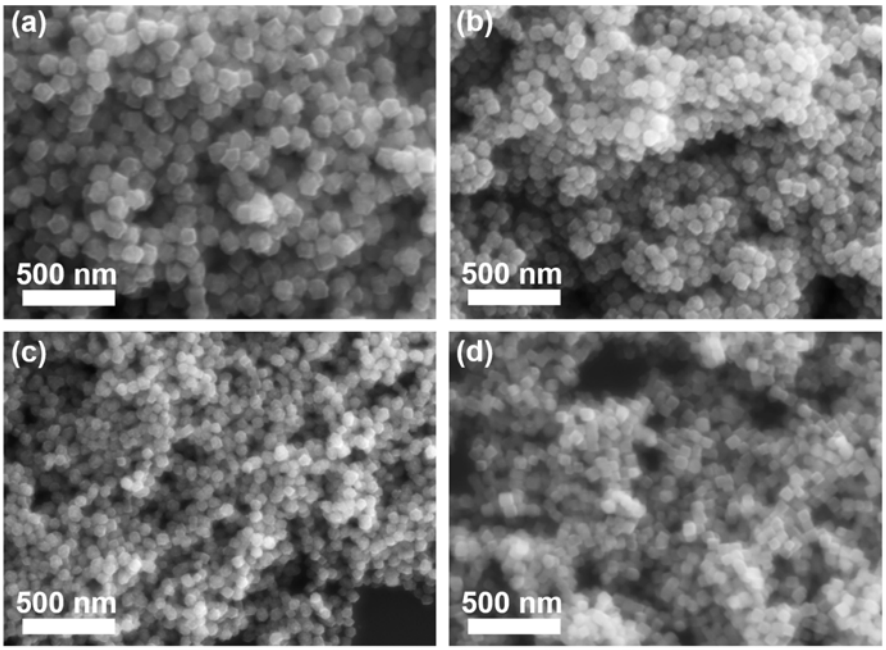

Figure 2-1. SEM images for (a) Ag@Cu_2O, (b) Pd@Cu_2O, (c) Au@Cu_2O, and (d) pure Cu_2O

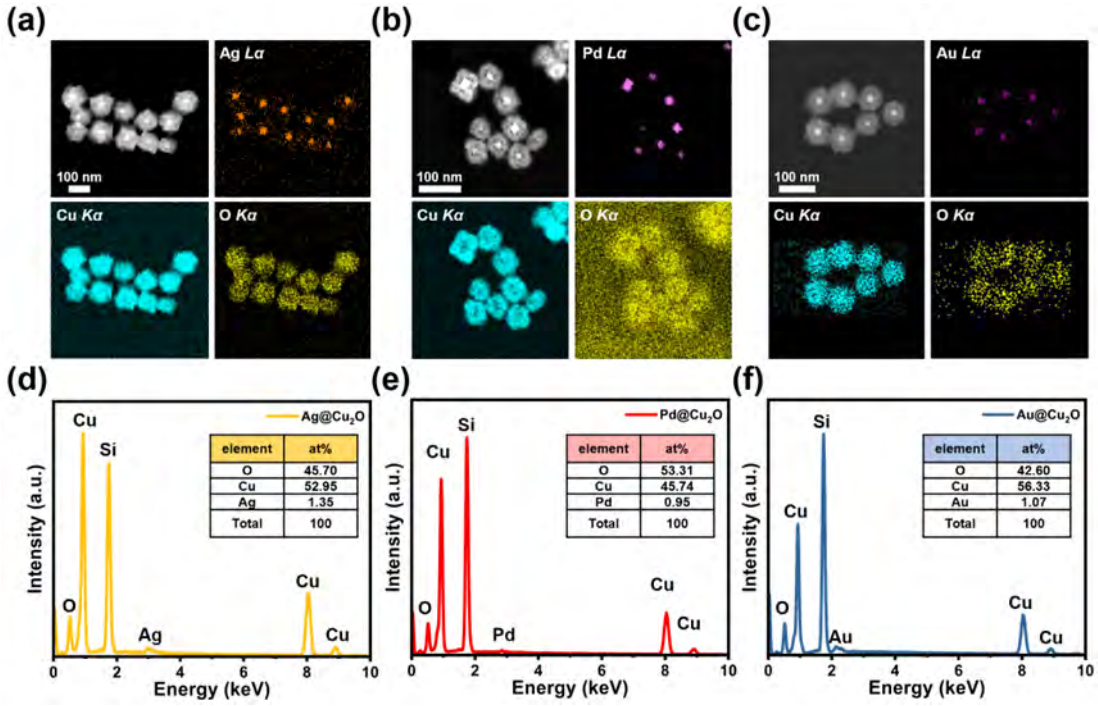

Figure 2-2. TEM-EDS mapping analysis for (a) Ag@Cu_2O, (b) Pd@Cu_2O, (c) Au@Cu_2O, and corresponding spectra for (d) Ag@Cu2O, (e) Pd@Cu_2O, and (f) Au@Cu_2O

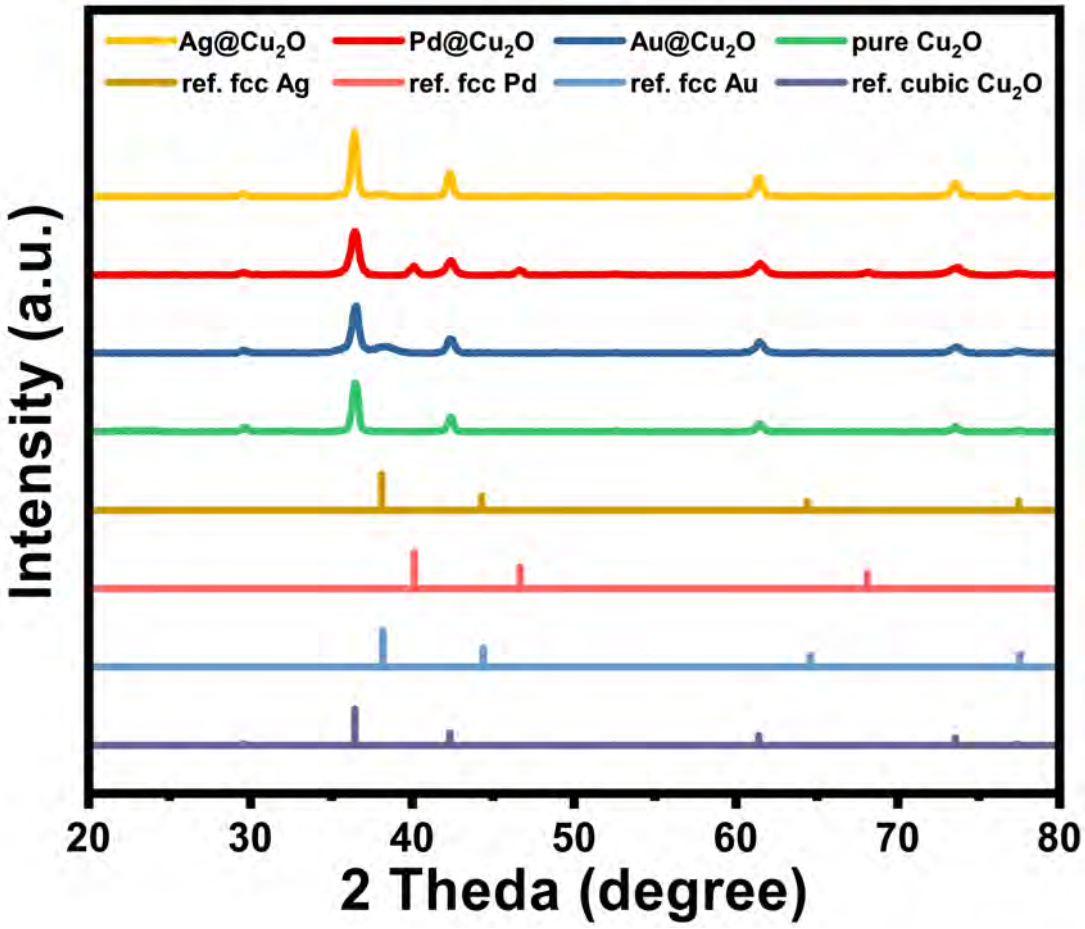

Figure 2-3. XRD patterns for Ag@Cu_2O, Pd@Cu_2O, Au@Cu_2O, and pure Cu_2O.

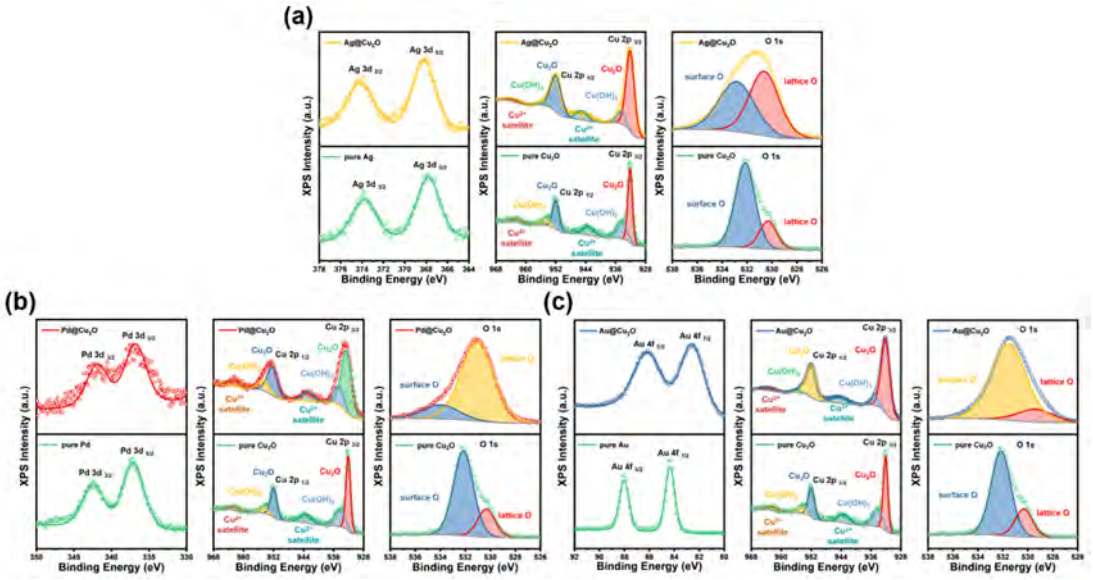

Figure 2-4. (a) Ag 3d, Cu 2p and O 1s XPS spectra for Ag@Cu_2O, pure Ag, and pure Cu_2O. (b) Pd 3d, Cu 2p and O 1s XPS spectra for Pd@Cu_2O, pure Pd, and pure Cu_2O. (c) Au 4f, Cu 2p and O 1s XPS spectra for Au@Cu_2O, pure Au, and pure Cu_2O.

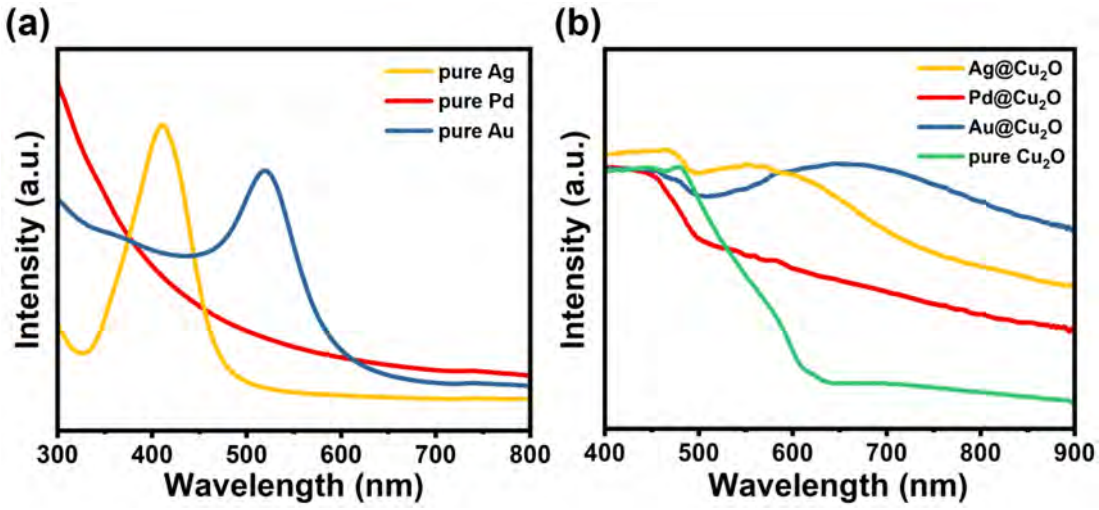

Figure 2-5. UV−visible DRS spectra of (a) pure Ag, pure Pd, and pure Au (b) Ag@Cu_2O, Pd@Cu_2O, Au@Cu_2O and pure Cu_2O.

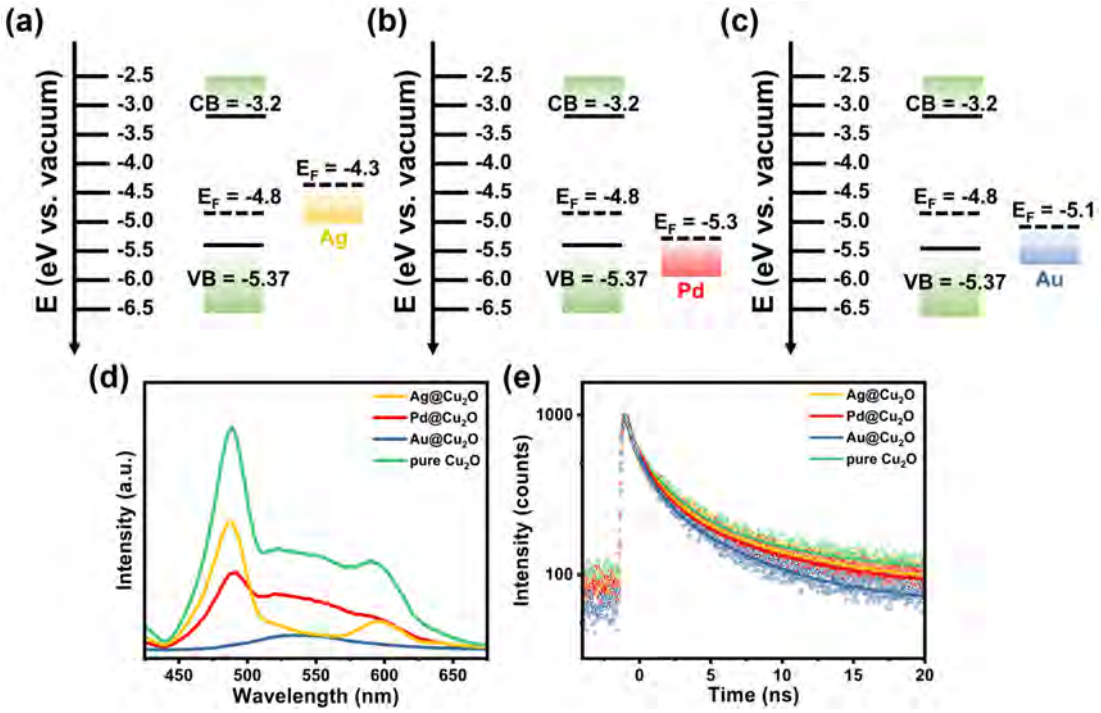

Figure 2-6. Proposed band structure of (a) Ag@Cu_2O, (b)Pd@Cu_2O, (c)Au@Cu_2O, (d) Steady-state PL spectra of all samples, and (e) Time-resolved PL spectra of all samples.

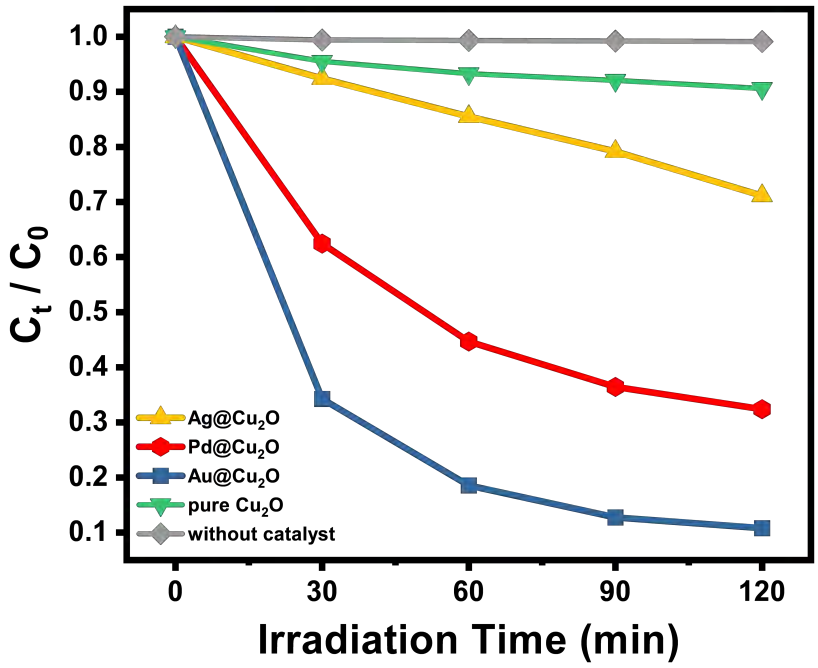

Figure 2-7. Comparative results of photocatalytic MO degradation by using Pd@Cu_2O, Au@Cu_2O, Ag@Cu_2O and pure Cu_2O.

2.7 Tables

Table 2-1. Fitted Parameters of Time-Resolved PL Data for All of the Samples

entry	A_1 (%)	τ_1 (ns)	A_2 (%)	τ_2 (ns)	χ^2	$\langle\tau\rangle$ (ns)	$k_{ct}(s^{-1})$
pure Cu_2O	72.68	7.57	27.32	1.97	1.00	6.04	-
Ag@Cu_2O	71.64	7.56	28.36	1.65	1.01	5.88	0.45×10^7
Pd@Cu_2O	71.35	6.76	28.65	1.40	1.00	5.22	2.60×10^7
Au@Cu_2O	69.18	6.79	30.82	1.40	1.01	5.13	2.94×10^7

CHAPTER 3

Effects of shell thickness in Au@Cu_2O core-shell nanocrystals for photodegradation

3.1 Introduction

In the endeavor to mitigate the proliferation of environmental pollutants, photocatalysis has emerged as a formidable technology, harnessing the inexhaustible energy of sunlight to decompose organic contaminants. Core-shell nanocrystals, particularly Au@Cu_2O with their distinctive gold core and semiconductor oxide shell, have been the subject of extensive research due to their promising applications in photocatalytic degradation. The efficiency of these nanocrystals is often dictated by the precise engineering of their structural features, among which the shell thickness plays a critical role. The Au core induces a plasmonic effect, while the Cu_2O shell facilitates visible light absorption and charge transfer, essential for photocatalytic processes. This intricate interplay can be finely adjusted by tailoring the shell thickness, thus directly influencing the photodegradation capabilities of nanocrystal.

However, the practical deployment of these potent photocatalysts in powder form is hampered by inherent recovery challenges post-photocatalysis, which lead to secondary contamination and catalyst loss. The quest for sustainable application of these materials

necessitates a design that not only preserves the intrinsic activity but also allows for simple recovery and reuse. The immobilization of photocatalyst powders onto substrates is a viable approach to this end. Within this context, polyethylene terephthalate (PET) fabrics emerge as an excellent substrate for immobilizing photocatalytic nanoparticles. PET offers remarkable chemical resilience and mechanical integrity, making it an ideal scaffold for the attachment of photocatalyst powders. Its adaptability, combined with environmental sustainability, presents a solution to the recuperation issue of photocatalytic powders, thus opening new avenues for the broader application of photocatalysis in environmental remediation.

This chapter explores the synthesis and application of Au@Cu_2O core-shell nanocrystals with controlled shell thicknesses immobilized on PET fabrics. We provide a comprehensive investigation of the physicochemical interplay between the shell thickness of nanocrystals and their photocatalytic efficiency when supported by PET substrates.

3.2 Experimental

3.2.1 Chemicals

Tri-sodium citrate ($C_6H_5Na_3O_7$; 99.0%) and tetrachloroauric (III) acid trihydrate ($HAuCl_4 \cdot 3H_2O$, 99.5%) were purchased from Sigma-Aldrich. Copper (II) sulfate pentahydrate ($CuSO_4 \cdot 5H_2O$; 99.0%), silver nitrate ($AgNO_3$; 99.0%), 1,4-benzoquinone (BQ; 99.0%), ethylenediaminetetraacetic acid (EDTA; 99.0%), isopropyl alcohol (IPA; 99.5%) and L-ascorbic Acid (LAA; 99.0%) were provided by Kanto Chemical Co., Inc. Sodium hydroxide (NaOH; 99.0%) was purchased from Tokyo Chemical Industry Co., Ltd. Polyethylene terephthalate (PET) fabrics (thickness 0.079 mm, size 100 cm × 120 cm) were purchased from JSA Group.

3.2.2 Preparation of Au colloids

The citrate-protected Au colloids were prepared using the well-known Turkevich method.[1] In a typical approach, an aqueous solution of $HAuCl_4$ (100 mL, 0.25 mM) was first heated to 100 °C in a reflux system, followed by an addition of the reducing agent, trisodium citrate aqueous solution (200 μL, 0.5 M). The mixed solution was maintained at 100 °C for 10 min until the colour changed to wine red. The resulting Au colloids were naturally cooled to room temperature for further usage.

3.2.3 Preparation of Au@Cu2O core-shell nanocrystals

Cu_2O was deposited on the surface of the Au particles using the chemical reduction method.[2] Briefly, a given amount of NaOH solution (1.5 mL, 1.0 M) was added to 35 mL deionized water in a beaker, followed by a successive addition of $CuSO_4$ (4.0, 3.0, or 2.0 mL, 0.01 M), Au colloids (3.0 mL, 0.25 mM), and LAA (0.5 mL, 0.1 M). After 2 min of stirring at 35 °C, the reaction solution was centrifuged and repeatedly rinsed with deionized water to precipitate the product. In this work, three $CuSO_4$ amounts (2.0, 3.0, and 4.0 mL) were respectively employed to prepare for Au@Cu_2O with increasing shell thicknesses. The resulting samples were denoted as Au@Cu_2O-2, Au@Cu_2O-3, and Au@Cu_2O-4, respectively. Note that Au served as the core for Cu_2O deposition. Under a situation of a fixed Au concentration, addition of more $CuSO_4$ would result in more Cu_2O deposition, leading to an increase in Cu_2O shell for Au@Cu_2O. For comparison purpose, pure Cu_2O nanocrystals were also prepared by using the same procedure without the addition of Au colloids.

3.2.4 Immobilization of Au@Cu_2O on PET

Firstly, a 3 cm × 3 cm piece of PET fabrics was fabricated and placed in a mixed solution composed of ethanol and acetone in a 1:1 volume ratio. After sonicated at 50 °C for 30 min, the PET piece was taken out and dried. Subsequently, the PET piece was immersed in a 10.0 mL methanol solution containing 5.0 mg Au@Cu_2O nanocrystals. After sonicated at 50 °C for 2 h, the Au@Cu_2O-functionalized PET was taken out and dried in a vacuum oven at 40 °C. Pure Cu_2O and pure Au with an equivalent amount to Au@Cu_2O were also immobilized on PET fabrics by using the same procedure.

3.2.4 Photocatalytic MO degradation

MO was employed as a test pollutant to evaluate the photocatalytic performance of the functionalized PET. In a typical procedure, the Au@Cu_2O-functionalized PET fabrics were immersed in a MO aqueous solution (20 mL, 40 μM) in a quartz tube. After achieving adsorption-desorption equilibrium in darkness for 120 min, the reaction solution was subject to white light illumination (xenon lamp, 500 mW/cm^2) for carrying out MO degradation. At specific time intervals, 0.2 mL of the reaction solution was extracted and centrifuged. The absorbance at λ = 464 nm was then measured to determine the variation in concentration of the residual MO. The calibration curve of MO solutions was obtained by using the external standard method. As displayed in Supplementary Figure S1, the linear regression of the calibration curve in the linear range gave a slope of 0.026 mM^{-1}, i.e. the calibration sensitivity, and a linearity of 0.9995, also known as the correlation coefficient. The standard deviation of the blank test on pure water was 0.00015. By using a signal-to-noise ratio of 3.3, the limit of detection was determined to be 0.019 mM. By using a signal-to-noise ratio of 10, the limit of quantification was determined to be 0.058 mM. The linear dynamic range was found to distribute from 0.019 mM, the

detection limit, to 80 mM, the concentration beyond which the calibration curve deviates from linearity. In this work, the employed MO concentration was determined by comparing the photocatalytic activity of the functionalized PET at various MO concentrations. Comparative results showed that 40 μM was the optimal concentration of MO for maximizing the photocatalytic performance for the functionalized PET. This MO concentration has also been employed in other studies related to photocatalysis.[3,4]

3.2.5 Photocatalytic MB degradation

The experimental procedures of photocatalytic MB degradation were identical to the case of MO degradation except that the employed MB concentration was 20 μM.

3.2.6 Photocatalytic simulated textile wastewater degradation

The experimental procedures of photocatalytic degradation of simulated textile wastewater were identical to the case of MO degradation except that the simulated textile wastewater was prepared according to the recipe reported in literature.[5]

3.2.6 Scavenger experiments

In order to identify the main reactive species, four kinds of radical scavengers (1 mM), including $AgNO_3$, EDTA, IPA, and BQ,[5] were employed to respectively trap electrons, holes, ·OH and $\cdot O_2^-$ produced from the functionalized PET during the degradation process of MO. In a typical procedure, a given concentration of scavenger (1 mM) was added to the reaction solution of photocatalytic MO degradation. The variation in MO concentration was then monitored and compared with the result without the employment of radical scavengers.

3.2.7 Photoelectrochemical measurements

Photoelectrochemical (PEC) measurements were conducted in a three-electrode cell consisting of a Pt foil counter electrode, an Ag/AgCl (saturated KCl) reference electrode and a 0.5 M Na_2SO_4 aqueous electrolyte (pH = 6.5). The working electrode was prepared by uniformly drop-casting a given amount of nanocrystals suspension onto the fluorine-doped tin oxide (FTO) substrate. The conductive Ag paste was used to adhere Cu wires to the FTO substrate, and all of contacts were meticulously sealed with epoxy resin. The chronoamperometry data (I−t curves) were collected on a potentiostat (Autolab, PGSTAT204). A solar simulator (Newport, LCS-100, 94011A) composed of a xenon lamp and a AM 1.5 G filter was used as the irradiation source (100 mW/ cm^2). Incident photon-to-electron efficiency (IPCE) measurements were conducted using a xenon lamp coupled with a monochromator (HORIBA, Tunable PowerArc, 0.2 m, 1200 g/mm, dispersion = 5 nm).

3.2.8 Characterizations

The microstructural features of the samples were analyzed by a field-emission scanning electron microscope (SEM, Hitachi, SU4300SE) and a high-resolution transmission electron microscope (HRTEM, JEOL, JEM-ARM200FTH) operated at 200 kV. The crystallographic structure and chemical compositions were studied with X-ray diffraction (XRD, Rigaku, Ultima IV) and an energy-dispersive X-ray spectrometer (EDS) installed on the SEM (SU4300SE) and TEM (JEM-ARM200FTH). The chemical states of the samples were analyzed with X-ray photoelectron spectroscopy (XPS, ULVAC-PHI, ESCA1700R) using Al Kα radiation. The recorded binding energies were calibrated to

the C 1s peak at 284.8 eV. UV-visible absorption spectra were obtained from a spectrometer (Apel, PD-3000UVe). Steady-state photoluminescence (PL) spectra were collected in a customized spectroscope (Horiba, FluoroMax-3) using 375 nm as excitation wavelength. Fourier-transform infrared spectroscope (FTIR, Thermo Scientific, Nicolet iS10) was utilized to analyze the vibration frequency of C=O stretching of PET.

3.3 Results and discussion

3.3.1 Structural characteristics and optical properties

Au@Cu_2O was prepared by depositing a Cu_2O shell on the citrate-protected Au particles by following the previous reported synthetic procedures.[7] The microstructural features of the resultant Au@Cu_2O were first characterized with TEM. The Au particles produced from the citrate reduction method showed a homogeneous size distribution of 15.3 ± 1.4 nm. The carboxyl groups at the surface of the citrate-protected Au can coordinate with the Cu^{2+} ions, enabling the further uniform deposition of Cu_2O on each Au particles.[8] As shown in Figure 1(a), the high structural integrity of core@shell morphology without the existence of non-coated Au and arbitrarily grown Cu_2O can be identified. This outcome highlighted the reliability of the developed synthetic procedure for the preparation of highly uniform Au@Cu_2O. The lattice resolved high-resolution TEM image in Figure 1(b) and the corresponding EDS mapping data in Figure 1(c) further confirmed the core composition of fcc Au and shell composition of cubic Cu_2O.

The Au@Cu_2O was then immobilized on the PET fabrics by immersing PET in the methanolic suspension of Au@Cu_2O. As Figure 2(a-b) shows, the immobilized Au@Cu_2O was evenly distributed on the PET fabrics in a large scale. Note that the surface of the as-synthesized Au@Cu_2O was capped with hydroxyl group originating from the ascorbic acid [9,10] added during the deposition of Cu_2O. These hydroxyl moieties can

form hydrogen bonds with the carbonyl group of PET [11,12], providing a substantial binding force between Au@Cu_2O and PET. This feature may guarantee the firm immobilization of Au@Cu_2O on PET, which can avoid the significant detachment of Au@Cu_2O from PET fabrics during the photocatalytic process. FTIR analysis may provide further insights into the binding between Au@Cu_2O and PET associated with the formation of hydrogen bonds. Specifically, the hydrogen bonds formed at the carbonyl oxygen of PET can induce a frequency shift for the vibration of carbonyl group.[13] As Supplementary Figure S2 compares, a perceivable frequency shift of C=O stretching was observed for the functionalized PET, presumably ascribable to the intermolecular interaction between PET and Au@Cu_2O.

In this work, Au@Cu_2O with three different shell thicknesses was respectively immobilized on PET fabrics to study the influence of shell thickness on the resultant photocatalytic efficiency. Pure Cu_2O and pure Au were also introduced to PET fabrics to highlight the superior feature of Au@Cu_2O. As displayed in Figure 2(c-f), pure Cu_2O and the three Au@Cu_2O shared similar microstructural features with a rounded surface morphology. Pure Cu_2O had a particle size of 55.3 ± 6.1 nm. The three Au@Cu_2O had a particle size of 53.4 ± 4.2, 63.4 ± 5.1 and 74.4 ± 5.5 nm, respectively, corresponding to a shell thickness of 38.1 ± 2.8 (Au@Cu_2O-2), 48.1 ± 3.7 (Au@Cu_2O-3) and 59.1 ± 4.1 nm (Au@Cu_2O-4). The results of SEM-EDS analysis in Figure 2(g-i) revealed a gradual increase in Cu/Au ratio from 19.59 (Au@Cu_2O-2), 29.63 (Au@Cu_2O-3), to 44.19 (Au@Cu_2O-4), consistent with the microstructural observations.

The materials properties of Au@Cu_2O were further investigated with XRD, UV-visible absorption and PL spectroscopy. Figure 3(a) showed the XRD analytic results, suggesting the high crystallinity for Au@Cu_2O with the core composition of fcc Au and

shell composition of cubic Cu_2O both complying with the JCPDS database. Note that high crystallinity is beneficial for photocatalytic applications because it can facilitate charge carrier transfer. In Figure 3(b), the UV-visible absorption spectra of the three Au@Cu_2O were compared with those of pure Au and pure Cu_2O. The pure Au exhibited a typical surface plasmon resonance (SPR) absorption peak at 520 nm, complying well with the reported values for Au colloids [14]. Compared to pure Au, the three Au@Cu_2O displayed the SPR peak at a longer wavelength beyond 650 nm. The larger refractive index of the surrounding Cu_2O (n = 2.8–3.4 for Cu_2O) than the solvent (n = 1.33 for H_2O) [7,15] may account for the observed SPR shifting. An additional absorption shoulder around 480 nm can be identified for the three Au@Cu_2O. A similar absorption feature was also observed for pure Cu_2O, which can be attributed to the excitonic bandgap absorption [16]. Accordingly, the optical bandgap of the three Au@Cu_2O was determined to be 2.58 eV. Figure 3(c) further compared the steady-state PL spectra for pure Cu_2O and the three Au@Cu_2O. These Cu_2O-based samples exhibited a broad emission band that can be ascribed to the excitonic band-to-band emission of Cu_2O [17]. The PL emission of Cu_2O crystals may result from four possible electronic transitions.[18] The yellow series show an emission of around 2.17 eV, ascribable to the transition from the highest valence band to the lowest conduction band. The green series have an energy of around 2.28 eV, corresponding to the transition from a band below the highest valence band to the lowest conduction band. The blue series produce an emission in the range from 2.56 to 2.63 eV, which derives from the electronic transition from the highest valence band to a band above the lowest conduction band. The violet series exhibit an emission beyond 2.69 eV, which can be assigned to the transition from a band below the highest valence band to a band above the lowest conduction band. In this work, the recorded broad PL emission for

pure Cu_2O and Au@Cu_2O might be a result of the spectral overlap of multiple emissions related to the four electronic transitions. In comparison to pure Cu_2O, the three Au@Cu_2O showed a significantly depressed PL emission, reflecting the prevalence of pronounced charge separation. On the other hand, an obvious redshift of PL emission was noticed for Au@Cu_2O as the Cu_2O thickness increased. Similar phenomenon was ever reported for Cu_2O nanocrystals,[19] in which larger Cu_2O absorbed light of longer wavelength. This outcome was attributed to the optical size effect even though the crystal size of Cu_2O was relatively large. For Au@Cu_2O, the band alignment at interface can promote interfacial charge transfer to spatially separate the photoexcited electrons from the photogenerated holes.[18] The electron-hole recombination can therefore be prohibited, increasing the carrier utilization efficiency to enhance the photocatalytic activity. The Au@Cu_2O-functionalized PET fabrics were also characterized with XRD. As can be seen from Figure 3(d), diffractions peaks attributable to PET and Au@Cu_2O components can be respectively identified at the 2θ region from 15° to 28°[20] and from 30° to 80°. This result demonstrated the successful immobilization of Au@Cu_2O on PET fabrics.

The charge transfer pathway at the Au/Cu_2O interface of Au@Cu_2O can be further explored by conducting XPS analysis. By monitoring the binding energy shift on selected elements, a plausible scenario accounting for the interfacial charge transfer can be identified. The comparative results of XPS analysis were shown in Supplementary Figure 3 and Figure 4. The binding energy of Au 4f core level was first compared. Pure Au displayed doublet peaks of Au 4f at 87.9 and 84.3 eV, which was in good agreement with the reported values for Au colloids.[21,22] Comparatively, Au@Cu_2O showed a smaller binding energy of Au 4f (87.5 and 83.8 eV), suggesting an increased electron density at the Au core as a result of electron transfer from Cu_2O to Au. Similar phenomena can be

observed in other metal/semiconductor composites systems, where the reduced binding energy of metal components of metal/semiconductor composites was considered as a result of electron charging [23–27]. The considered electron transfer pathway from Cu_2O to Au can be corroborated by identifying the complementary binding energy change for the Cu_2O shell of Au@Cu_2O. As Figure 4 shows, both of the Cu 2p and O 1s of Au@Cu_2O showed a perceivably larger binding energy than pure Cu_2O did. For the Cu 2p spectra, peak deconvolution disclosed three sets of doublet peaks, which can be respectively attributed to the chemical states of Cu^+ of Cu_2O (952.3 eV for Cu $2p_{1/2}$ and 932.4 eV for Cu $2p_{3/2}$), Cu^{2+} of $Cu(OH)_2$ (954.6 eV for Cu $2p_{1/2}$ and 933.3 eV for Cu $2p_{3/2}$), and Cu^{2+} satellite (962.8 and 944.0 eV) [28]. The existence of $Cu(OH)_2$ at Cu_2O surface has been commonly observed [29], which might originate from the incomplete dehydration during the crystal growth of Cu_2O. For the O 1s spectra, the deconvoluted doublets comprised the lattice oxygen of Cu_2O (530.1 eV) and the surface oxygen of hydroxides (531.1 eV), consistent with the spectral features of Cu_2O crystal.[28] Note that the results of peak deconvolution of O 1s spectra were consistent with those reported in the literature,[30,31] showing two distinct peaks that can be respectively assigned to the lattice oxygen and surface oxygen. Based on the XPS analytical results, transportation of photoexcited electrons from Cu_2O to Au and localization of photogenerated holes at Cu_2O were considered for the present Au@Cu_2O system.

3.3.2 PEC performance

To evaluate the charge separation efficiency of the samples, photocurrent generation over a long period of PEC operation was monitored. Figure 5(a) displayed the I−t curves recorded under chopped AM 1.5 G illumination at +0.38 V vs RHE. All of the tested

electrodes showed a prompt, stable photoresponse during the alternating on/off switches of irradiation. The average current enhancement induced by light irradiation was 13.30 μA/cm^2 for Au@Cu_2O-3 and 11.96 μA/cm^2 for pure Cu_2O. This outcome demonstrated that the addition of Au enhanced charge separation efficiency for Cu_2O, thereby improving the photocurrent generation. The presence of Au core, on the other hand, may contribute to an enhanced photoactivity for Cu_2O shell by virtue of the SPR effect. It has been widely documented that the contribution of the surface plasmon resonance of Au to the enhanced photoactivity of semiconductors is limited, usually less than 1 % of activity enhancement [18,32–34]. To resolve this issue, incident photon-to-current efficiency (IPCE) measurements were further conducted on Au@Cu_2O-3 and pure Cu_2O. As Figure 5(b) reveals, the enhanced photoactivity of Au@Cu_2O-3 mostly resulted from irradiation at wavelength less than 600 nm, a region where the bandgap excitation of Cu_2O dominated. The pronounced charge separation induced by band alignment at Au/Cu_2O interface can increase the carrier utilization efficiency for Cu_2O, therefore increasing the photoactivity upon bandgap excitation. Although Au@Cu_2O-3 showed definite SPR band beyond 650 nm, the resultant photoactivity gain was less than 0.005 % as was identified from the corresponding IPCE spectra. The primary factors contributing to the overall photoactivity enhancement were therefore considered as pronounced charge separation upon bandgap excitation of Cu_2O, rather than the plasmonic effect of Au.

3.3.3 Photocatalytic properties and mechanism

By virtue of the capacity of Au@Cu_2O,[7,18] the functionalized PET fabrics were capable of conducting various photocatalytic reactions. To demonstrate the application scenario in environmental purifications, photocatalytic degradation of MO was employed

as the model reaction. Figure 6(a) compared the results of photocatalytic MO degradation over various functionalized PET fabrics. Here, PET fabrics were functionalized with five kinds of nanocrystals, including pure Au, pure Cu_2O and the three Au@Cu_2O, and were tested for performance comparison. By assuming pseudo firs-order kinetics, the rate constant of MO degradation can be computed, giving 0.36, 0.78, 3.90, 7.43, and 6.78 × 10^{-3} min^{-1} for PEC fabrics functionalized with pure Au, pure Cu_2O, Au@Cu_2O-2, Au@Cu_2O-3 and Au@Cu_2O-4, respectively. Notably, PET fabrics functionalized with pure Au and pure Cu_2O showed fairly weak photocatalytic activities. Pure Au can function as a plasmonic photocatalyst; however, its activity is intrinsically low due to the ultrafast relaxation of hot carriers.[35] Pure Cu_2O is photocatalytic active, while its photocatalytic performance was mediocre owing to the limited carrier utilization efficiency as a result of the prevalent electron-hole recombination. As compared to pure Au and pure Cu_2O, the PET fabrics functionalized with Au@Cu_2O exhibited substantially enhanced photocatalytic performance toward MO degradation. This enhancement was ascribed to the pronounced charge separation rendered by the band alignment between Au and Cu_2O. Among the three Au@Cu_2O, Au@Cu_2O-3 provided PET fabrics with the best photocatalytic performance. For Au@Cu_2O-4, the further thickened Cu_2O shell can harvest additional photons to increase the total number of photoexcited charge carriers. However, the extensive growth of Cu_2O would prohibit interfacial charge transfer to largely deteriorate carrier utilization [36]. This counteractive effect led to an otherwise decreased photocatalytic activity observed for Au@Cu_2O-4-functionalized PET. To illustrate the long-term applicability, Au@Cu_2O-3-functionalized PET fabrics were repeatedly used in photocatalytic MO degradation. As shown in Figure 6(b), after four cycles of operation, the functionalized PET fabrics can maintain 80 % of the initial

activity, highlighting the structural robustness of the supporting PET and the chemical integrity of the introduced Au@Cu_2O. XRD and SEM were further used to examine the structural stability of Au@Cu_2O-functionalized PET after the MO degradation reaction. As revealed in Figure 6(c), no appreciable change in microstructural morphology and crystallographic structure can be observed after four consecutive cycles of the MO degradation, demonstrating the commendable stability of Au@Cu_2O. The XPS spectrum of Cu 2p core level for Au@Cu_2O upon photocatalytic reaction was also examined. As shown in Supplementary Figure S4, Cu_2O and $Cu(OH)_2$ were still existent after photocatalytic operation, suggesting the high chemical integrity for Au@Cu_2O. Scavenger experiments were further conducted to identify the reactive species responsible for the photocatalytic MO degradation on Au@Cu_2O-functionalized PET. In these experiments, $AgNO_3$, EDTA, IPA, and BQ were respectively added to the photocatalytic solution in order to trap electrons, holes, ·OH and $\cdot O_2^-$ [6] produced from the functionalized PET. If the resulting photocatalytic performance was largely declined, the designated reactive species were considered as the main species participating in the degradation of MO. As evident from Figure 6(d), additions of EDTA and BQ both led to nearly inactivation for the functionalized PET. This observation manifested that holes and $\cdot O_2^-$ were mainly responsible for MO degradation over the current Au@Cu_2O-functionalized PET. On the other hand, adding IPA caused a noticeable activity decrease, while adding $AgNO_3$ did not pose any effect. This result suggested that ·OH was partly involved in MO degradation, while electrons were irrelevant. Based on the above observations, a plausible mechanism was proposed to account for the MO degradation process over the functionalized PET. Under light illumination, electrons and holes were produced from the introduced Au@Cu_2O. Owing to the band alignment at the Au/Cu_2O

interface, the photoexcited electrons were separated from the photogenerated holes. Because the separated holes were highly oxidative, they can directly degrade MO. On the other hand, the separated electrons can react with the dissolved oxygen to produce $\cdot O_2^-$. As a highly oxidative species, $\cdot O_2^-$ can readily degrade MO. Some of the produced $\cdot O_2^-$ can undergo a series of protonation processes to form $\cdot OH$, contributing to MO degradation as well.

Note that MO is one kind of azo dyes. In the textile industry, azo dyes are most commonly present, representing a major pollutant found worldwide. Using MO as a test pollutant is thus important with regard to the development of photocatalysis technology for environmental protection. The photocatalytic performance of the functionalized PET toward the degradation of methylene blue (MB), a non-azo dye, has also been examined. As displayed in Supplementary Figure S5, the functionalized PET also exhibited a noticeable activity toward the degradation of MB, demonstrating its utility and adaptability in a wide spectrum of photocatalytic applications. To illustrate the real-life applications, the functionalized PET was further employed to treat simulated textile wastewater. The simulated textile wastewater was prepared by mixing MO with the synthetic municipal sewage composed of a given concentration of peptone, meat extract, K_2HPO_4, urea, NaCl, $CaCl_2$, $MgSO_4$ and tap water [5]. As can be seen from Supplementary Figure S6, a noticeable photocatalytic activity toward the degradation of simulated textile wastewater was still observed for the functionalized PET even though it was inferior to the performance toward the degradation of the model MO. Here, the reduced photocatalytic activity may be ascribed to the interference between the multiple cations and anions ions present in the synthetic municipal sewage. Nevertheless, this demonstration highlights the applicability of the current Au@Cu_2O-funcitonalzed PET

fabrics to the real-life scenarios.

The potential leaching issue of the deposited Au@Cu_2O has also been examined by analyzing the supernatant of the photocatalytic reaction solution with SEM and EDS. Results showed that a perceivable number of nanocrystals with a trace amount of Cu element was present, indicative of the detachment of Au@Cu_2O from the functionalized PET. This outcome can also be witnessed from Figure 6(b), which revealed a 20 % loss of photocatalytic activity for the functionalized PET upon four cycles of operation. By assuming the activity loss was entirely due to the detachment of Au@Cu_2O, the detached amount can be estimated to be 1.0 mg. This detachment level was substantially lower than the median lethal dose of Cu_2O (470 mg/kg for rat by mouth) [37]; as a result, it would not pose a detrimental health effect.

3.4 Chapter Summary

In conclusion, the practical use of Au@Cu_2O-functionalized PET fabrics in photocatalytic degradation of MO, MB and simulated textile wastewater has been demonstrated. Such a competent photocatalytic capacity may stimulate the development of photocatalyst powders-functionalized fabrics for long-term recyclable usage in various photocatalytic reactions. The current work may inspire further interests in bringing functional textiles one step closer to practical applications in environmental purifications and energy conversion.

3.5 References

[3-1] J. Kimling, M. Maier, B. Okenve, V. Kotaidis, H. Ballot, A. Plech, *J. Phys. Chem. B* **2006**, *110*, 15700.

[3-2] Y.-H. Chiu, S. A. Lindley, C.-W. Tsao, M.-Y. Kuo, J. K. Cooper, Y.-J. Hsu, J. Z. Zhang, *J. Phys. Chem. C* **2020**, *124*, 11333.

[3-3] M. Anas, D. S. Han, K. Mahmoud, H. Park, A. Abdel-Wahab, *Mater. Sci. Semicond. Process.* **2016**, *41*, 209.

[3-4] Y. S. Sohn, Y. R. Smith, M. Misra, V. (Ravi) Subramanian, *Appl. Catal. B Environ.* **2008**, *84*, 372.

[3-5] B. Chen, F. Long, S. Chen, Y. Cao, X. Pan, *Chem. Eng. J.* **2020**, *385*, 123926.

[3-6] Y.-H. Chiu, Tso-Fu Chang, C.-Y. Chen, M. Sone, Y.-J. Hsu, *Catalysts* **2019**, *9*, 430.

[3-7] M.-Y. Kuo, C.-F. Hsiao, Y.-H. Chiu, T.-H. Lai, M.-J. Fang, J.-Y. Wu, J.-W. Chen, C.-L. Wu, K.-H. Wei, H.-C. Lin, Y.-J. Hsu, *Appl. Catal. B Environ.* **2019**, *242*, 499.

[3-8] Y.-H. Chiu, Y.-J. Hsu, *Nano Energy* **2017**, *31*, 286.

[3-9] D. A. Prado-Chay, M. A. Cortés-Jácome, C. Angeles-Chávez, R. Oviedo-Roa, J. M. Martínez-Magadán, C. Zuriaga-Monroy, I. J. Hernández-Hernández, P. R. Mayoral, D. R. Gómora-Herrera, J. A. Toledo-Antonio, *Top. Catal.* **2020**, *63*, 586.

[3-10] S. Arayachukiat, C. Kongtes, A. Barthel, S. V. C. Vummaleti, A. Poater, S. Wannakao, L. Cavallo, V. D'Elia, *ACS Sustain. Chem. Eng.* **2017**, *5*, 6392.

[3-11] J. Liu, Q. Zhang, B. Zhang, M. Yu, *Polymers* **2020**, *12*, 3052.

[3-12] C. L. Loch, D. Ahn, C. Chen, J. Wang, Z. Chen, *Langmuir* **2004**, *20*, 5467.

[3-13] S. Zhou, X. Zheng, X. Yu, J. Wang, J. Weng, X. Li, B. Feng, M. Yin, *Chem. Mater.* **2007**, *19*, 247.

[3-14] J. Wang, D. Song, L. Wang, H. Zhang, H. Zhang, Y. Sun, *Sens. Actuators B Chem.* **2011**, *157*, 547.

[3-15] K.-H. Yang, S.-C. Hsu, M. H. Huang, *Chem. Mater.* **2016**, *28*, 5140.

[3-16] B. Li, Y. Li, Y. Zhao, L. Sun, *J. Phys. Chem. Solids* **2013**, *74*, 1842.

[3-17] M. Abdelfatah, A. Basuni, H. Y. Salah, M. Bakry, N. Darwesh, W. Ismail, A. El-Shaer, *Opt. Mater.* **2022**, *130*, 112583.

[3-18] T.-H. Lai, C.-W. Tsao, M.-J. Fang, J.-Y. Wu, Y.-P. Chang, Y.-H. Chiu, P.-Y. Hsieh, M.-Y. Kuo, K.-D. Chang, Y.-J. Hsu, *ACS Appl. Mater. Interfaces* **2022**, *14*, 40771.

[3-19] J.-Y. Huang, M. Madasu, M. H. Huang, *J. Phys. Chem. C* **2018**, *122*, 13027.

[3-20] W. Yu, X. Zhang, X. Gao, H. Liu, X. Zhang, *J. Mater. Sci.* **2020**, *55*, 8940.

[3-21] J.-P. Sylvestre, S. Poulin, A. V. Kabashin, E. Sacher, M. Meunier, J. H. T. Luong, *J. Phys. Chem. B* **2004**, *108*, 16864.

[3-22] J.-Y. Wu, T.-H. Lai, M.-J. Fang, J.-Y. Chen, M.-Y. Kuo, Y.-H. Chiu, P.-Y. Hsieh, C.-W. Tsao, H.-E. Chang, Y.-P. Chang, C.-Y. Wang, C.-Y. Chen, M. Sone, W.-W. Wu, T.-F. M. Chang, Y.-J. Hsu, *ACS Appl. Nano Mater.* **2022**, acsanm.2c01529.

[3-23] T.-T. Yang, W.-T. Chen, Y.-J. Hsu, K.-H. Wei, T.-Y. Lin, T.-W. Lin, *J. Phys. Chem. C* **2010**, *114*, 11414.

[3-24] H. Wang, D. Peng, X. Hu, X. Ma, W. Ye, W. Zhang, Y. Chang, S. Dong, *Mater. Res. Bull.* **2018**, *108*, 176.

[3-25] X. Jin, F. Chen, D. Jia, Y. Cao, H. Duan, M. Long, *RSC Adv.* **2020**, *10*, 4455.

[3-26] L. Sinatra, A. P. LaGrow, W. Peng, A. R. Kirmani, A. Amassian, H. Idriss, O. M. Bakr, *J. Catal.* **2015**, *322*, 109.

[3-27] Q. Wei, Y. Wang, H. Qin, J. Wu, Y. Lu, H. Chi, F. Yang, B. Zhou, H. Yu, J. Liu, *Appl. Catal. B Environ.* **2018**, *227*, 132.

[3-28] I. Platzman, R. Brener, H. Haick, R. Tannenbaum, *J. Phys. Chem. C* **2008**, *112*, 1101.

[3-29] S. Gong, X. Wu, J. Zhang, N. Han, Y. Chen, *CrystEngComm* **2018**, *20*, 3096.

[3-30] W. Zhang, X. Yang, Q. Zhu, K. Wang, J. Lu, M. Chen, Z. Yang, *Ind. Eng. Chem. Res.* **2014**, *53*, 16316.

[3-31] X. Deng, Q. Zhang, E. Zhou, C. Ji, J. Huang, M. Shao, M. Ding, X. Xu, *J. Alloys Compd.* **2015**, *649*, 1124.

[3-32] Y.-C. Pu, G. Wang, K.-D. Chang, Y. Ling, Y.-K. Lin, B. C. Fitzmorris, C.-M. Liu, X. Lu, Y. Tong, J. Z. Zhang, Y.-J. Hsu, Y. Li, *Nano Lett.* **2013**, *13*, 3817.

[3-33] Y.-H. Chiu, S. B. Naghadeh, S. A. Lindley, T.-H. Lai, M.-Y. Kuo, K.-D. Chang, J. Z. Zhang, Y.-J. Hsu, *Nano Energy* **2019**, *62*, 289.

[3-34] Y.-H. Chiu, K.-D. Chang, Y.-J. Hsu, *J. Mater. Chem. A* **2018**, *6*, 4286.

[3-35] A. Furube, S. Hashimoto, *NPG Asia Mater.* **2017**, *9*, e454.

[3-36] W. Xu, J. Jia, T. Wang, C. Li, B. He, J. Zong, Y. Wang, H. J. Fan, H. Xu, Y. Feng, H. Chen, *Angew. Chem. Int. Ed.* **2020**, *59*, 22246.

[3-37] M. L. Monaghan, M. L. Doherty, J. D. Collins, J. F. Kazda, P. J. Quinn, *Vet. Microbiol.* **1994**, *40*, 111.

3.6 Figures

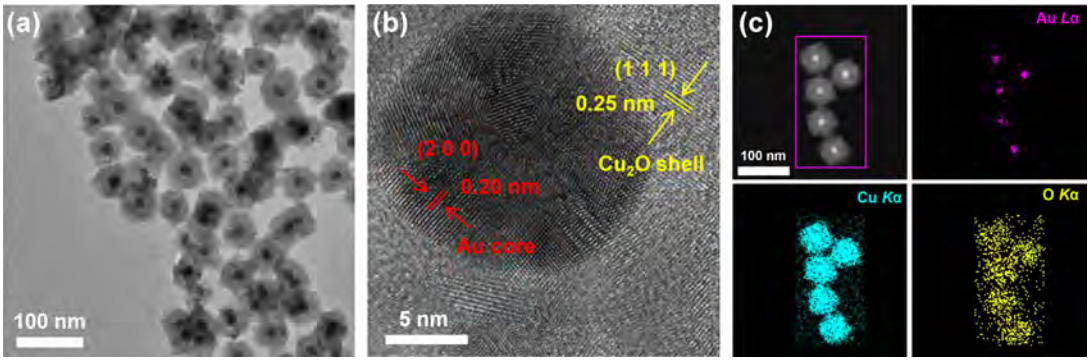

Figure 3-1. (a) Typical TEM image, (b) high-resolution TEM image, (c) EDS mapping analysis for Au@Cu_2O.

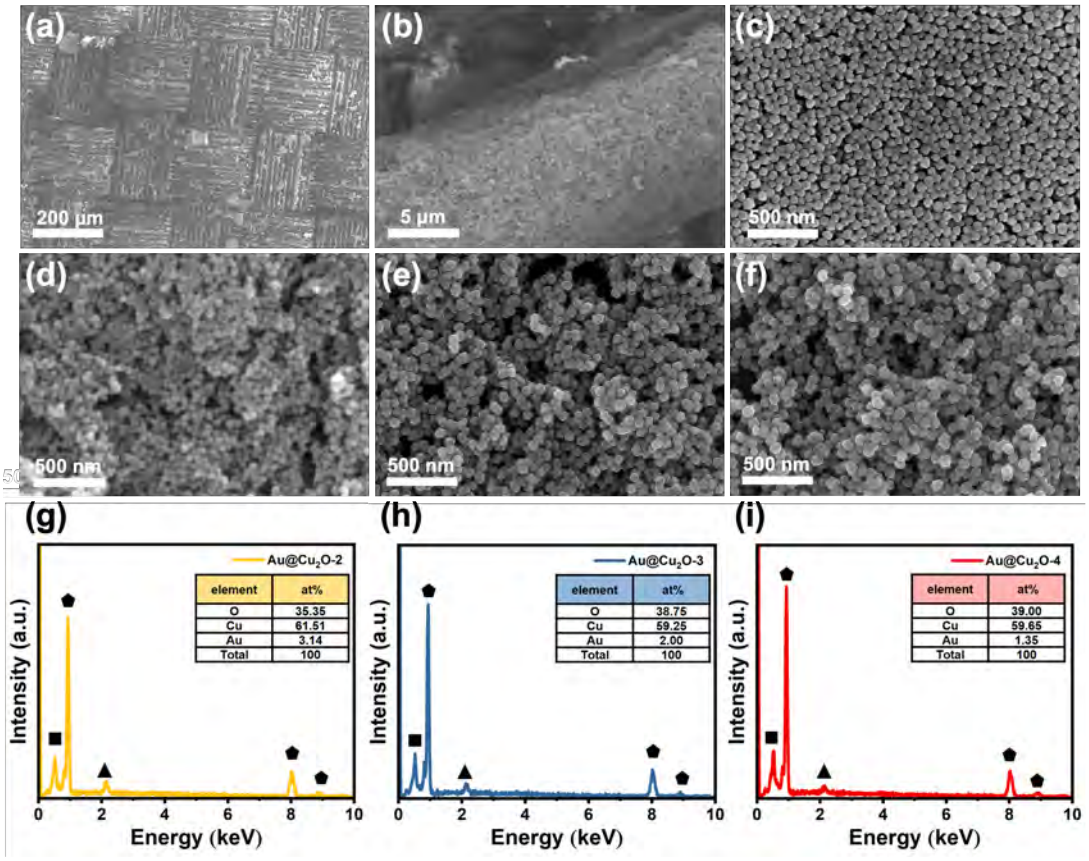

Figure 3-2. SEM images for (a-b) Au@Cu_2O-functionalzied PET fabrics, (c) pure Cu_2O, (d) Au@Cu_2O-2, (e) Au@Cu_2O-3, and (f) Au@Cu_2O-4. (g-i) Corresponding EDS spectra (■: O, ⬟: Cu, ▲: Au).

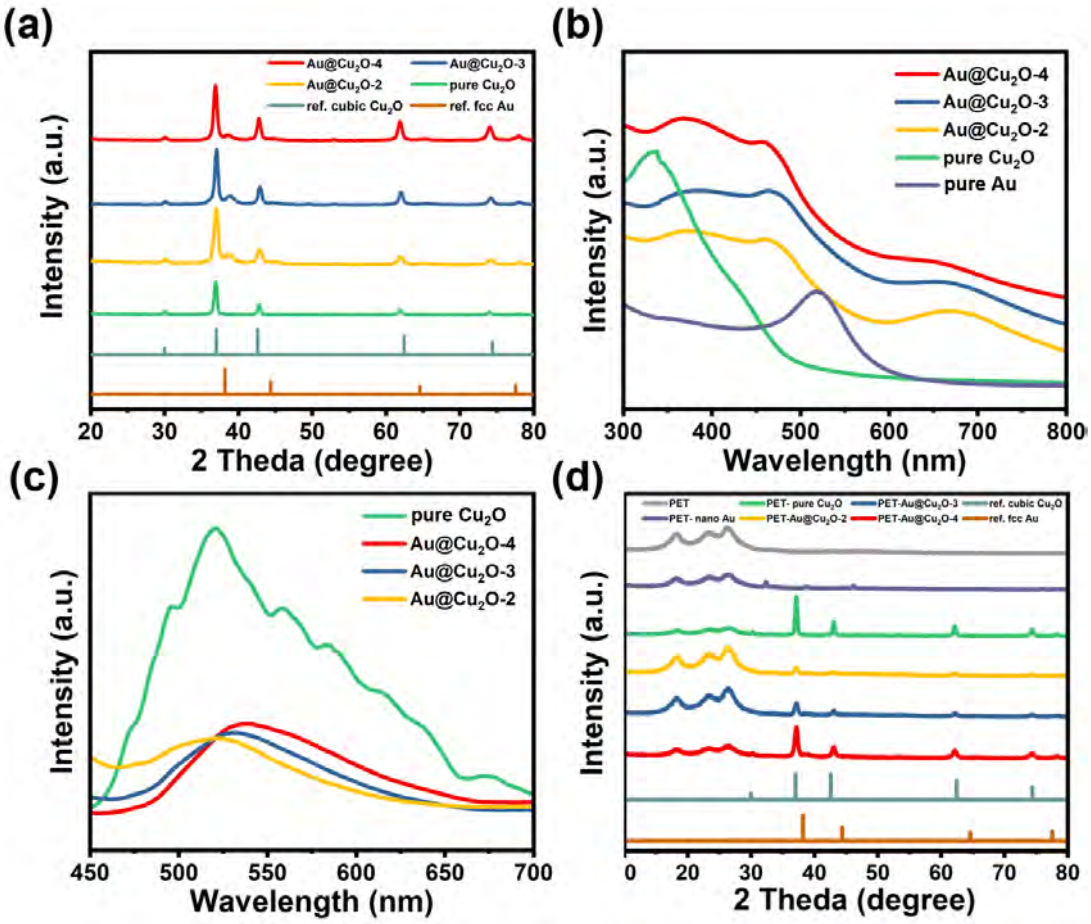

Figure 3-3. (a) XRD patterns, (b) UV-visible absorption spectra, (c) steady-state PL spectra for the three Au@Cu2O, pure Au and pure Cu_2O. (d) XRD patterns for the functionalized PET fabrics. In (a) and (d), the standard patterns of fcc Au (JCPDS #04-0784) and cubic Cu_2O (JCPDS #34-1354) were also included.

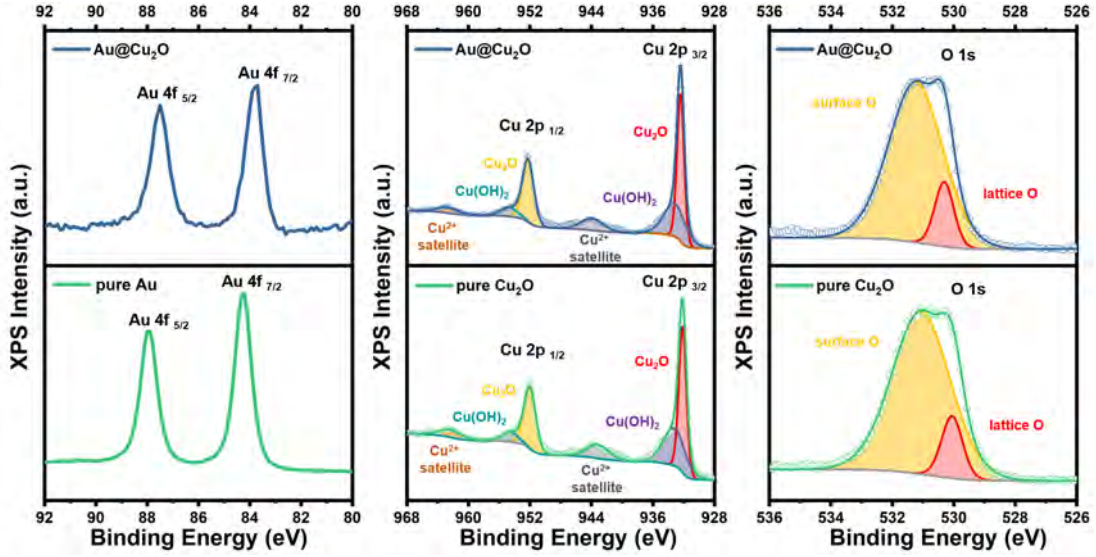

Figure 3-4. XPS spectra of Au 4f, Cu 2p and O 1s core levels for Au@Cu_2O, pure Au, and pure Cu_2O.

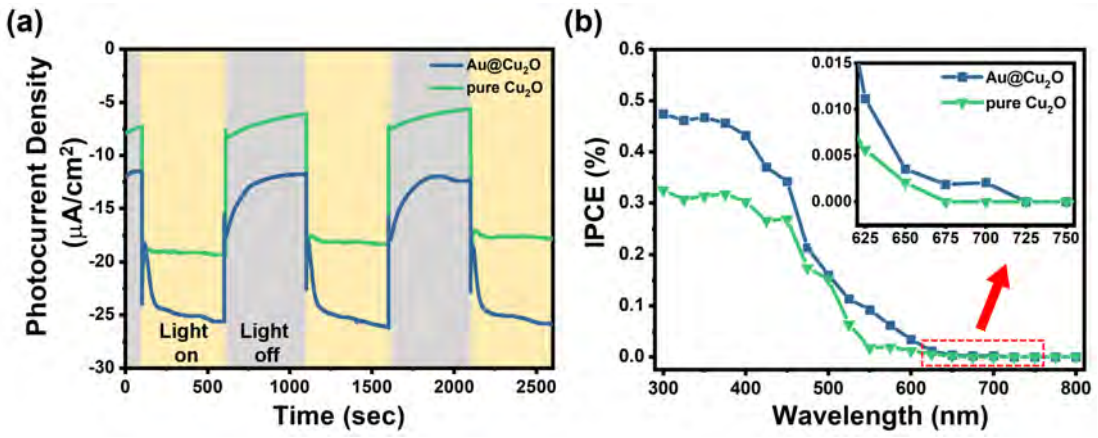

Figure 3-5. (a) I–t curves recorded on Au@Cu_2O-3 and pure Cu_2O electrodes under darkness and AM 1.5G illumination. (b) IPCE spectra recorded on Au@Cu_2O and pure Cu_2O. Inset showed the enlarged spectra at wavelength region from 625 to 750 nm.

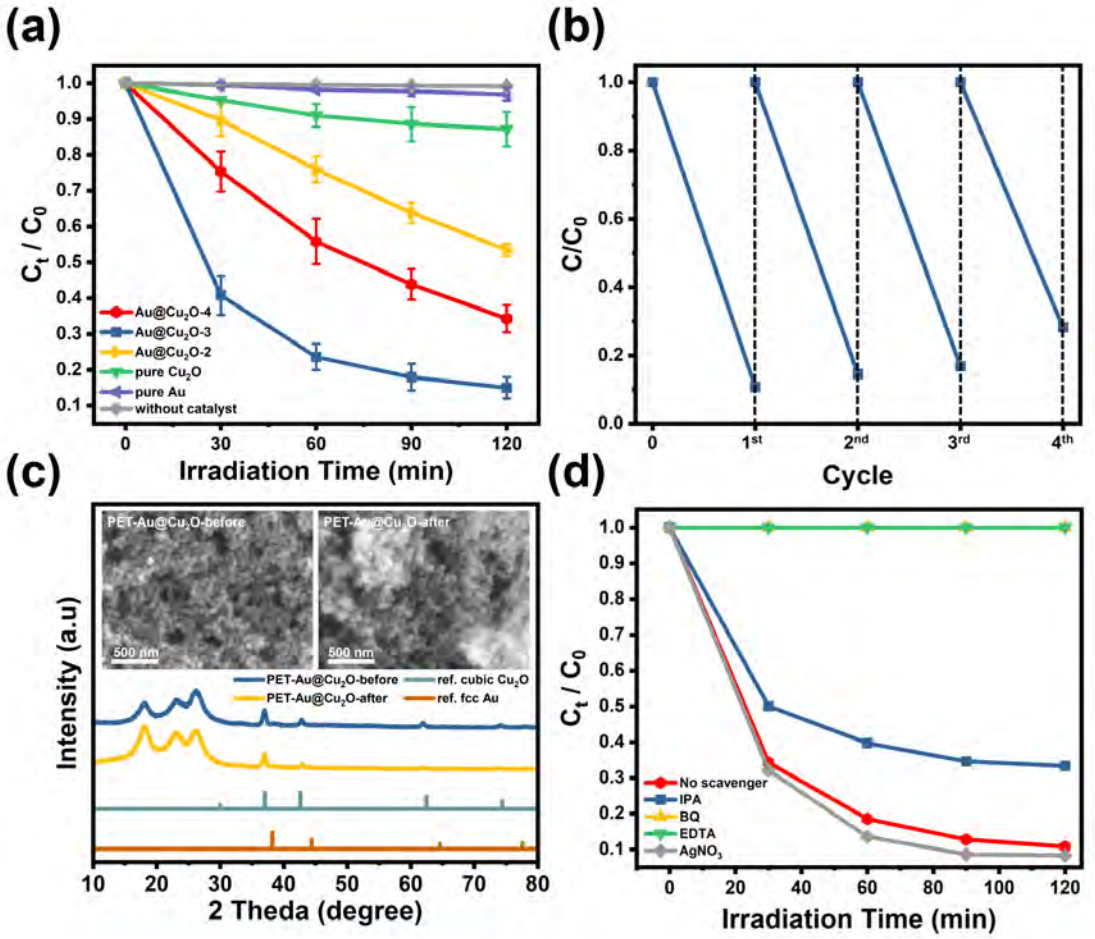

Figure 3-6. (a) Comparative results of photocatalytic MO degradation over various functionalized PET fabrics. (b) Recycling tests of photocatalytic MO degradation on Au@Cu_2O-3-functionalized PET. (c) SEM images and XRD patterns of Au@Cu_2O-functionalized PET before and after 4 cycles of MO degradation. (d) Results of scavenger experiments on Au@Cu_2O-3-functionalized PET.

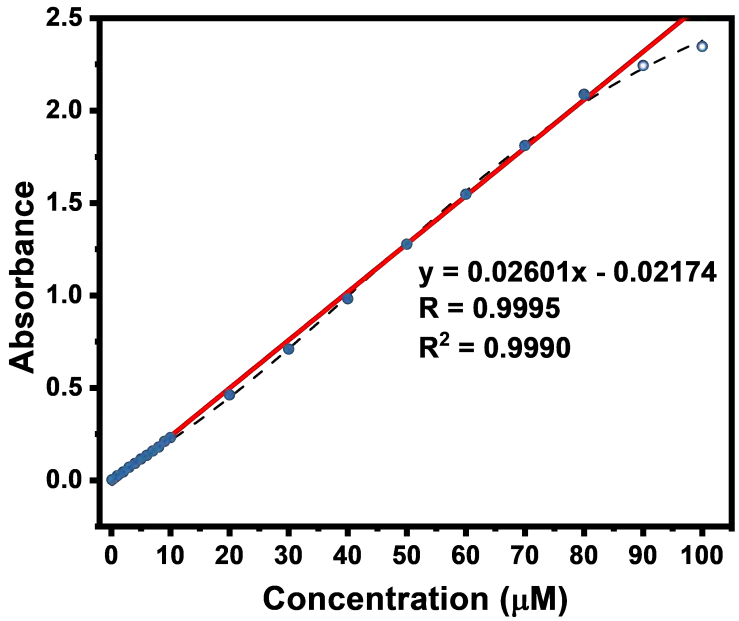

Figure 3-S1. Calibration curve of MO solutions. The solid line represented the linear regression result in the linear region. The open circles were data beyond the linearity.

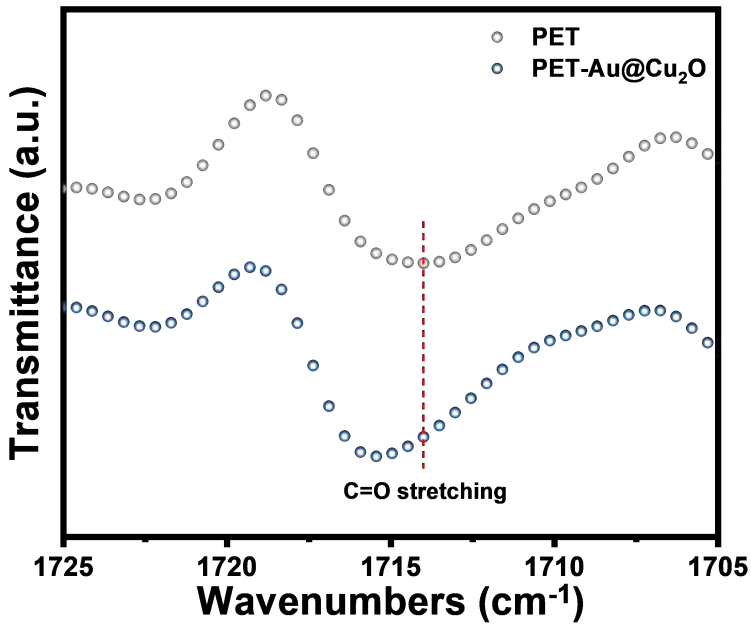

Figure 3-S2. FTIR spectra of pristine PET and Au@Cu_2O-functionalized PET.

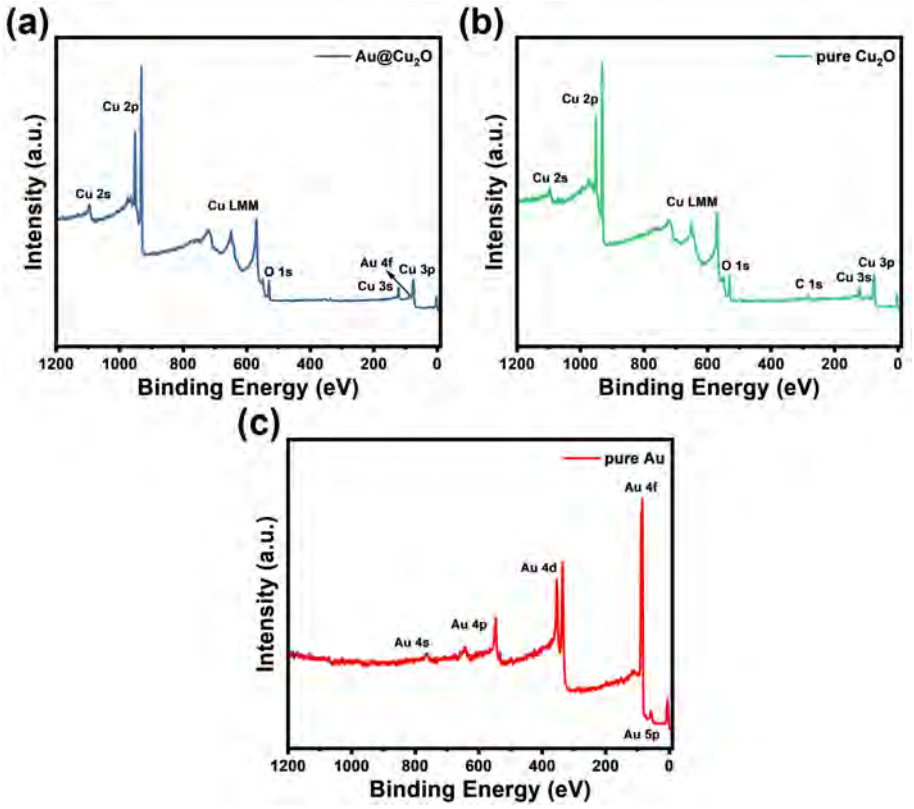

Figure 3-S3. XPS survey spectra for (a) Au@Cu_2O, (b) pure Cu_2O, and (c) pure Au.

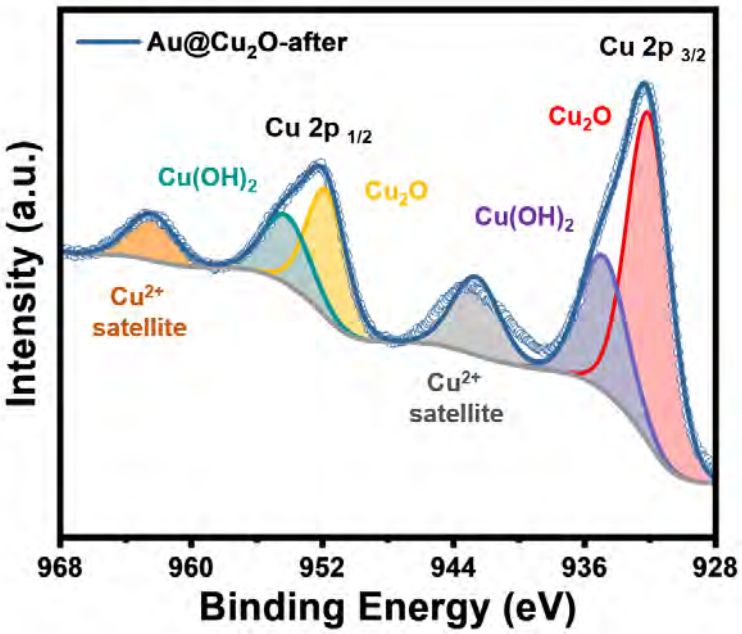

Figure 3-S4. XPS spectrum of Cu 2p core level for the repeated used Au@Cu_2O.

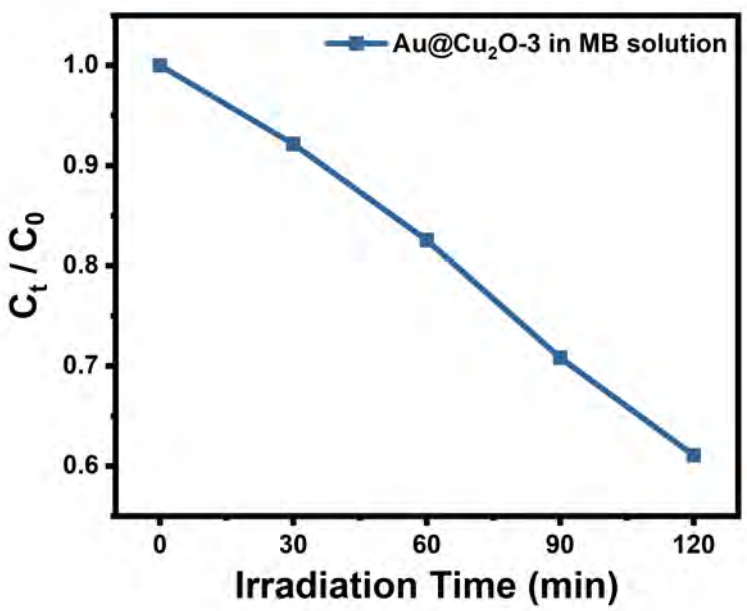

Figure 3-S5. Result of photocatalytic MB degradation over Au@Cu_2O-3 functionalized PET.

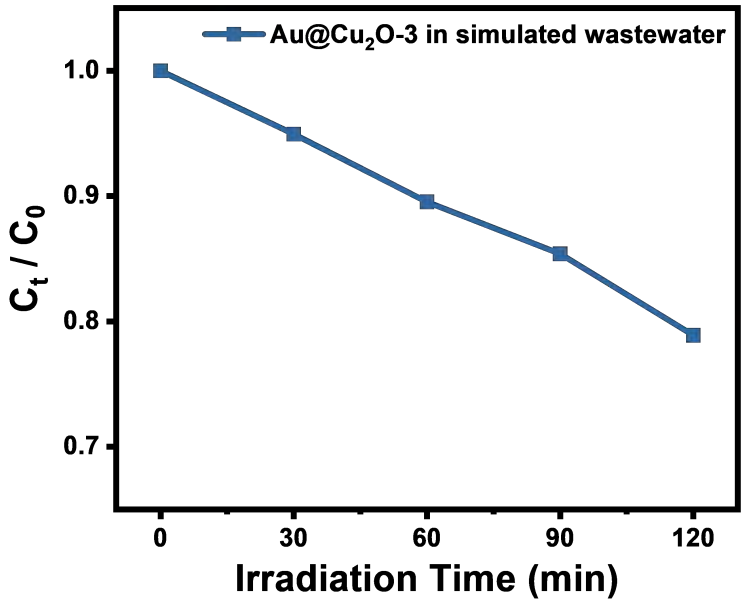

Figure 3-S6. Results of photocatalytic degradation of simulated textile wastewater over Au@Cu_2O-3-functionalized PET.

4.7 Tables

Table 4-1. Fracture strength of the Pt/PET.

Pt deposition time (min)	Pt thickness (μm)	Fracture stress (MPa)
30	0.20 ± 0.019	33.9 ± 2.84
45	0.32 ± 0.024	52.1 ± 3.42
60	0.41 ± 0.006	65.7 ± 8.96

CHAPTER 4

Material Design and Fabrication of series of yolk-shell Nanostructures

4.1 Introduction

In 2004, hollow nanocrystals of cobalt chalcogenides were prepared according to the nanoscale Kirkendall effect.[1] Subsequently, yolk-shell nanocrystals comprising a mobile core particle surrounded by a hollow, permeable shell have emerged as a subject of great interest. Compared to the core-shell nanocrystal counterpart, in which a stationary core is coated with a solid, dense shell, yolk-shell nanocrystals have many superior structural features, which can be exploited in technological applications. For instance, the confined space within the hollow shell can function as a robust nanoreactor to accelerate mass transfer dynamics. In addition, the mobile core can stir a reaction solution, creating a homogeneous, internal reaction environment.[2] The inner surface as well as the outer surface of the shell can both provide active sites for reacting species, which can facilitate reaction kinetics; furthermore, the inner surface can behave like a reflecting surface for incident light to allow for multiple reflections, which may enhance photon harvesting efficiency.[3] With such unique properties, yolk-shell nanocrystals have demonstrated remarkable potential for biomedical, catalytic, and energy conversion applications, such

as drug delivery,[4] photothermal therapy,[5] heterogeneous catalysis,[6] photovoltaic devices,[7] and hydrogen production.[8]

Several synthetic strategies have been proposed and realized in creating hollow nanocrystals. The core concept includes the use of the Kirkendall effect,[9] galvanic exchange,[10] chemical etching,[11] Ostwald ripening,[12] and thermal treatment.[13] Among them, ion exchange on the basis of Kirkendall effect has shown a preponderant capacity of creating hollow nanocrystals possessing tailored compositions.[14,15] A typical procedure involves the use of Cu_2O nanocrystals as a structural template, followed by sulfidation treatment with the addition of Na_2S. Because of the higher solubility product of Cu_2O than that of Cu_7S_4, Cu_7S_4 is formed at the expense of Cu_2O. During the sulfidation process, the slower inward diffusion of the foreign ions (S^{2-}) compared to the outward diffusion of the parent ions (Cu^+ or O^{2-}) causes formation of Kirkendall voids, thereby generating hollow spaces inside frameworks of Cu_7S_4.[16–18] A further kinetically controlled cation exchange reaction can be stimulated by adding specific metal ions to convert Cu_7S_4 into corresponding metal sulfides while maintaining the morphology of the starting Cu_2O.[19–21]

Metal-semiconductor heterostructures, in particular those comprising Au as the metal component, have been the limelight of photocatalyst engineering because of the fascinating properties induced by Au. The attributes include pronounced charge separation,[22] enriched active sites,[23] as well as peculiar plasmonic effect,[24] which can cooperate to enhance the overall photocatalytic efficiency. In this study, we reported a sequential ion exchange process to prepare for metal-semiconductor yolk-shell nanocrystals comprised of Au yolk and various semiconductor shells. The synthetic procedures involved delicate sulfidation on an Au@Cu_2O core-shell nanocrystal template,

followed by a kinetically controlled cation exchange reaction that enabled the conversion of shell composition into various metal sulfides. Four representative yolk-shell nanostructure samples, including Au@Cu_7S_4, Au@CdS, Au@ZnS and Au@Ni_3S_4, were synthesized for investigation. X-ray photoelectron spectroscopy (XPS) and photoluminescence (PL) spectroscopy were used to explore the electronic interactions and charge transfer dynamics between the yolk and shell components. The findings from the present study can help deploying yolk-shell nanocrystals for various photocatalysis applications, including environmental purification, hydrogen production and carbon dioxide reduction.

4.2 Experimental

4.2.1 Chemicals

All chemicals and reagents were of analytical grade and used as received without further purification.

4.2.2 Preparation of Au@Cu_2O core-shell nanocrystals

First, a typical citrate reduction approach was employed to obtain Au particles having an average diameter around 15 nm.[25] To deposit Cu_2O, a given amount of NaOH solution (1.5 mL, 1.0 M) was added to deionized water (32.5 mL), followed by a sequential injection of $CuSO_4$ solution (4.0 mL 0.01 M), Au colloid (3.0 mL, 0.25 mM), and *L*-ascorbic acid (0.5 mL, 0.1 M). The mixed solution was stirred at 35 °C for 10 min, and the product (Au@Cu_2O) was purified with deionized water and collected with centrifugation.

4.2.3 Preparation of Au@Cu_7S_4 yolk-shell nanocrystals

To prepare for Au@Cu_7S_4, an Au@Cu_2O methanol colloid (0.4 mmol, 10.0 mL) was mixed with an Na_2S solution (0.2 M, 800 μL) under vigorous stirring for 10 min. The product (Au@Cu_7S_4) was washed with an HCl solution (pH = 1.0) and collected with centrifugation.

4.2.4 Preparation of Au@CdS, Au@ZnS, and Au@Ni_3S_4 yolk-shell nanocrystals

To prepare for Au@CdS, an Au@Cu_7S_4 methanol colloid (0.4 mmol, 10.0 mL) was added to a 50 mL flask, followed by an addition of $Cd(NO_3)_2 \cdot 4H_2O$ (4 mmol in 1.5 mL methanol) and tributyl phosphate (TBP) (8 mmol in 1.0 mL toluene). The mixed solution was heated at 50 °C under stirring for 12 hr. The product (Au@CdS) was collected with centrifugation and then dispersed in methanol for later analysis. By replacing $Cd(NO_3)_2 \cdot 4H_2O$ with $Zn(NO_3)_2 \cdot 6H_2O$ and $Ni(NO_3)_2 \cdot 6H_2O$, Au@ZnS and Au@Ni_3S_4 can be obtained, respectively. For comparison, pure Cu_7S_4, pure CdS, pure ZnS, and pure Ni_3S_4 nanocrystals were also prepared by using the identical ion exchange procedure in the absence of Au colloids.

4.2.5 Characterizations

The microstructural features of the samples were characterized with a field-emission scanning electron microscope (SEM, JEOL, JSM-7800F) and a high-resolution transmission electron microscope (HRTEM, JEOL, JEM-ARM200FTH) operated at 200 kV. The crystallographic structure and chemical compositions were studied with X-ray diffraction (XRD, Bruker, D2 phaser), selected-area electron diffraction (SAED), and an energy dispersive X-ray spectrometer (EDS) installed on the SEM (JSM-7800F) and

TEM (JEM-ARM200FTH). The chemical states of the samples were analysed with XPS (VG Scientific, Microlab 350) using Al Kα radiation. The recorded binding energies were calibrated to C 1s peak at 284.8 eV. UV-visible diffuse reflectance spectra (DRS) were obtained from a spectrometer (Hitachi, U-3900H) equipped with an integrating sphere. Steady-state photoluminescence (PL) spectra were collected in a commercial spectroscope (Horiba, FluoroMax-3) using 320 nm as excitation wavelength. Time-resolved PL spectra were obtained in a customized single-photon counting setup, which contains a sub-nanosecond pulsed diode laser (λ_{ex} = 320 nm, PicoQuant, PLD 320) and provides an instrument response function down to 25 ps FWHM. The recorded data were fitted with a biexponential kinetics equation to generate two lifetime components (τ_1, τ_2) and the corresponding amplitude contributions (A_1, A_2) along with the goodness of the fitting result (χ^2). The intensity-average lifetime ($<\tau>$) was then computed for overall comparison.

4.3 Results and Discussion

4.3.1 Morphology and crystallographic structure

Figure 1(a) depicts the synthetic procedure for producing Au@Cu_7S_4, Au@CdS, Au@ZnS, and Au@Ni_3S_4 yolk-shell nanocrystals. The Au particles obtained from the citrate reduction had a uniform size distribution of 15.3 ± 1.4 nm. During the deposition of Cu_2O, the carboxyl groups on the surface of citrate-protected Au can coordinate with Cu^{2+} ions.[17] As Cu^{2+} ions were bound to the surface of Au, each Au particle can be completely deposited with Cu_2O to produce Au@Cu_2O core-shell nanocrystals. As Figure S1 (supporting information) shows, the TEM image, lattice-resolved HRTEM image, SAED pattern and TEM-EDS mapping data manifested the core-shell structural feature

and chemical compositions for the as-prepared Au@Cu_2O. In the second step, as Na_2S was added to the Au@Cu_2O template, the Cu_2O shell was transformed into Cu_7S_4 because of the lower solubility product of Cu_7S_4 ($K_{sp} = 1 \times 10^{-48}$) than the value of Cu_2O ($K_{sp} = 2 \times 10^{-15}$).[26,27] In addition to the change in shell composition, Kirkendall voids were also generated during the anion exchange process because the outward diffusion of the parent ions (Cu^+ or O^{2-}) was more rapid than the inward diffusion of the foreign ions (S^{2-}).[18,28] This anion exchange induced Kirkendall effect has been extensively utilized to prepare for Cu_7S_4 hollow structures with tailored morphologies. Debates on which diffusion couple (Cu^+/S^{2-} or O^{2-}/S^{2-}) contributes to the generation of structural voids as a result of the diffusivity difference have however existed. According to the empirical data,[29,30] the diffusivity of Cu in O, O in Cu and S in Cu at 50 °C can be estimated to be 6.33×10^{-12}, 8.90×10^{-17} and 2.06×10^{-34} m^2/s, respectively. Because the crystal ionic radius of Cu^+ (91 pm) is much smaller than O^{2-} (126 pm),[31] the diffusion of Cu^+ should be dominant within the Cu_2O framework. The sufficiently faster Cu^+ outward diffusion than the S^{2-} inward diffusion can therefore exert a driving force of generating Kirkendal voids during the transformation from Cu_2O to Cu_7S_4. Consequently, Au@Cu_7S_4 nanocrystals were formed comprising the movable Au cores surrounded by the permeable Cu_7S_4 shell. As estimated from Figure 1(b), the shell thickness and void size of Au@Cu_7S_4 were 13.3 ± 2.2 nm and 63.2 ± 5.8 nm, respectively. In the next step, cation exchange was conducted to convert Cu_7S_4 into CdS, ZnS, and Ni_3S_4 while maintaining the morphology of the parent Au@Cu_7S_4. Figure 1(c-e) displays the morphology of the resulting Au@CdS, Au@ZnS and Au@Ni_3S_4. The respective shell thickness and void size were 11.0 ± 2.1 nm and 62.6 ± 4.8 nm for Au@CdS, 10.9 ± 1.6 nm and 62.1 ± 4.7 nm for Au@ZnS, and 10.2 ± 1.5 nm and 50.0 ± 3.1 nm for Au@Ni_3S_4. Note that the conversion of Cu_7S_4 to

CdS, ZnS, and Ni_3S_4 in the cation exchange reaction was thermodynamically unfavorable because the solubility product of Cu_7S_4 ($K_{sp} = 1 \times 10^{-48}$) was lower than that of the three sulphides ($K_{sp} = 8 \times 10^{-27}$, 3×10^{-25}, 1×10^{-21}, for CdS, ZnS, Ni_3S_4, respectively).[32] By adding TBP with phosphorus as the complexation substrate[33] and employing excess amounts of Cd^{2+}, Zn^{2+} and Ni^{2+} (10 times the stoichiometry of the initial Cu_7S_4), the kinetics of the cation exchange reaction were largely accelerated to achieve successful transformation of Cu_7S_4. During this phosphine induced cation exchange process, the Cu^+ ions of Cu_7S_4 were complexed with TBP to enable their extraction from the framework.[32] Meanwhile, the solvated foreign metal ions[34,35] can diffuse into the Cu_7S_4 matrix and occupy the vacant positions in the framework. As a result of the replacement of Cu^+ by the incoming metal ions, Cu_7S_4 can be converted into the corresponding metal sulfides. For the conversion of Cu_7S_4 into the three sulfides, the Cu species can be completely removed provided that an excessive supply of the foreign cations and TBP is employed along with a sufficient reaction time. As displayed in Figure S2 (supporting information), the SEM-EDS spectra revealed that no appreciable Cu element can be detected on the resultant Au@CdS, Au@ZnS and Au@Ni_3S_4.

For comparison, nanocrystals of the four pure sulfides were also prepared. Figure 2 shows that the four pure sulfide nanocrystals also possessed hollow structures resembling those of the corresponding yolk-shell nanocrystals. The respective shell thicknesses and void sizes were 12.3 ± 2.2 nm and 62.2 ± 7.4 nm for pure Cu_7S_4, 9.4 ± 2.5 nm and 60.4 ± 6.7 nm for pure CdS, 10.5 ± 2.5 nm and 59.7 ± 6.0 nm for pure ZnS, and 10.9 ± 1.9 nm and 65.0 ± 5.6 nm for pure Ni_3S_4. In Figure 3, the XRD patterns verified the compositions of fcc Au, monoclinic Cu_7S_4, wurtzite CdS, wurtzite ZnS, and polydymite Ni_3S_4 for the four yolk-shell nanocrystals and their pure counterparts.

To gain more information on the crystallographic structure of the samples, we performed HRTEM, SAED and TEM-EDS mapping analyses. Figure 4 (a-c) shows the analytical result for Au@Cu_7S_4. The recorded d-spacings of 0.19 and 0.24 nm can be appointed as the (8 8 6) and (111) planes of monoclinic Cu_7S_4 and fcc Au, respectively. The SAED pattern revealed the polycrystalline nature of the components. From the reciprocal vector length and angle, the crystallographic structure of monoclinic Cu_7S_4 and fcc Au can be confirmed. The EDS mapping data, on the other hand, revealed the uniform distribution of the constituent Cu and S elements covering the nanocrystal surface. The Cu/S molar ratio was determined to be 1.88, approximately the ideal Cu/S ratio of Cu_7S_4. In contrast, Au existed solely at the lateral surface of individual nanocrystals, complying with the yolk-shell structural feature that each of the Au particles was surrounded by a Cu_7S_4 shell. Importantly, the Au yolk particles were found to randomly situate at the interior of the Cu_7S_4 shell. Similar observations were obtained from the analytical data regarding Au@CdS, Au@ZnS, and Au@Ni_3S_4, as shown in Figure 4(d-f), Figure 4(g-i) and Figure 4(j-l), respectively. This finding indicated that Au particles were mobile inside the hollow space of yolk-shell nanocrystals, which is significant for catalytic applications. To corroborate this argument, real-time monitoring on the movement of Au yolk of Au@Cu_7S_4 nanocrystals was conducted by TEM. As can be seen from the recorded video (video S1, supporting information), under electron beam irradiation, the movement of the Au yolk inside the Au@Cu_7S_4 shell was random yet vivid. It should be noted that the technique of using electron beam of TEM to move nanoparticle has been well developed.[36] This nanoparticle manipulation is realized based on the momentum transfer from the electrons to the nanoparticles. Because the exerted force due to momentum transfer is small, the interaction between electron beam and nanoparticles is limited,

which may explain why only a few Au yolks in the sampled $Au@Cu_7S_4$ nanocrystals were mobile under TEM observation. Nevertheless, the finding from real-time TEM monitoring validated the argument that Au particles were mobile inside the hollow space of yolk-shell nanocrystals. Ideally, one single yolk-shell nanocrystal would contain one single Au yolk. In practice, multiple Au yolks can however be encapsulated in a single yolk-shell nanocrystal due to the inhomogeneity of Cu_2O deposition in the synthesis of the starting $Au@Cu_2O$. From the statistical analysis of TEM images, the average number of Au core/yolk encapsulated in the shell was estimated to be 1.24, 1.25, 1.25, 1.29 and 1.32 for $Au@Cu_2O$, $Au@Cu_7S_4$, Au@CdS, Au@ZnS, and $Au@Ni_3S_4$, respectively. For simplicity and esthetics, the sketched core-shell and yolk-shell nanocrystals in Figure 1(a) and TOC graphics contained exactly one single Au core/yolk. Figure 5 further presents the crystallographic structure of the four pure sulfide nanocrystals. These results showed that the pure sulfides and the corresponding yolk-shell nanocrystals shared identical crystallographic structures.

4.3.2 Chemical states and electronic interactions

Note that the studied yolk-shell nanocrystals comprised metal yolk (Au) and semiconductor shells (Cu_7S_4, CdS, ZnS, and Ni_3S_4), representing a typical metal-semiconductor heterostructure system.[22] The electronic interactions between the metal yolk and semiconductor shell may induce charge carrier separation under light illumination, which can be further exploited for photocatalysis applications. To investigate the electronic interactions between the yolk and shell components, the samples were further characterized with XPS spectroscopy. Figure 6(a) shows a comparison of the XPS spectra among $Au@Cu_7S_4$, Au colloids and pure Cu_7S_4. For Au 4f spectra, both

Au@Cu_7S_4 and Au colloids exhibited doublet peaks at 87.9 and 84.3 eV associated with the Au $4f_{5/2}$ and Au $4f_{7/2}$ components of metallic Au.[37] For the Cu 2p spectra, the observed doublet peaks at 951.6 eV and 931.7 eV appeared to originate from the Cu $2p_{1/2}$ and Cu $2p_{3/2}$ components of Cu_7S_4.[17] For the S 2p spectra, peak deconvolution revealed the existence of two sets of double peaks. For pure Cu_7S_4, the main double peaks at 162.5 (S $2p_{1/2}$) and 161.4 eV (S $2p_{3/2}$) were designated for sulfide (S^{2-}), while the minor doublets at 163.6 (S $2p_{1/2}$) and 162.5 eV (S $2p_{3/2}$) were assigned to disulfide (S_2^{2-}).[38] The coexistence of sulfide and disulfide was characteristic of nonstoichiometric $Cu_{2-x}S$ nanostructures.[38] For Au@Cu_7S_4, the two sets of double peaks of S 2p were slightly divergent from those of pure Cu_7S_4, showing a binding energy shift of 0.4 eV. The electronic interactions between Au and Cu_7S_4 may account for this outcome.[39] In Figure 6(b), the Au 4f spectra of Au@CdS and Au colloids displayed doublet features characteristic of metallic Au. The recorded double peaks were located at 88.3 and 84.6 eV for Au@CdS, and 87.9 and 84.3 eV for Au colloids. A noticeable binding energy shift (approximately 0.4 eV) was found for Au@CdS, presumably resulting from the pronounced electronic interactions between Au and CdS.[40] The Cd 3d spectra of Au@CdS and pure CdS showed peak positions (411.7 eV for Cd $3d_{3/2}$ and 405.0 eV for Cd $3d_{7/2}$) corresponding well with the reported values of CdS.[41] For the S 2p spectra, the peak positions of the deconvoluted doublet of pure CdS (162.8 eV for S $2p_{1/2}$ and 161.6 eV for S $2p_{3/2}$) were consistent with the values of CdS.[41] The S 2p peaks of Au@CdS (161.8 eV for S $2p_{1/2}$ and 161.6 eV for S $2p_{3/2}$) also exhibited an obvious binding energy shift (approximately 0.6 eV) compared to those of pure CdS. This outcome, together with the observed perceivable shift of Au 4f binding energy, strongly suggested the prevalence of significant electronic interactions between Au and CdS for Au@CdS.

In Figure 7(a), the analytical results of the Au 4f, Zn 2p and S 2p spectra pointed to the chemical states of metallic Au and ZnS[42] for Au@ZnS. Importantly, Au@ZnS also exhibited a significant binding energy shift in Au 4d (approximately 0.2 eV) and S 2p (approximately 0.2 eV) relative to the Au colloids and pure ZnS. This feature again suggested the pronounced electronic interactions between Au and ZnS for Au@ZnS.[43] For Au@Ni_3S_4, the recorded XPS spectra of Au 4f, Ni 2p and S 2p in Figure 7(b) showed doublet features consistent with the chemical states of metallic Au and Ni_3S_4. Particular attention should be directed to the multiple, overlapping peak features observed in the Ni 2p and S 2p spectra. For the Ni 2p spectra, the peak deconvolution result presented three sets of doublet peaks, which can be attributed to the chemical states of Ni^{2+} (869.7 eV for Ni $2p_{1/2}$ and 852.4 eV for Ni $2p_{3/2}$), Ni^{3+} (873.0 eV for Ni $2p_{1/2}$ and 854.9 eV eV for Ni $2p_{3/2}$) and Ni satellite (878.2 and 859.9 eV).[44] For the S 2p spectra, the deconvoluted peaks contained three components. For pure Ni_3S_4, there was a main doublet (162.7 eV for S $2p_{1/2}$ and 161.6 eV for S $2p_{3/2}$) for S^{2-}, a minor doublet (163.9 eV for S $2p_{1/2}$ and 162.8 eV for S $2p_{3/2}$) for S_2^{2-}, and a broad satellite band (167.7 eV). This multiple, overlapping peak feature of the S 2p spectrum was characteristic of Ni_3S_4, which has also been widely reported in the literature.[44] Compared to pure Ni_3S_4, a noticeable binding energy shift of S 2p components (approximately 0.3 eV) was observed for Au@Ni_3S_4, again suggesting that the electronic interactions between Au and Ni_3S_4 were noticeable.[45] Based on the analytical results of the XPS spectra, we considered that the electronic interactions between the yolk and shell components were significant for the four yolk-shell nanocrystal samples. This feature has important implications for the utilization of the current yolk-shell nanocrystals in energy conversion applications, especially when light irradiation is present.

4.3.3 Light absorption and charge transfer dynamics

To evaluate the potential for photocatalysis applications, we further investigated the light absorption and charge transfer dynamics of the samples. In Figure 8(a), Au@Cu_7S_4 exhibited a prominent absorption edge at approximately 550 nm accompanied by an extended absorption band beyond 700 nm. The prominent absorption edge was attributed to the excitonic band-to-band absorption of Cu_7S_4,[17] while the extended absorption band toward near infrared originated from the plasmonic absorption induced by the nonstoichiometry of Cu_7S_4.[17,46] In Figure 8(b) and 8(c), both Au@CdS and Au@ZnS showed an excitonic absorption edge consistent with the reported bandgap values of CdS[41] and ZnS.[47] Figure 8(d) revealed a wide absorption band spanning the UV, visible and near infrared range for Au@Ni_3S_4. Note that the reported bandgap values of Ni_3S_4 were somewhat divergent, ranging from 1.74 to 2.81 eV;[48–50] moreover, the large refractive index of Ni_3S_4 (n = 2.6)[51] caused serious light scattering. These two features made the identification of the absorption characteristics in Figure 8(d) improbable.

The charge transfer dynamics of the samples were further interrogated with steady-state and time-resolved PL spectroscopy. Figure 9 shows a comparison of steady-state PL spectra between the four yolk-shell nanocrystals and their corresponding pure counterparts. The comparative results collectively revealed a significant decrease in the PL intensity for yolk-shell nanocrystals. Considering the typical band alignment scenario at the metal-semiconductor interface,[22] effective charge carrier separation under light illumination was expected for these yolk-shell nanocrystals. Taking Au@Cu_7S_4 as an example, since the Fermi level of Au (+0.5 V vs. NHE)[52] was less negative than the

conduction band edge of Cu_7S_4 (-1.063 V vs. NHE),[53] the resultant band bending at Au/Cu_7S_4 interface would drive an opposite charge transfer direction of photogenerated electrons to that of photoexcited holes, segregating electrons from holes at the interface. Because electrons were separated from holes, their recombination can be further suppressed to depress the PL intensity. A similar charge transfer scenario was considered for Au@CdS, Au@ZnS and Au@Ni_3S_4 since the conduction band edges of CdS (-1.0 V vs. NHE)[54], ZnS (-1.75 V vs. NHE)[52], and Ni_3S_4 (-1.09 V vs. NHE)[55] were all more negative than the Fermi level of Au. To gain more significant insights into the interfacial charge transfer dynamics, time-resolved PL data were analysed and presented in Figure 10. Relative to their pure counterparts, all four yolk-shell nanocrystals exhibited more rapid PL decay dynamics, confirming that effective charge separation took place at the interface between the yolk and shell. These data were analysed using a biexponential equation to gain more quantitative information. As summarized in Table 1, two lifetime components (τ_1 and τ_2) along with the corresponding amplitude contributions (A_1 and A_2) were computed. The long (τ_1) and short (τ_2) lifetime components can be respectively assigned to the charge carrier relaxation via radiative and non-radiative pathways.[56] Several important points can be noticed here. First, the four yolk-shell samples all exhibited a shortened long lifetime component (τ_1) accompanied by a reduced amplitude contribution (A_1) in comparison with the corresponding pure samples. This outcome manifested that the presence of Au yolk can prohibit the radiative recombination of charge carriers. Second, the amplitude contribution of the short lifetime component (A_2) was found increased for yolk-shell samples. This result signified that additional non-radiative charge transfer emerged within the yolk-shell nanocrystals, presumably associated with the interfacial charge transfer between the semiconductor shell and Au yolk. Third, the

four yolk-shell samples had a shorter average carrier lifetime than their pure counterparts (<τ> = 7.65, 5.48, 6.49 and 4.89 ns for Au@Cu_7S_4, Au@CdS, Au@ZnS, Au@Ni_3S_4 vs. <τ> = 8.82, 6.30, 6.71 and 5.21 ns for pure Cu_7S_4, pure CdS, pure ZnS, pure Ni_3S_4). By assuming that charge transfer between the semiconductor shell and Au yolk accounted for the observed rapid PL decays of yolk-shell nanocrystals, the interfacial charge transfer rate constant (k_{ct}) can be computed by the following equation:

$$k_{ct} = \frac{1}{<\tau>}(yolk - shell\ nanocrystals) - \frac{1}{<\tau>}(pure\ counterparts)$$

For Au@Cu_7S_4, Au@CdS, Au@ZnS, and Au@Ni_3S_4, the calculated k_{ct} values were 1.73 × 10^7, 2.38 × 10^7, 0.51 × 10^7, and 1.25 × 10^7 s^{-1}, respectively. The findings from time-resolved PL spectroscopy, together with the analytical results of XPS spectra, revealed significant electronic interactions and effective charge carrier separation between the yolk and shell components for the four yolk-shell nanocrystals samples. These attributes can be utilized to demonstrate a multitude of photocatalysis applications for the four yolk-shell nanocrystals. As one of the most ancient photocatalysts studied in science, CdS and ZnS can find ubiquitous use in various photocatalytic processes. For the current Au@CdS and Au@ZnS, they are particularly suited to photocatalytic environmental purification, e.g. dye degradation and bacterial disinfection, by virtue of the sufficiently anodic valence band potential of CdS (E_{VB} = +1.5 V vs. NHE)[57] and ZnS component (E_{VB} = +1.85 V vs. NHE).[58] In contrast to the numerous reports on CdS and ZnS, the practical use of Cu_7S_4 and Ni_3S_4 as photocatalysts is still very scarce and is of great interest to fundamental research. With the extended light absorption over the whole visible and even near infrared region, Au@Cu_7S_4 and Au@Ni_3S_4 hold big promise for the development of versatile photocatalytic systems that can harvest photons over the entire solar spectrum and beyond.

As an important note, all of the charge dynamics data were collected with an excitation energy (λ_{ex} = 320 nm) larger than the bandgap of the semiconductor components. The reason of using 320 nm as excitation wavelength was to exclude the possible interference of the plasmonic absorption of the Au yolk at a wavelength beyond 520 nm. Since the current study was aimed to study charge transfer dynamics of the semiconductor shell, a main component producing photoexcited charge carriers for photocatalysis applications, the excitation wavelength was deliberately set at 320 nm to ensure photoexcitation of the four sulfides but avoid plasmonic excitation of Au. Under this experimental condition, the collected charge dynamics data can reflect the veritable fate of photoexcited charge carriers, and most importantly, its influence by the Au yolk as a charge separation enhancer can be revealed. On the other hand, the dependence of charge transfer dynamics of yolk-shell nanocrystals on the excitation wavelength was explored. A qualitative insight into this dependence can be acquired by comparing the steady-state PL spectra of yolk-shell nanocrystals with those of pure counterparts using five different excitation wavelengths (330 nm, 380 nm, 430 nm, 480 nm, 530 nm). Here, Au@CdS and pure CdS were chosen for measurements due to the relatively intense PL emission of CdS component. The extent of PL decay of Au@CdS relative to pure CdS was regarded as a quantitative index to assess the effectiveness of charge carrier separation. In Figure S3 (supporting information), the comparative results showed that the extent of PL decay of Au@CdS for the five different excitation wavelengths was nearly identical, approximately 60 %. This outcome signified that the excitation wavelength did not pose a significant influence on the charge transfer dynamics of yolk-shell nanocrystals.

Because the yolk Au was mobile inside the semiconductor shell, Au was not constantly

in direct contact with semiconductor, especially when these yolk-shell nanocrystals were suspended in solution. This might to some extent affect the effectiveness of interfacial charge transfer between the Au yolk and semiconductor shell. We further collected time-resolved PL data on control samples to address this mystery. Here, the control samples were prepared by keeping the nanocrystal suspension stationary for a long period to fully precipitate the dispersed nanocrystals. For the fully-precipitated yolk-shell nanocrystals, the composed Au yolk would settle to the inner surface of the semiconductor shell and make a direct, constant contact to the shell. This control sample can therefore exhibit enhanced, maximal effectiveness of interfacial charge transfer between the Au yolk and semiconductor shell. By comparing the measured k_{ct} value between the well-suspended and fully-precipitated samples, the extent of the influence of interfacial charge transfer by the mobility of Au yolk can be estimated. Figure S4 (supporting information) and Table S1 (supporting information) displayed the comparative results between the well-suspended and fully-precipitated samples for Au@CdS and pure CdS. As expected, the fully-precipitated Au@CdS exhibited much effective interfacial charge transfer, achieving around 5-fold higher k_{ct} than the well-suspended Au@CdS.

4.4 Chapter Summary

In this work, a sequential ion exchange process on the basis of Kirkendall effect was reported to prepare for metal-semiconductor yolk-shell nanocrystals comprising Au yolks associated with various semiconductor shells. The synthetic procedures involved delicate sulfidation on an Au@Cu_2O core-shell nanocrystal template, followed by a kinetically controlled cation exchange reaction enabling the conversion of shell composition into various metal sulfides. Four representative yolk-shell nanocrystals, Au@Cu_7S_4, Au@CdS,

Au@ZnS and Au@Ni_3S_4, were synthesized for investigation. The analytical results of XPS and PL spectroscopy revealed significant electronic interactions and effective charge carrier separation between the yolk and shell components. This feature has vital implications for utilizing these yolk-shell nanocrystals for photocatalysis applications. In a practical scenario, the separated photoexcited electrons and holes can readily react with the surrounding oxygen and water molecules, producing reactive oxygen species for photocatalytic environmental purification.[58,59] The delocalized, hot electrons at the plasmonic metal yolk may also facilitate specific photoreduction reactions to promote solar fuels generation. Examples have included hydrogen production from water splitting[3,41] and hydrocarbons generation from carbon dioxide reduction.[60,61]

4.5 References

[4-1] Y. Yin, R. M. Rioux, C. K. Erdonmez, S. Hughes, G. A. Somorjai, A. P. Alivisatos, *Science* **2004**, *304*, 711.

[4-2] J. Liu, S. Z. Qiao, J. S. Chen, X. W. (David) Lou, X. Xing, G. Q. (Max) Lu, *Chem. Commun.* **2011**, *47*, 12578.

[4-3] X. Shi, Z. Lou, P. Zhang, M. Fujitsuka, T. Majima, *ACS Appl. Mater. Interfaces* **2016**, *8*, 31738.

[4-4] G. M. Ziarani, P. Mofatehnia, F. Mohajer, A. Badiei, *RSC Adv.* **2020**, *10*, 30094.

[4-5] L. Fan, X. Xu, C. Zhu, J. Han, L. Gao, J. Xi, R. Guo, *ACS Appl. Mater. Interfaces* **2018**, *10*, 4502.

[4-6] C.-H. Kuo, Y. Tang, L.-Y. Chou, B. T. Sneed, C. N. Brodsky, Z. Zhao, C.-K. Tsung, *J. Am. Chem. Soc.* **2012**, *134*, 14345.

[4-7] W. Qi Fang, X. Hua Yang, H. Zhu, Z. Li, H. Zhao, X. Yao, H. Gui Yang, *J. Mater. Chem.* **2012**, *22*, 22082.

[4-8] Z. Jiang, C. Zhu, W. Wan, K. Qian, J. Xie, *J. Mater. Chem. A* **2016**, *4*, 1806.

[4-9] C. M. Cui, X. H. Guo, Y. M. Geng, T. T. Dang, G. Xie, S. P. Chen, F. Q. Zhao, *Chem. Commun.* **2015**, *51*, 9276.

[4-10] J. Liu, L. Yu, C. Wu, Y. Wen, K. Yin, F.-K. Chiang, R. Hu, J. Liu, L. Sun, L. Gu, J. Maier, Y. Yu, M. Zhu, *Nano Lett.* **2017**, *17*, 2034.

[4-11] L. Li, F. Tang, H. Liu, T. Liu, N. Hao, D. Chen, X. Teng, J. He, *ACS Nano* **2011**, *5*, 679.

[4-12] C. C. Yec, H. Chun Zeng, *J. Mater. Chem. A* **2014**, *2*, 4843.

[4-13] H. Zhang, X. Huang, O. Noonan, L. Zhou, C. Yu, *Adv. Funct. Mater.* **2017**, *27*, 1606023.

[4-14] M. Ji, X. Li, H. Wang, L. Huang, M. Xu, J. Liu, J. Liu, J. Wang, J. Zhang, *Nano Res.* **2017**, *10*, 2977.

[4-15] X. Wan, J. Liu, D. Wang, Y. Li, H. Wang, R. Pan, E. Zhang, X. Zhang, X. Li, J. Zhang, *Nano Res.* **2020**, *13*, 1162.

[4-16] A. Li, W. Zhu, C. Li, T. Wang, J. Gong, *Chem. Soc. Rev.* **2019**, *48*, 1874.

[4-17] Y.-H. Chiu, Y.-J. Hsu, *Nano Energy* **2017**, *31*, 286.

[4-18] M. Basu, A. K. Sinha, M. Pradhan, S. Sarkar, Govind, T. Pal, *J. Phys. Chem. C* **2011**, *115*, 12275.

[4-19] B. C. Steimle, J. L. Fenton, R. E. Schaak, *Science* **2020**, *367*, 418.

[4-20] J. L. Fenton, B. C. Steimle, R. E. Schaak, *Science* **2018**, *360*, 513.

[4-21] H.-L. Wu, R. Sato, A. Yamaguchi, M. Kimura, M. Haruta, H. Kurata, T. Teranishi, *Science* **2016**, *351*, 1306.

[4-22] M.-J. Fang, C.-W. Tsao, Y.-J. Hsu, *J. Phys. Appl. Phys.* **2020**, *53*, 143001.

[4-23] M. Murdoch, G. I. N. Waterhouse, M. A. Nadeem, J. B. Metson, M. A. Keane, R. F. Howe, J. Llorca, H. Idriss, *Nat. Chem.* **2011**, *3*, 489.

[4-24] Y.-H. Chiu, K.-D. Chang, Y.-J. Hsu, *J. Mater. Chem. A* **2018**, *6*, 4286.

[4-25] X. Ji, X. Song, J. Li, Y. Bai, W. Yang, X. Peng, *J. Am. Chem. Soc.* **2007**, *129*, 13939.

[4-26] H. Zhang, Z. Zhang, B. Li, Y. Hua, C. Wang, X. Zhao, X. Liu, *CrystEngComm* **2015**, *17*, 3908.

[4-27] S. Jiao, L. Xu, K. Jiang, D. Xu, *Adv. Mater.* **2006**, *18*, 1174.

[4-28] G. Chen, M. Niu, L. Cui, F. Bao, L. Zhou, Y. Wang, *J. Phys. Chem. C* **2009**, *113*, 7522.

[4-29] H. Magnusson, K. Frisk, .

[4-30] W. J. Moore, B. Selikson, *J. Chem. Phys.* **1951**, *19*, 1539.

[4-31] R. D. Shannon, *Acta Crystallogr. A* **1976**, *32*, 751.

[4-32] X. Li, M. Ji, H. Li, H. Wang, M. Xu, H. Rong, J. Wei, J. Liu, J. Liu, W. Chen, C. Zhu, J. Wang, J. Zhang, *Matter* **2020**, *2*, 554.

[4-33] A. T. Nguyen, W.-H. Lin, Y.-H. Lu, Y.-D. Chiou, Y.-J. Hsu, *Appl. Catal. Gen.* **2014**, *476*, 140.

[4-34] S. E. Wark, C.-H. Hsia, D. H. Son, *J. Am. Chem. Soc.* **2008**, *130*, 9550.

[4-35] Y. Li, J. Liu, X. Li, X. Wan, R. Pan, H. Rong, J. Liu, W. Chen, J. Zhang, *ACS Appl. Mater. Interfaces* **2019**, *11*, 27170.

[4-36] H. Zheng, *Nanoscale* **2013**, *5*, 4070.

[4-37] X. Zhang, Y. C. Guo, Z. Cheng Zhang, J. S. Gao, C. M. Xu, *J. Catal.* **2012**, *292*, 213.

[4-38] C. S. Kim, S. H. Choi, J. H. Bang, *ACS Appl. Mater. Interfaces* **2014**, *6*, 22078.

[4-39] J. Zhu, Y. Zhou, W. Wu, Y. Deng, Y. Xiang, Yi. Zhou, *J. Mater. Sci. Mater. Electron.* **2020**, *31*, 3845.

[4-40] H. Wang, D. Peng, X. Hu, X. Ma, W. Ye, W. Zhang, Y. Chang, S. Dong, *Mater. Res. Bull.* **2018**, *108*, 176.

[4-41] Y.-H. Chiu, S. B. Naghadeh, S. A. Lindley, T.-H. Lai, M.-Y. Kuo, K.-D. Chang, J. Z. Zhang, Y.-J. Hsu, *Nano Energy* **2019**, *62*, 289.

[4-42] Y. Kim, K. Giribabu, J. G. Kim, J. B. Lee, W. G. Hong, Y. S. Huh, H. J. Kim, *ACS Sustain. Chem. Eng.* **2019**, *7*, 4094.

[4-43] X. Jin, F. Chen, D. Jia, Y. Cao, H. Duan, M. Long, *RSC Adv.* **2020**, *10*, 4455.

[4-44] D. Jiang, H. Liang, W. Yang, Y. Liu, X. Cao, J. Zhang, C. Li, J. Liu, J. J. Gooding, *Carbon* **2019**, *146*, 557.

[4-45] Y. Lv, S. Duan, Y. Zhu, H. Guo, R. Wang, *Chem. Eng. J.* **2020**, *382*, 122794.

[4-46] I. Kriegel, C. Jiang, J. Rodríguez-Fernández, R. D. Schaller, D. V. Talapin, E. da Como, J. Feldmann, *J. Am. Chem. Soc.* **2012**, *134*, 1583.

[4-47] Y. Feng, N. Feng, G. Zhang, G. Du, *CrystEngComm* **2014**, *16*, 214.

[4-48] O. O. Balayeva, A. A. Azizov, M. B. Muradov, A. M. Maharramov, G. M. Eyvazova, R. M. Alosmanov, Z. Q. Mamiyev, Z. A. Aghamaliyev, *Mater. Res. Bull.* **2016**, *75*, 155.

[4-49] M. Mao, J. Xu, L. Li, S. Zhao, X. Li, *Int. J. Hydrog. Energy* **2021**, *46*, 23190.

[4-50] S. Huang, J. Zai, D. Ma, Z. Hu, Q. He, M. Wu, D. Chen, Z. Chen, X. Qian, *Electrochimica Acta* **2017**, *241*, 89.

[4-51] O. O. Balayeva, A. A. Azizov, M. B. Muradov, G. M. Eyvazova, *Solid-State Electron.* **2017**, *132*, 31.

[4-52] M. Misra, R. K. Gupta, A. K. Paul, M. Singla, *J. Power Sources* **2015**, *294*, 580.

[4-53] P. Bhavani, D. Praveen Kumar, A. Putta Rangappa, Y. Hong, M. Gopannagari, D. Amaranatha Reddy, T. Kyu Kim, *ChemCatChem* **2021**, *13*, 304.

[4-54] G. Song, F. Xin, J. Chen, X. Yin, *Appl. Catal. Gen.* **2014**, *473*, 90.

[4-55] Y. Qi, J. Xu, M. Zhang, H. Lin, L. Wang, *Int. J. Hydrog. Energy* **2019**, *44*, 16336.

[4-56] T.-T. Yang, W.-T. Chen, Y.-J. Hsu, K.-H. Wei, T.-Y. Lin, T.-W. Lin, *J. Phys. Chem. C* **2010**, *114*, 11414.

[4-57] W.-T. Chen, Y.-J. Hsu, *Langmuir* **2010**, *26*, 5918.

[4-58] J. Zhao, W. Li, L. Fan, Q. Quan, J. Wang, C. Xiao, *J. Colloid Interface Sci.* **2019**, *534*, 480.

[4-59] J. Zhou, L. Xu, J. Sun, D. He, H. Jiao, *Surf. Coat. Technol.* **2015**, *271*, 119.

[4-60] W. Tu, Y. Zhou, H. Li, P. Li, Z. Zou, *Nanoscale* **2015**, *7*, 14232.

[4-61] H. Liu, X. Meng, T. Duy Dao, L. Liu, P. Li, G. Zhao, T. Nagao, L. Yang, J. Ye, *J. Mater. Chem. A* **2017**, *5*, 10567.

4.6 Figures

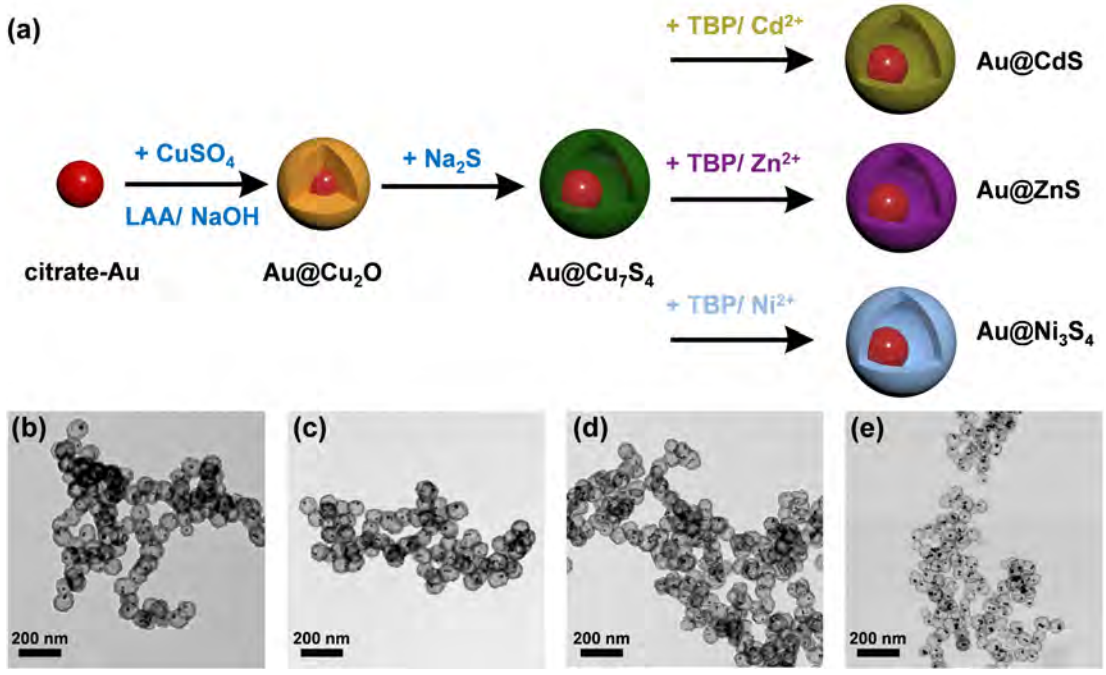

Figure 4-1. (a) Schematic depiction of the synthetic procedure for Au@Cu_7S_4, Au@CdS, Au@ZnS, and Au@Ni_3S_4. (b-e) shows the corresponding TEM images.

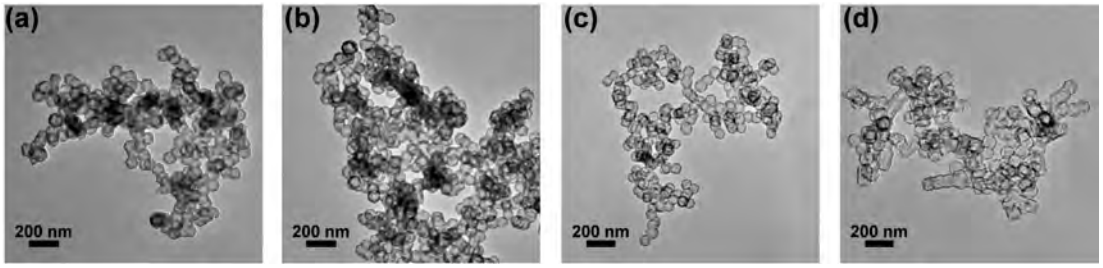

Figure 4-2. TEM images for (a) pure Cu_7S_4, (b) pure CdS, (c) pure ZnS, and (d) pure Ni_3S_4.

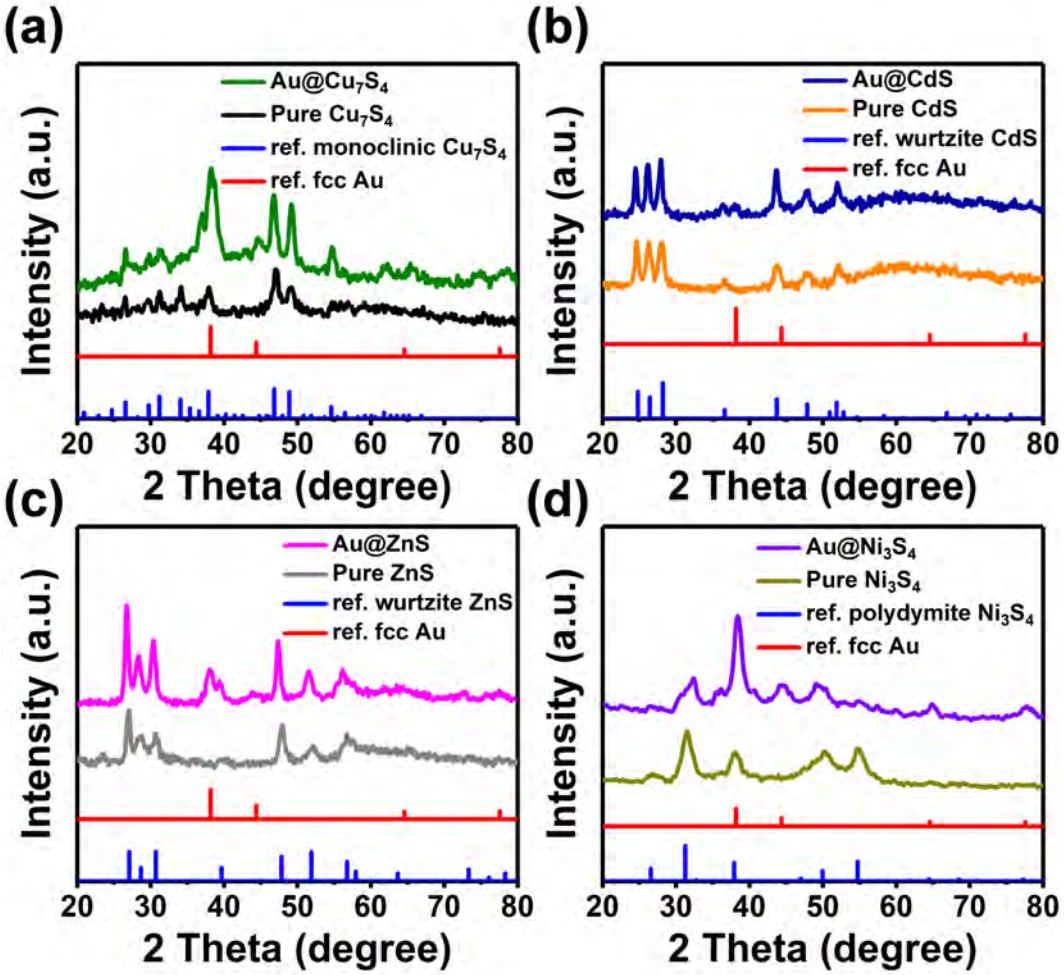

Figure 4-3. XRD patterns for (a) Au@Cu_7S_4, (b) Au@CdS, (c) Au@ZnS, and (d) Au@Ni_3S_4. The patterns of pure counterpart samples and the reference fcc Au, monoclinic Cu_7S_4, wurtzite CdS, wurtzite ZnS, and polydymite Ni_3S_4 were also included.

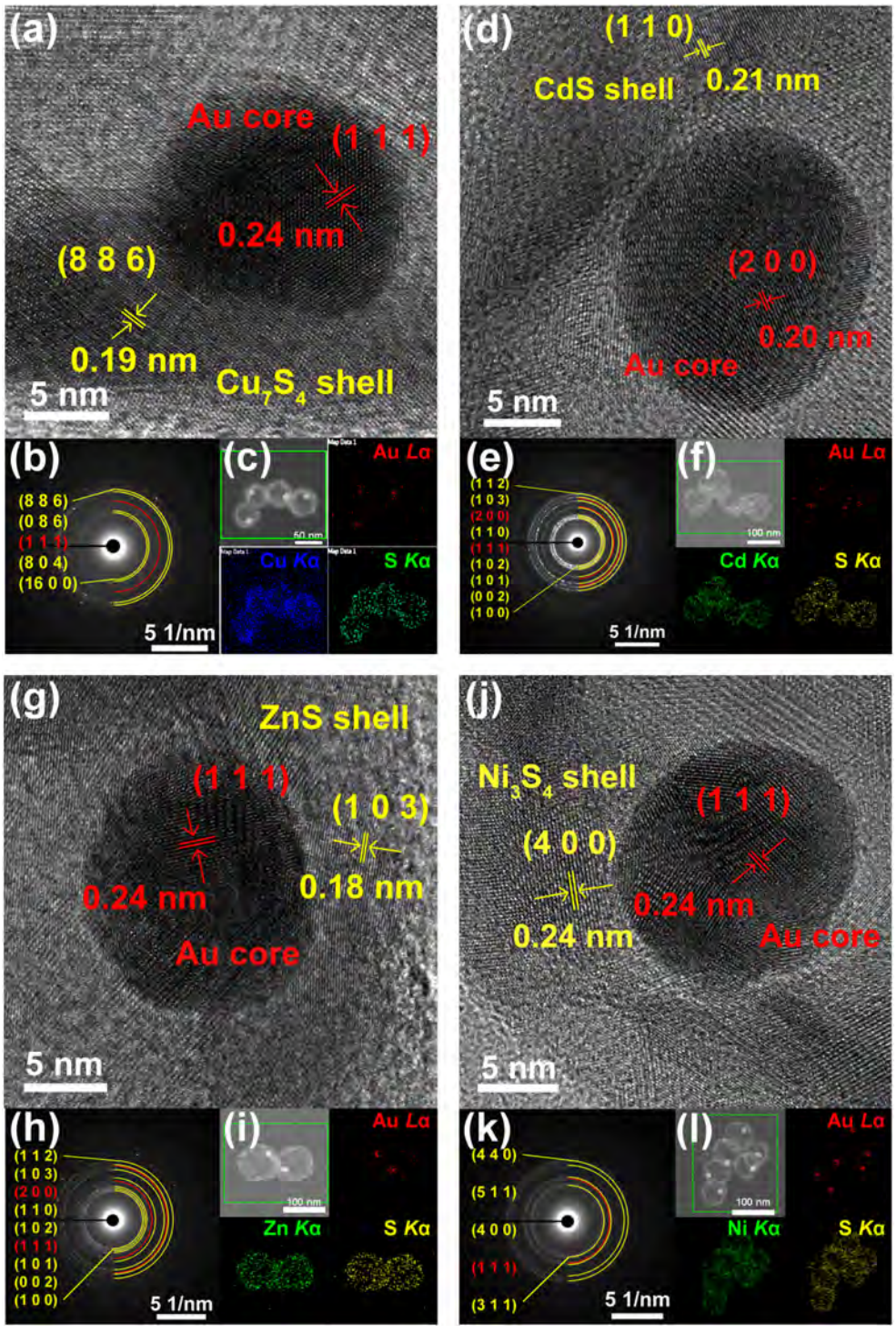

Figure 4-4. HRTEM image, SAED pattern and EDS mapping analysis for (a-c) Au@Cu_7S_4, (d-f) Au@CdS, (g-i) Au@ZnS, and (j-l) Au@Ni_3S_4.

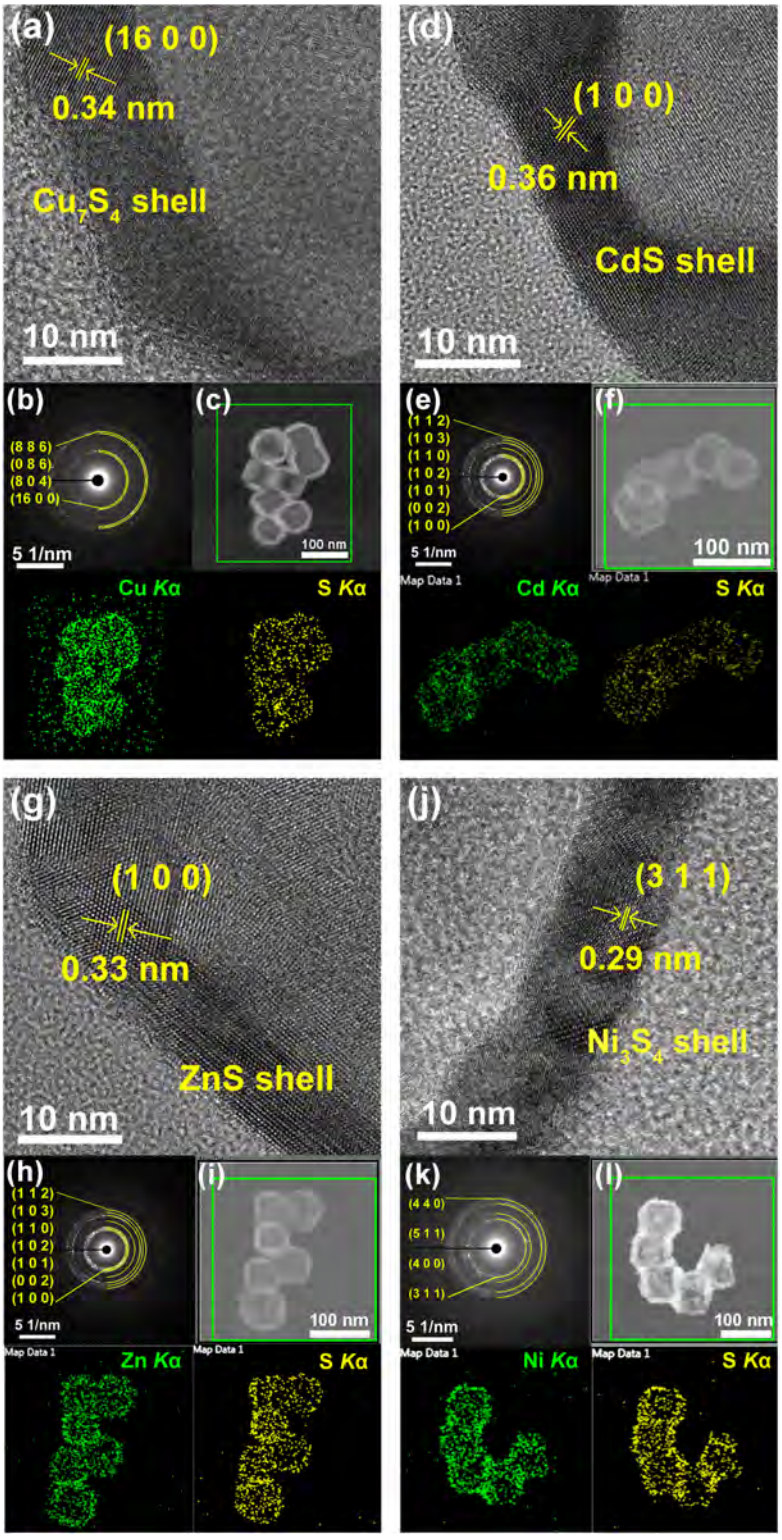

Figure 4-5. HRTEM image, SAED pattern and EDS mapping analysis for (a-c) pure Cu_7S_4, (d-f) pure CdS, (g-i) pure ZnS, and (j-l) pure Ni_3S_4.

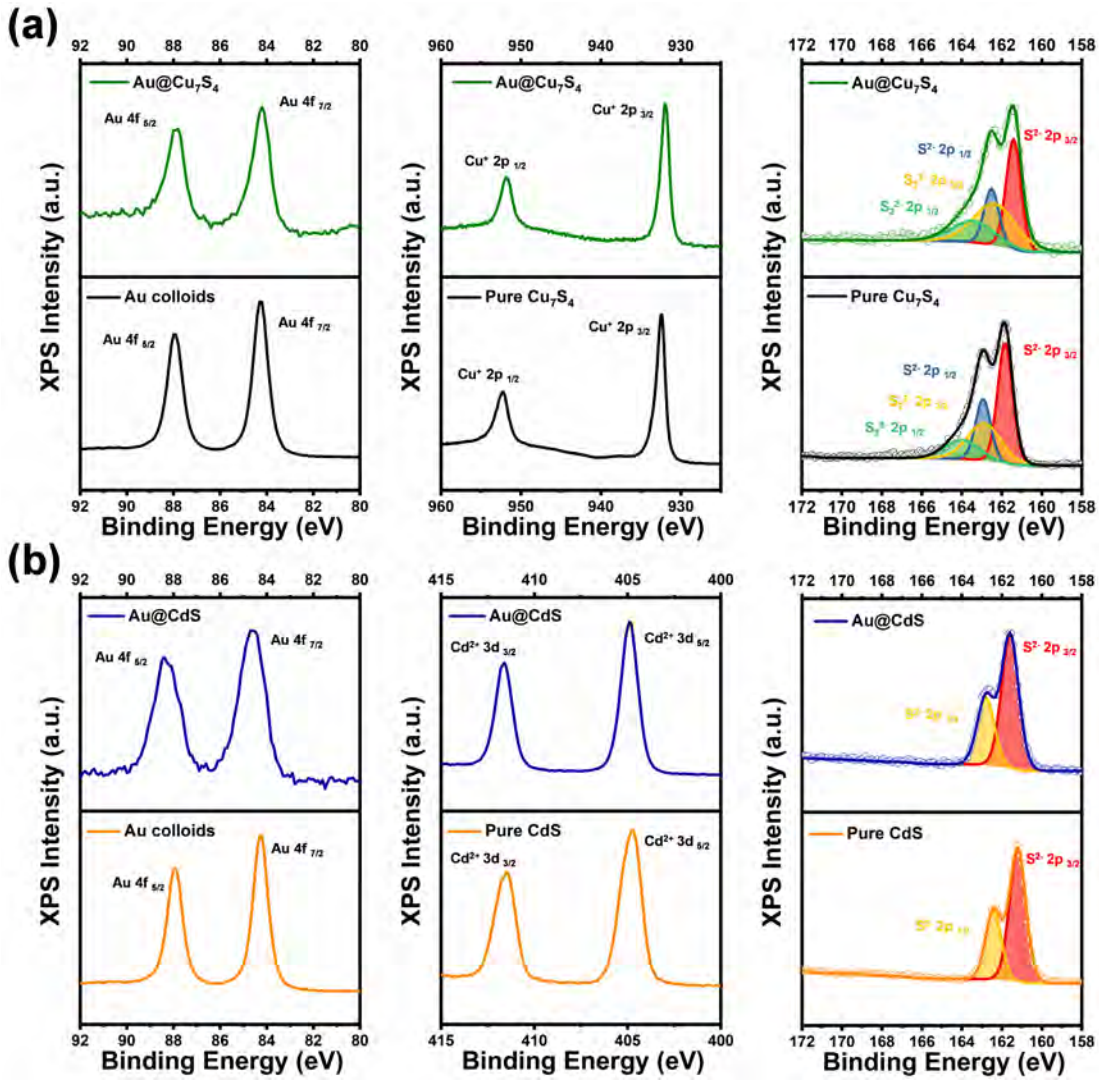

Figure 4-6. HRTEM image, SAED pattern and EDS mapping analysis for (a-c) pure Cu_7S_4, (d-f) pure CdS, (g-i) pure ZnS, and (j-l) pure Ni_3S_4.

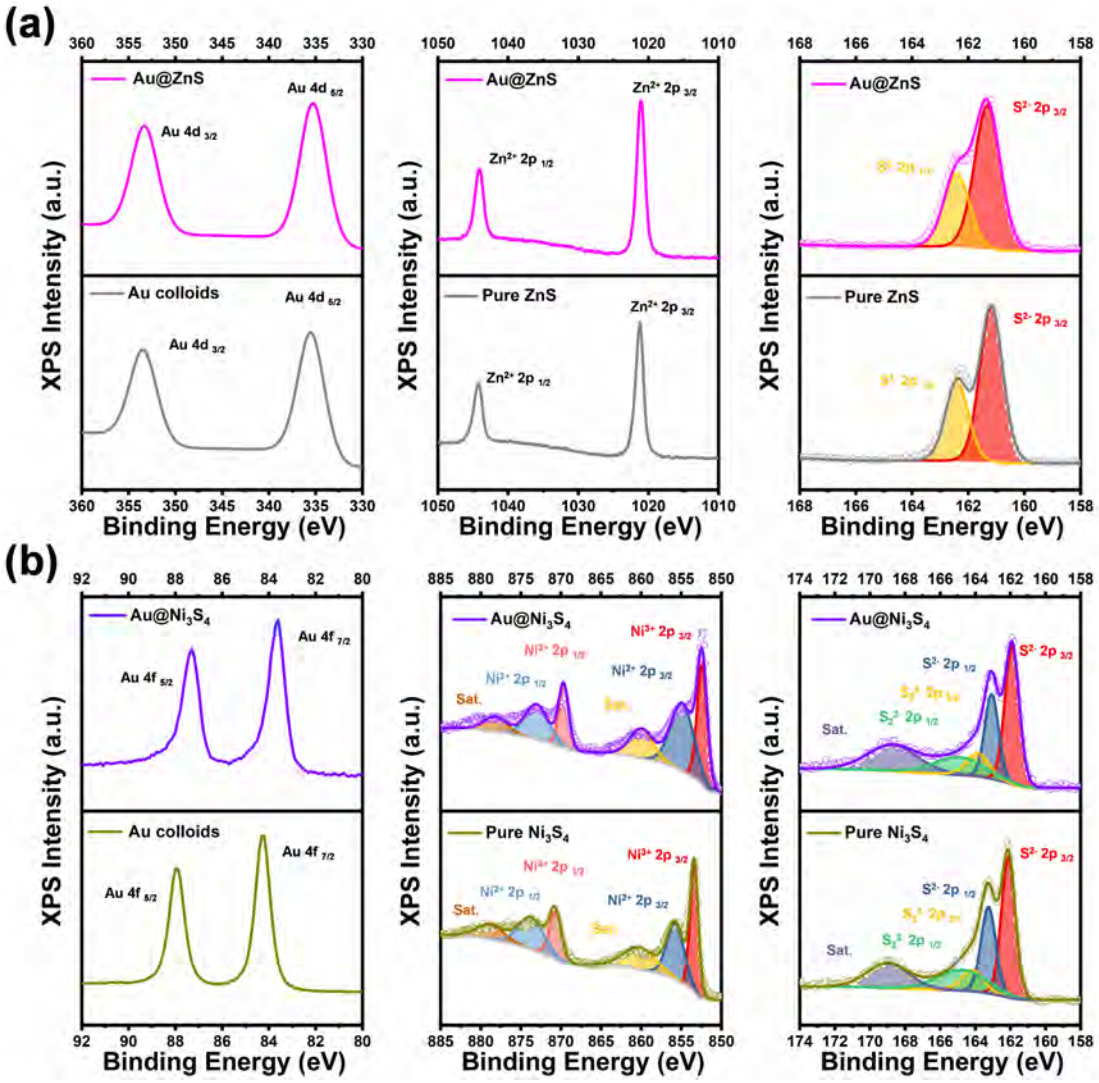

Figure 4-7. HRTEM image, SAED pattern and EDS mapping analysis for (a-c) pure Cu_7S_4, (d-f) pure CdS, (g-i) pure ZnS, and (j-l) pure Ni_3S_4.

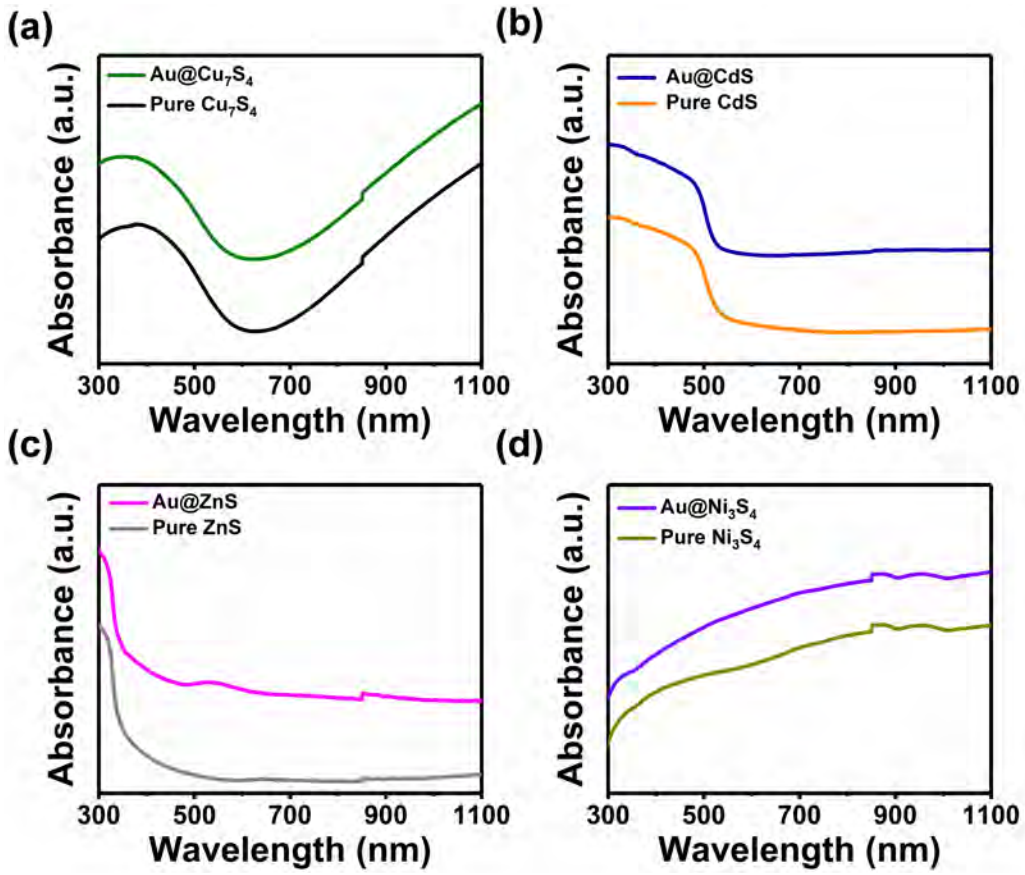

Figure 4-8. HRTEM image, SAED pattern and EDS mapping analysis for (a-c) pure Cu_7S_4, (d-f) pure CdS, (g-i) pure ZnS, and (j-l) pure Ni_3S_4.

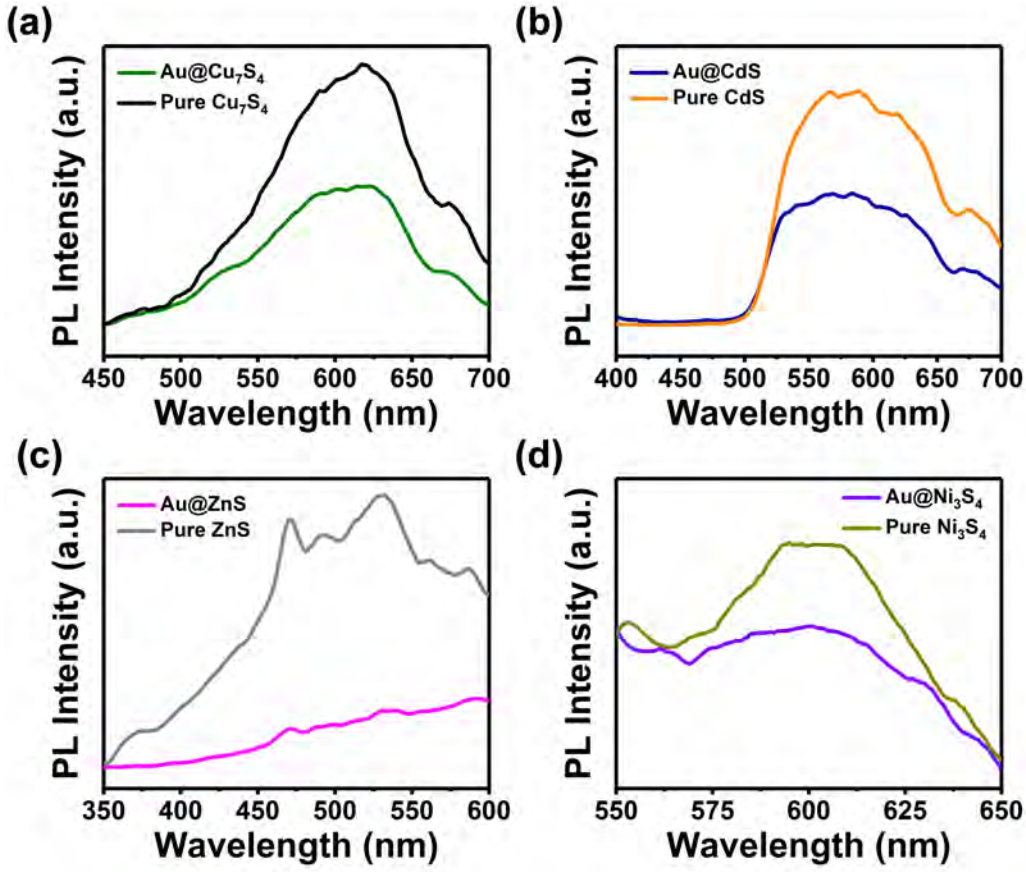

Figure 4-9. HRTEM image, SAED pattern and EDS mapping analysis for (a-c) pure Cu_7S_4, (d-f) pure CdS, (g-i) pure ZnS, and (j-l) pure Ni_3S_4.

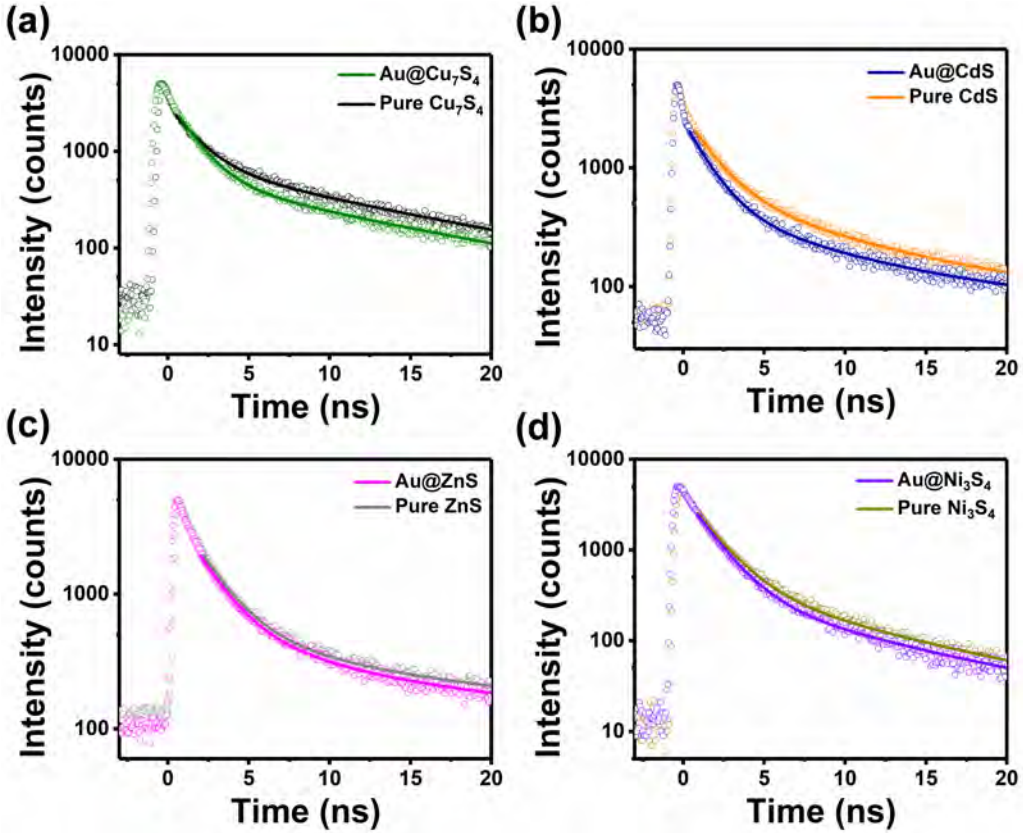

Figure 4-10. HRTEM image, SAED pattern and EDS mapping analysis for (a-c) pure Cu_7S_4, (d-f) pure CdS, (g-i) pure ZnS, and (j-l) pure Ni_3S_4.

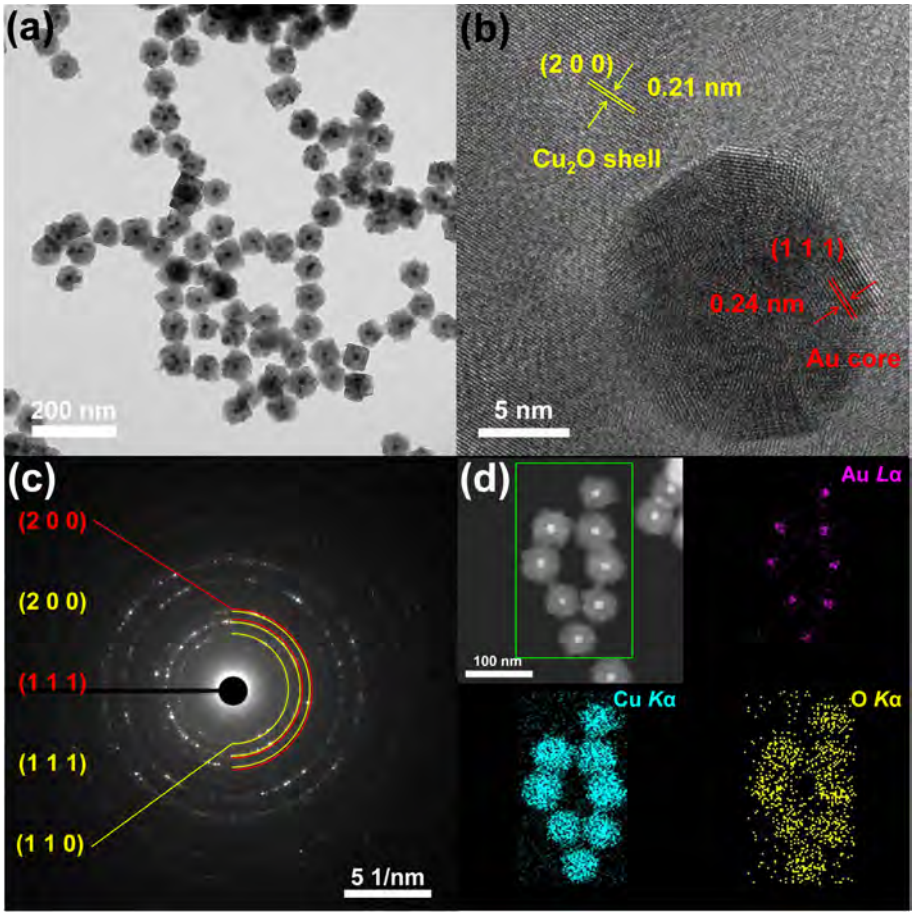

Figure 4-S1. (a) Typical TEM image, (b) HRTEM image, (c) SAED pattern and (d) EDS mapping analysis for Au@Cu_2O

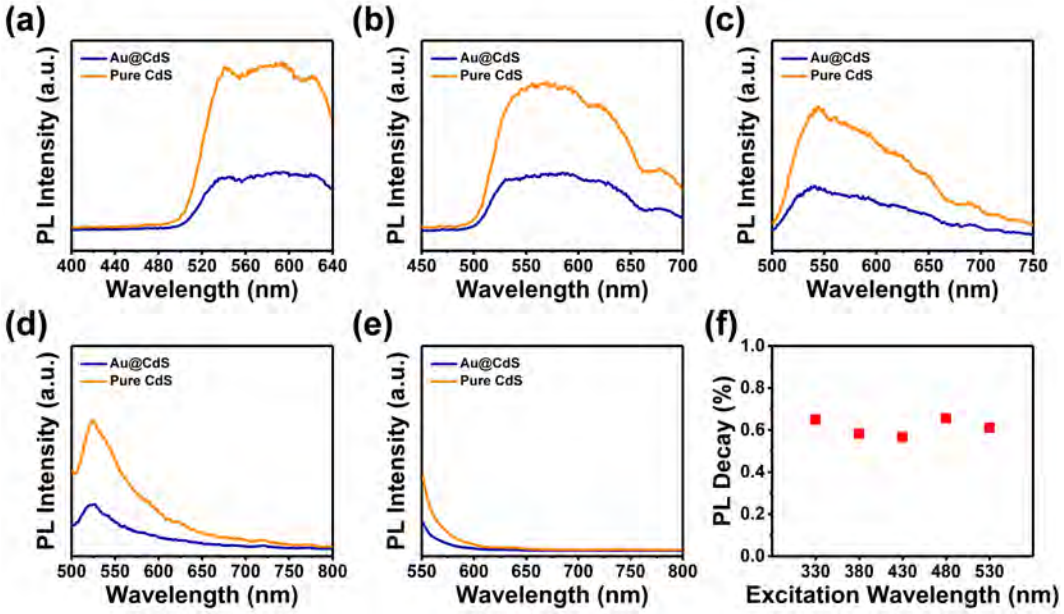

Figure 4-S2. (a) Typical TEM image, (b) HRTEM image, (c) SAED pattern and (d) EDS mapping analysis for Au@Cu_2O

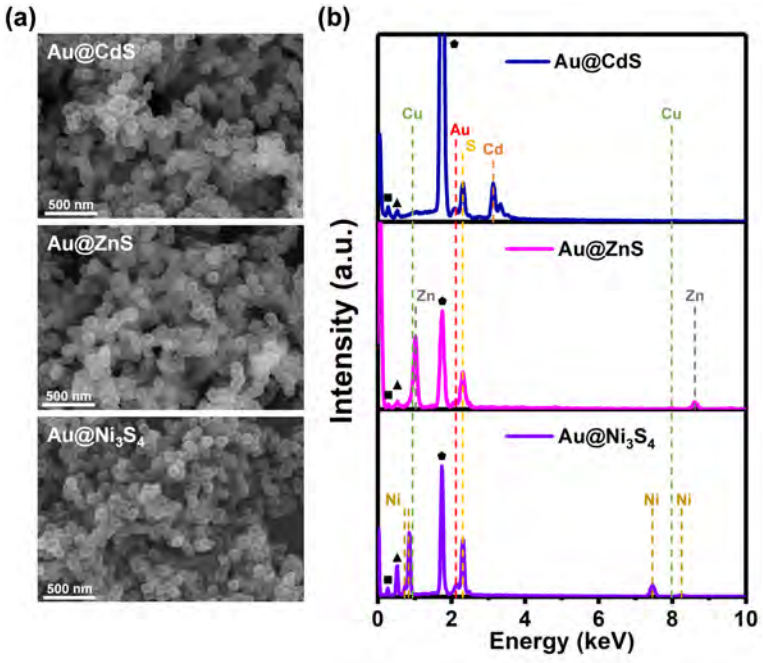

Figure 4-S2. (a) SEM images and (b) the corresponding EDS spectra of Au@CdS, Au@ZnS and Au@Ni_3S_4 (■: C, ▲: O, ⬟: Si).

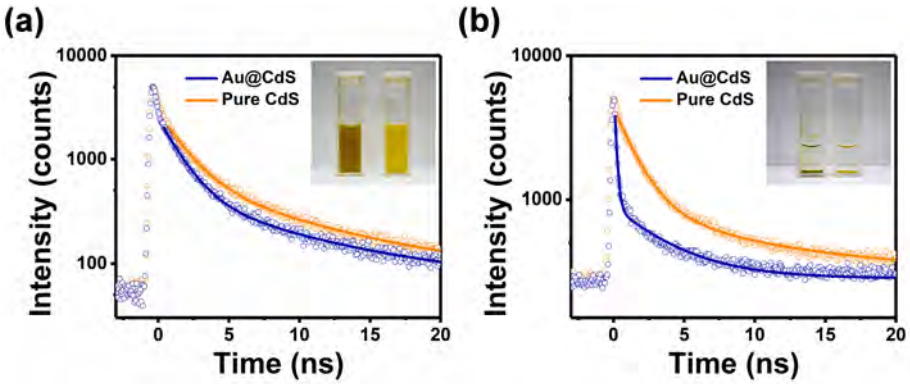

Figure 4-S3. Time-resolved PL spectra for (a) well-suspended and (b) fully-precipitated samples. Insets show the photos of the appearance of the sample solutions (left side: Au@CdS, right side: pure CdS).

4.7 Tables

Table 4-1. Fitted parameters of time-resolved PL data for all the samples.

Entry	A_1(%)	τ_1(ns)	A_2(%)	τ_2(ns)	χ^2	$<\tau>$(ns)	k_{ct}(s^{-1})
Pure Cu_7S_4	29.48	11.24	70.52	1.57	1.07	8.82	-
Au@Cu_7S_4	19.80	10.91	80.20	1.41	1.00	7.65	1.73×10^7
Pure CdS	26.74	8.76	73.26	1.73	1.05	6.30	-
Au@CdS	19.77	8.35	80.23	1.48	1.03	5.48	2.38×10^7
Pure ZnS	22.33	9.86	77.67	1.83	1.08	6.71	-
Au@ZnS	22.13	9.61	77.87	1.82	1.09	6.49	0.51×10^7
Pure Ni_3S_4	14.12	9.18	85.88	1.73	1.06	5.21	-
Au@Ni_3S_4	12.41	9.04	87.59	1.64	1.06	4.89	1.25×10^7

Table 4-S1. Fitted parameters of time-resolved PL data for well-suspended (s) and fully precipitated (p) samples.

Entry	A_1(%)	τ_1(ns)	A_2(%)	τ_2(ns)	χ^2	$<\tau>$(ns)	k_{ct}(s^{-1})
Pure CdS (s)	26.74	8.76	73.26	1.73	1.05	6.30	-
Au@CdS (s)	19.77	8.35	80.23	1.48	1.03	5.48	2.38×10^7
Pure CdS (p)	17.30	8.50	82.70	1.50	1.19	5.29	-
Au@CdS (p)	17.04	3.77	82.96	0.16	1.18	5.48	1.39×10^8

CHAPTER 5

General conclusions

5.1 Conclusions

In the foregoing analyses, a profound exploration of metal@Cu_2O core-shell nanocrystals and metal-semiconductor yolk-shell nanocrystals has been executed to address the exigent environmental quandary posed by synthetic dye wastewater. The investigative journey commenced with the synthesis and assiduous characterization of metal@Cu_2O core-shell nanocrystals, where a trio of distinct metal cores (Ag, Pd, and Au) were integrated to scrutinize the core-dependent variations in photocatalytic aptitude. Among the scrutinized structures, the Au@Cu_2O nanocrystal exhibited unparalleled prowess in the photocatalytic degradation of MO, a merit attributed to the enhanced charge segregation at the core-shell interface and its electron trapping ability. The narrative further unfolded with an in-depth examination of charge-transfer dynamics through both steady-state and time-resolved PL spectroscopy, elucidating the mechanisms propelling the observed performance metrics. Transitioning to a more pragmatic realm, Au@Cu_2O-functionalized PET fabrics were prepared and evaluated for photocatalytic degradation of MO, showcasing a tangible application of these nanocrystals in environmental decontamination endeavors. The influence of shell thickness on

photocatalytic performance was meticulously examined, rendering a comprehensive understanding of the interplay between structural attributes and photocatalytic efficacy. Subsequently, the foray into metal-semiconductor yolk-shell nanocrystals unveiled a novel sequential ion-exchange process, furnishing a collection of yolk-shell nanocrystals with diversified semiconductor shells. The electronic interactions and charge-transfer dynamics between the yolk and shell components were thoroughly examined, revealing a significant enhancement in charge-carrier separation, which holds paramount implications for a multitude of photocatalysis applications. The manifested charge separation exhibits potential in promoting solar fuels generation, including hydrogen production from water splitting and hydrocarbons generation from carbon dioxide reduction. Collectively, these investigations not only offer a substantive solution to a pressing environmental issue but also scaffold an edifice for future endeavors aimed at optimizing and broadening the applications of hybrid nanocrystal-based photocatalysts, thereby bridging the chasm between theoretical investigation and practical environmental purification and energy conversion applications.

Acknowledgements

Firstly, I owe a deep sense of gratitude to my advisor, Prof. Sone. Your unwavering support, insightful feedback, and warm guidance have been the backbone of my doctoral journey. Your commitment to academic excellence and your care for my well-being have not only shaped this dissertation but also greatly influenced my personal and academic growth.

I am sincerely thankful to Prof. Mark Chang, whose invaluable suggestions and attentive guidance have significantly accelerated my academic development. Your creative thinking and dedication have continuously inspired me and broadened my horizons.

A heartfelt thank you goes to Prof. Hsu, whose expertise and passion have laid a solid foundation for my work. Your engaging discussions and positive feedback have been essential in refining my research methods and theories.

I extend my sincere appreciation to Prof. Kurioka, whose deep knowledge and encouragement have been a source of inspiration. Your thoughtful suggestions and steadfast support have greatly contributed to the betterment of this dissertation.

I also want to thank Prof. Chen for her invaluable guidance and support throughout

this journey. Your insightful feedback and extensive expertise have been crucial in advancing my research to a higher level.

Special recognition goes to Prof. Okamoto from Sumitomo Chemical, whose extensive knowledge and collaborative spirit have significantly enriched my research. The discussions, critiques, and collaboration with Sumitomo Chemical, guided by Prof. Okamoto, have been a remarkable part of my doctoral experience, greatly enhancing the quality and scope of my work.

The administrative support from Toda san has been indispensable. Your consistent support, patience, and diligence have eased the daily challenges and significantly contributed to my academic endeavors.

I extend my warm appreciation to my classmates Mei-Jing Fang, Ting-Hsuan Lai, Ming-Yu Kuo, Chun-Wen Tsao, Ping-Yen Hsieh, Yi-Hsuan Chiu, Yi-An Chen, Hsuan-Hung Kuo, Yu-An Chien, Po-Wei Cheng, Yiming Jiang, Huai-En Chang, Yu-Peng Chang, Chien-Yi Wang, Yu-Ting Wang, Jen-An Shih, Jyoti Rohilla, Zeyu Gu, Ryohei Hori, Ami Iwasaki, Hikaru Kondou, Shohei Yoshida, Vinaisuratern Punvinai, Takumi Akiyama, Keisuke Okamoto, and Taro Omura. Your friendship, feedback, and enduring support have made this academic journey both rewarding and enjoyable. The collaborative spirit and constructive discussions have enriched my understanding and significantly

contributed to my research experience.

My deepest thanks go to my family for their unconditional love and support throughout my educational journey. Their sacrifices and belief in me have been the driving force behind my perseverance.

A special note of thanks goes to my love, Zhaoma Shu, whose love, understanding, and encouragement have been my constant source of strength. Your unwavering faith in my abilities and endless support have been nothing short of a blessing during this journey.

Thank you to all who have supported and assisted me in this endeavor, making the completion of this dissertation a reality.

JHEN-YANG WU

Appendix A List of achievements and others

A.1 Awards

- Interchange Association international student scholarship, Japan–Taiwan Interchange Association

  Apr. 2022-Apr. 2024

- Research Fellow, Institute of Innovative Research, Tokyo Tech

  Apr. 2022-Apr. 2024

A.2 Publications

A.2.1 International journal papers

1. **J.-Y. Wu,** T.-H. Lai, M.-J. Fang, J.-Y. Chen, M.-Y. Kuo, Y.-H. Chiu, P.-Y. Hsieh, C.-W. Tsao, H.-E. Chang, Y.-P. Chang, C.-Y. Wang, C.-Y. Chen, M. Sone, W.-W. Wu, T.-F.M. Chang, Y.-J. Hsu, "Functionalization of polyethylene terephthalate fabrics with au@Cu_2O core@shell nanocrystals for environmental purifications." Micro and Nano Engineering (2023)
2. **J.-Y. Wu**, Y.-A. Chen, Y.-A. Chien, T. Kurioka, M. Sone, C.-Y. Chen, T.-F. M. Chang, Y.-J. Hsu, "Photocatalytic Fibers for Environmental Purification: Challenges and Opportunities in the Post-Pandemic Era." Advanced Energy and Sustainability Research, in press.
3. **J.-Y. Wu,** T.-H. Lai, M.-J. Fang, J.-Y. Chen, M.-Y. Kuo, Y.-H. Chiu, P.-Y. Hsieh, C.-W. Tsao, H.-E. Chang, Y.-P. Chang, C.-Y. Wang, C.-Y. Chen, M. Sone, W.-W. Wu, T.-F.M. Chang, Y.-J. Hsu, "Electronic Interactions and Charge-Transfer Dynamics for a Series of Yolk–Shell Nanocrystals: Implications for Photocatalysis." ACS Applied Nano Materials (2022)
4. **J.-Y. Wu,** H.-E. Chang, Y.-A. Chen, M.-J. Fang, T.-H. Lai, M.-Y. Kuo, C.-W. Tsao, T. Kurioka, M. Sone, C.-Y. Chen, T.-F.M. Chang, Y.-J. Hsu. Tunable Photocatalytic Properties of Metal@Cu_2O Core–Shell Nanostructures for Methyl Orange Degradation. (Under review)
5. P.-Y. Hsieh, **J.-Y. Wu,** T.-F.M. Chang, C.-Y. Chen, M. Sone, Y.-J. Hsu, "Near infrared-driven photoelectrochemical water splitting: Review and future prospects." Arabian Journal of Chemistry (2020)
6. M.-J. Fang, Y.-C. Lin, J.-Y. Jan, T.-H. Lai, P.-Y. Hsieh, M.-Y. Kuo, Y.-H. Chiu, C.-W.

Tsao, Y.-A. Chen, Y.-T. Wang, Y.-J. Hong, **J.-Y. Wu,** Y.C.S. Wu, Y.-G. Lin, T.-F.M. Chang, C.-Y. Chen, M. Sone, S.-M. Chang, C.-L. Chang, Y.-J. Hsu, "Au@Cu_2O core@shell nanocrystals as sustainable catalysts for efficient hydrogen production from ammonia borane." Applied Catalysis B: Environmental (2023)

7. T.-H. Lai, C.-W. Tsao, M.-J. Fang, **J.-Y. Wu,** Y.-P. Chang, Y.-H. Chiu, P.-Y. Hsieh, M.-Y. Kuo, K.-D. Chang, Y.-J. Hsu, "Au@Cu2O Core–Shell and Au@Cu2Se Yolk–Shell Nanocrystals as Promising Photocatalysts in Photoelectrochemical Water Splitting and Photocatalytic Hydrogen Production." ACS Applied Materials & Interfaces (2022)
8. M.-Y. Kuo, C.-F. Hsiao, Y.-H. Chiu, T.-H. Lai, M.-J. Fang, **J.-Y. Wu,** J.-W. Chen, C.-L. Wu, K.-H. Wei, H.-C. Lin, Y.-J. Hsu, "Au@Cu_2O core@shell nanocrystals as dual-functional catalysts for sustainable environmental applications." Applied Catalysis B: Environmental (2019)
9. S.B. Naghadeh, S. Sarang, A. Brewer, A. Allen, Y.-H. Chiu, Y.-J. Hsu, **J.-Y. Wu,** S. Ghosh, J.Z. Zhang, "Size and temperature dependence of photoluminescence of hybrid perovskite nanocrystals." Journal of Chemical Physics (2019)
10. **J.-Y. Wu**, Y.-A. Chen, Y.-A. Chien, T. Kurioka, M. Sone, C.-Y. Chen, T.-F. M. Chang, Y.-J. Hsu, "Photocatalytic Fibers for Environmental Purification: Challenges and Opportunities in the Post-Pandemic Era." Advanced Energy and Sustainability Research (2023)
11. (Under review) **J.-Y. Wu**, H.-E. Chang, Y.-A. Chen, M.-J. Fang, T.-H. Lai, M.-Y. Kuo, C.-W. Tsao, T. Kurioka, M. Sone, C.-Y. Chen, T.-F. M. Chang, Y.-J. Hsu, "Tunable Photocatalytic Properties of Metal@Cu_2O Core–Shell Nanostructures for Methyl Orange Degradation"

A.2.2 International conferences

1. **Jhen-Yang Wu**, Tomoyuki Kurioka, Chun-Yi Chen, Masato Sone, Satoshi Okamoto, Tso-Fu Mark Chang, Yung-Jung Hsu: Hydrothermal fabrication of Au-$BiFeO_3$ for superior photocatalytic degradation efficiency, The 2023 International Thin Film Conference (TACT 2023), November 13, 2023 [Oral].
2. **Jhen-Yang Wu**, Tomoyuki Kurioka, Chun-Yi Chen, Masato Sone, Tso-Fu Mark Chang, Yung-Jung Hsu, Functionalization of Polyethylene Terephthalate Fabrics with Au@Cu2O Core@Shell Nanocrystals for Environmental Purifications, 35th Topical Meeting of the International Society of Electrochemistry, May 23, 2023 [Poster].
3. **Jhen-Yang Wu**, Tomoyuki Kurioka, Chun-Yi Chen, Masato Sone, Tso-Fu Mark Chang, Yung-Jung Hsu, Functionalization of Polyethylene Terephthalate Fabrics with Au@Cu2O Core@Shell Nanocrystals for Environmental Purifications, 第 70 回応用物理学会春季学術講演会, Mar 23, 2023 [Oral].
4. **Jhen-Yang Wu**, Tomoyuki Kurioka, Chun-Yi Chen, Masato Sone, Tso-Fu Mark Chang, Yung-Jung Hsu: Functionalization of polyethylene terephthalate fabrics with Au@Cu_2O core@shell nanocrystals for environmental purifications, 48th International Conference on Micro and Nano Engineering, September 19-23, 2022 [Poster].